AN INTRODUCTION TO MULTIFRACTAL GEOMETRY OF WAVE SEA STATES ON THE WEST AND SOUTH-EAST COASTS OF SOUTH AFRICA

by

Keith Robert MacHutchon

Thesis presented for Doctor of Philosophy in Engineering at the Faculty of Engineering at the University of Stellenbosch

Promotor: Prof. G.R. Basson

Co-Promotor: Mr. G Toms

Faculty of Engineering Department of Civil Engineering

March 2015

DECLARATION

By submitting this dissertation electronically, I declare that the entirety of the work contained therein is my own, original work, that I am the sole author thereof (save to the extent explicitly otherwise stated), that reproduction and publication thereof by Stellenbosch University will not infringe any third party rights and that I have not previously in its entirety or in part submitted it for obtaining any qualification.

Signature: …… Date: …….

Abstract

All of the Ports along the South African coastline are subject to bound infragravity wave action to a greater or lesser degree, for example, at the Ports of Saldanha Bay on the west coast and Ngqura on the south-east coast. Saldanha Bay harbour principally services loose- and liquid-bulk carriers and the Ngqura harbour mainly services container ships. The long wave actions when severe cause moorings to be broken, ships to leave the quay and loading to stop.

This research has confirmed that the sea surface is a multifractal structure characterised by many singularities ranging from highly irregular or rough features to smooth or calm features. Any wave train is comprised of the full range of these features to various degrees and in varying percentages of occupancy.

Notwithstanding this problem, relatively little is known about them in the South African context due to the fact that they cannot be visually detected and specialised, sophisticated equipment is required to physically measure them. The country is currently planning the development of a new port and the expansion of others for larger ships. Under these circumstances this research is seen to be appropriate from the point of view of obtaining a new method for the characterisation of these hazardous wave conditions.

The objective of the research was achieved. This was to identify a set of fractal dimensions that describe the surface geometry of a hazardous bound infragravity wave sea state.

In order to achieve the objective, a set of fractal dimensions was firstly determined from video imagery of an open water wave field, by analysing a set of single point time series data derived from the imagery. This has been done in order to be able to visually compare the derived set of fractal dimensions with video imagery of the sea surface that they represent. It also has the advantage of proving that fractal methods of analysis are applicable for the study of sea surface single point time series data.

Secondly, periods when long wave action occurs at both Saldanha Bay and Ngqura harbours were identified by the presence of their actions in the harbours.

Thirdly, single point time series data recorded by the Council for Scientific and Industrial Research (CSIR) were obtained during the identified periods as well as two days before these times and fractal sets of dimensions for the periods were determined. This was achieved by means of the following methods of analysis:

- The rescaled range (R/S) method,
- The Multifractal Detrended Fluctuation Analysis (MDFA) method,
- The Power Spectral Density (PSD) method in both the Fourier and the wavelet domains, and
- The Wavelet Transform method.

Fourthly, the fractal data sets from each harbour were compared to confirm that the sets of dimensions for the hazardous sea state are clearly different from those of the non-hazardous sea state and can be used to describe the condition.

Finally, the fractal sets of dimensions for hazardous sea states at both harbours were compared to identify any variances between them.

During the research it was found that a hazardous sea state could be profiled for identification purposes and for complementing the currently determined significant wave height and peak period details by means of fractal indices.

These indices were identified by comparison with a similar set of indices for non-hazardous sea states at the same location, as part of a ‘calibration’ process and clearly identified shifts in the Holder exponents of the sea states enabled the unambiguous identification of the hazardous condition.

Having completed the research and analysis work, the author has identified other areas of coastal engineering, besides the identification of hazardous bound

infragravity wave sea states, where a study of multifractal geometry could be applied advantageously.

Opsomming

Alle hawens langs Suid Afrika se kuslyn is tot ‘n meerdere of mindere mate onderworpe aan gebonde infragravitasie golf aksie. Hierdie probleem is egter veral straf by die hawens van Saldanhabaai aan die weskus en Ngqura, aan die suidooskus. Saldanhabaai voorsien dienste hoofsaaklik aan massa draers van los stowwe en vloeistof, terwyl Ngqura hoofsaaklik houerskepe bedien. Die lang golf aksies veroorsaak dat ankertoue breek en die skepe die kaai verlaat, sodat laai van die skepe tot stilstand kom.

In die loop van hierdie navorsing is gevind dat die seevlak ‘n multifraktale struktuur is, met singulariteitseienskappe wat wissel van hoogs onreëlmatig of rowwe eienskappe tot gladde, reëlmatige eienskappe. Enige golfreeks behels die volle omvang van hierdie eienskappe in verskillende grade en wisselende teenwoordigheids persentasies.

Die navorsing is gefokus op die geometrie van gebonde infragravitasie golfaksie seetoestande, wat oral langs die Suid Afrikaanse kuslyn voorkom, en in twee hawens ‘n beduidende bedreiging vir vasgemaakte skepe is. Ondanks die probleem, is min bekend oor hierdie toestande in Suid Afrikaanse konteks, omdat hulle nie visueel bespeur kan word nie en spesiale gesofistikeerde gereedskap nodig is om hulle fisies te kan meet. Daar word tans beplan om ‘n nuwe hawe te ontwikkel, wat hierdie navorsing veral gepas maak, met die doel om ‘n meer volledige beskrywing van hierdie bedreigende golftoestande te weeg te bring.

Die doel van die navorsing is om ‘n stel fraktale dimensies te identifiseer wat die oppervlakgeometrie van ‘n bedreigende gebonde infragravitasie golf-seetoestand omskryf. Hierdie dimensies kan dan gebruik word om ‘n indentifiserende profiel van die seetoestand te teken om die inligting tans beskikbaar oor beduidende golfhoogte en piektye, aan te vul.

Om hierdie doel te bereik is ‘n stel fraktale dimensies eerstens bepaal deur middel van videobeelding van ‘n oopwater golfveld. ‘n Stel enkelpunt tydserie data, afgelei van die beelding, word dan ge-analiseer. Dit het visuele vergelyking tussen die afgeleide stel fraktale dimensies en die videobeelding van die seevlak wat dit verteenwoordig het, moontlik gemaak. ‘n Verdere voordeel is dat dit bewys het dat fraktale analisemetodes toepaslik is vir die bestudering van seevlak enkelpunt tydreeks data.

Tweedens is die tye wanneer lang golfaksie teenwoordig was in die hawens by Saldanha en Ngqura, vasgestel deur die uitwerking daarvan in die hawens.

Derdens is enkelpunt tydreeks data wat deur die WNNR aangeteken is vir die vasgestelde tydperke, sowel as twee dae voor elke tydperk, verkry en is fraktale dimensiestelle vir elke tydperk vasgestel.

Vierdens is die fraktale datastelle van albei die hawens vergelyk om te bevestig dat die stelle dimensies vir bedreigende seetoestande duidelik verskil van die vir nie-bedreigende toestande, en dus geskik is om die seetoestand te beskryf.

Ten slotte is die fraktale dimensiestelle vir bedreigende seetoestande in die twee hawens vergelyk om enige verskille tussen hulle te bepaal.

Na voltooiing van die navorsing en analise is ander gebiede van kusingenieurswese behalwe die bepaling van bedreigende gebonde infragravitasie golf seetoestande, identifiseer waar multifraktale geometrie ook tot voordeel aangewend kan word.

Acknowledgements

It has taken a number of years to complete this research and I have enjoyed each one of them. During the time I have met a large number of highly qualified academic and professional persons, as well as many other specialists, who have been kind, generous and interested enough to give of their time and expertise to assist me in my work. I am indebted to them all and especially to the following:

My family, Sue, Sharon and Michael have been a continuous source of encouragement and support to me. Sue, my wife has been close to me throughout all of my research and I have really appreciated her love and presence during my studies. Sharon, our daughter and Michael, our son have followed my progress with an interest that has been heartening.

Ian, my brother has never failed to listen to my ideas and to discuss analytical issues with me.

Brian Ingpen, has shown a keen interest in my work and its progress and has introduced me to many of his good friends in the shipping industry

Paul Liu and Eddie Bosman have been mentors to me, and I thank them for their interest and support for my work. I have enjoyed our discussions very much.

Geoff Toms, my Supervisor has kept me focused in my work. He has also been kind enough to introduce me to his colleagues in the Applied Mathematics Department and at Deltares in the Netherlands.

Alex Babanin has been a great inspiration to me, and without him, I may well have given up on my research. Alex has given me a great deal of advice and input, never hesitating to meet when we could at conferences or send me technical papers, or introduce me to his broad range of international colleagues.

Sarel Schoeman and Captain's Eddie Bremner and Peter Stowe, all gave up time to share their invaluable experiences of Port Operations with me.

Thanks also to Marius Rossouw of the CSIR for his ongoing interest in my work, and to Gerhardus Diedericks and Luther Terblanche of the University of Stellenbosch for the calculation of the mathematically derived time series used in the research.

Table of Contents

DECLARATION……..……..i
ABSTRACT……..……..……..ii
OPSOMMING……..…….....v
ACKNOWLEDGEMENTS……..……..viii
TABLE OF CONTENTS……....x
LIST OF FIGURES……..xiv
LIST OF TABLES…….……..……xix
1 INTRODUCTION 1
1.1 Infragravity waves 1
1.2 Long waves in Table Bay and Saldanha Bay 6
1.3 Analysis of sea surface displacements..... 7
1.4 Problem statement 8
1.5 Hypothesis 9
1.6 Study aim 10
1.7 Approach..... 10
1.8 Constraints 14
1.9 Overview of chapters 14
1.10 Summary of Chapter 1 15
2. HAZARDOUS LONG WAVE ACTION ON THE WEST AND SOUTH EAST COASTS OF SOUTH AFRICA 17
2.1 Introduction..... 17
2.2 Moored ship motions and the parting of moorings during long wave action 17
2.3 Long wave actions at Saldanha Bay and Ngqura Harbours 22
2.3.1 Typical incidents of mooring failures in Saldanha Bay Harbour 24

2.3.2 Typical incidents of mooring failures in Ngqura Harbour 28
2.4 Description of Saldanha Bay and Ngqura Harbours 30
2.4.1 Saldanha Bay Harbour (Latitude 33^{o} 02' South and Longitude 17^{o} 58' East) 30
2.4.2 Ngqura Harbour 38
2.4.3 (Latitude 33^{o} 46' South and Longitude 25^{o} 40' East) 38
2.5 Summary of Chapter 2 42
3. LITERATURE REVIEW OF FRACTALS 43
3.1 Fractal structure and dimensions 43
3.2 Fractal dimensions 46
3.2.1 The scaling dimension (D) 47
3.2.2 The Hurst exponent (H) 49
3.2.3 Hausdorff Dimension 51
3.3 The fractal structure of ocean wave systems 51
3.4 Methods of fractal analysis 54
3.4.1 Overview of fractal physics 54
3.5 Measurement of fractals 64
3.5.1 Rescaled Range method 66
3.5.2 Multifractal Detrended Fluctuation Analysis (MDFA) method 68
3.5.3 The Fourier power spectra density (PSD) method of analysis 68
3.5.4 Wavelet transform methods 70
3.5.5 Wavelet scaling method 76
3.5.6 Wavelet Transform Modulus Maxima (WTMM) method 78
3.5.7 Singularity power spectrum 79
3.6 Summary of Chapter 3 81
4. DATA SELECTION 82
4.1 Length of series 82
4.2 Data used in analysis 84

4.3 Sequential video images of a fully dimensioned open lake water wave field 85
4.3.1 Recording of spatial wave field images. 85
4.3.2 Analysis of open lake water spatial data frames 87
4.4 Mathematically generated bound long wave time series 90
4.5 Saldanha Bay Harbour time series data 91
4.6 Ngqura Harbour time series data 92
4.7 Summary of Chapter 4 93
5. ANALYSIS OF MEASUREMENT DATA 94
5.1 Analysis software 94
5.1.1 Spreadsheet models 94
5.1.2 MATLAB toolboxes and script files 94
5.2 Open lake water spatial wave field time series 95
5.2.1 General 95
5.2.2 Time Domain analysis 100
5.2.3 Frequency Domain 104
5.3 Analysis of mathematically generated time series 108
5.3.1 General 108
5.3.2 Time Domain Analysis 109
5.3.3 Frequency Domain analysis 111
5.4 Analysis of Saldanha Bay time series 113
5.4.1 Wave data on the 26th and 28th September 2013 113
5.4.2 Time Domain analysis 115
5.4.3 Frequency Domain analysis 121
5.5 Analysis of Ngqura Harbour time series 132
5.5.1 Wave data on the 6 /7 and 8 August 2012 132
5.5.2 Time Domain analysis 134
5.5.3 Frequency Domain analysis 139

5.6 Comparison of Wavelet Transform Modulus Maxima configurations for Saldanha Bay Ngqura harbours 149

5.7 Multifractal Detrended Fluctuation Analysis (MDFA) of longer term time series . 155

5.8 Analysis of period averaged singularity power distribution 156

5.9 Summary of Chapter 5 163

6. FINDINGS 164

6.1 Evaluation of fractal analysis methods 164

6.2 Proof of Hypothesis 164

6.3 Conventional wave characteristics of Saldanha Bay and Ngqura Harbours 165

6.4 Fractal dimensions and indices for bound infragravity wave (BIW) sea states at Saldanha Bay and Ngqura Harbours 166

6.5 Comparison of singularity spectra for hazardous BIW sea states in Saldanha Bay and Ngqura Harbours 169

6.6 Probability of non-exceedance of local Holder exponent values 172

6.7 Comparison of singularity spectral power groups in non-hazardous and hazardous BIW sea states in Saldanha Bay and Ngqura Harbours 175

6.8 Summary of Chapter 6 178

7. CONCLUSIONS 179

7.1 The ocean wave continuum and sea surface geometry 179

7.2 Summary of findings 180

7.3 Summary of contributions 181

7.4 Future research 182

List of Figures

Page

Figure 1: Degrees of ship motions 18
Figure 2: Plan showing the localities of the Port of Saldana and the Port of Ngqura. 23
Figure 3: Typical mooring layout for a capsize bulk carrier 24
Figure 4: Chart layout of Saldanha Bay Harbour, including bulk terminals 30
Figure 5: Oil tanker and bulk iron ore carrier shown at their terminals. 32
Figure 6: Typical iron ore bulk carriers shown at the iron ore terminal 32
Figure 7: Dyneema mooring ropes 33
Figure 8: Typical details of a hook mooring installation. 34
Figure 9: Satellite image showing the location of the waverider buoy at Saldanha Bay Harbour. 35
Figure 10: Typical screen capture of general wave data: (Hs, Hmax and forecast data) 37
Figure 11: Typical screen capture of long wave height. 38
Figure 12: Chart layout of Ngqura Harbour 39
Figure 13: View of the container terminal in Ngqura Harbour 40
Figure 14: Typical screen capture of general wave data (Hs), (Hmax) and wave height forecasts) 41
Figure 15**:** Typical screen capture of long wave height with forecast Long Wave height. 42
Figure 16: Illustration of self-affine structure in a sea surface displacement time series 45
Figure 17: Euclidean dimensions 48
Figure 18: Illustration of Holder exponent values for a typical time series 50
Figure 19: Diagrammatic representation of ocean wave fractal system 52
Figure 20: Sequential circles encapsulating numbers of squares 55
Figure 21: Log-log plot radii and of Σ values 56
Figure 22: Fractal time series continuum 59
Figure 23: Typical singularity spectrum 62
Figure 24: Cumulative frequency / probability on non-exceedance 63
Figure 25: Typical bounded time series 65
Figure 26: Variations in range for segments of a typical time series 66
Figure 27: Breakdown of time series into subsegments and elements 67
Figure 28: Plot of β values for long term short-term correlation 70

Figure 29: Graph of Morlet wavelet 71
Figure 30: Graph of dilated and translated Morlet wavelets..... 72
Figure 31: Diagram of a typical continuous wavelet transform structure. 73
Figure 32: Diagram of wavelet filtering process 74
Figure 33: Time series of a typical sea surface displacement sequence. 75
Figure 34: Mesh plot of the percentage energy in each wavelet coefficient 75
Figure 35: Contour plot of percentage energy in each wavelet coefficient 76
Figure 36: Typical power spectral density plots in the wavelet domain with average scaling exponents. 77
Figure 37: Schematic detail of the wavelet modulus maxima line configuration..... 79
Figure 38: Singularity power spectrum envelopes of typical time series. 80
Figure 39: Typical camera set-up for capturing of stereoscopic video imagery..... 86
Figure 40: (a), (b), (c), (d), (e) and (f): Typical sequential series of digital sea surface Model scenes. 88
Figure 41: Three-dimensional topographic and contour maps of the sea surface, showing breaking wave conditions 89
Figure 42: Diagram showing how spatial images and time series data can be derived from the stereoscopic video record of the breaking wave sequence 90
Figure 43: Diagrammatic layout of the analysis grid which was superimposed on the wave field. 96
Figure 44: Time Series of surface displacements on grid co-ordinates (25,10), (25,110) and (25, 210)..... 98
Figure 45: Time series on grid co-ordinate (225,210) with selected wave filed images 99
Figure 46: Scatter plot of rescaled range values of open lake water wave field data 100
Figure 47: Singularity spectra for the single point time series on grid coordinates (25,110), (225 110) and (425 110) 101
Figure 48: Singularity and relative frequency of occurrence..... 103
Figure 49: Cumulative frequency or probability of non-exceedance curves..... 104
Figure 50: Power spectral density plots of time series. 105
Figure 51: Log-log plot of power spectral density plots..... 105
Figure 52: Spectral exponent in the wavelet domain..... 106
Figure 53: Time series plot of 12sec(Series1) 108
Figure 54: Time series plot of 12sec(Series1) 108

Figure 55: Time series plot of 18sec(Series1) 109
Figure 56: Singularity spectra for time series 12sec(Series1), 12sec(Series2) and 18sec(Series1) 110
Figure 57: Continuous wavelet Transform of 12sec(Series1) time series 111
Figure 58: Continuous wavelet Transform of 12sec(Series2) time series 111
Figure 59: Continuous wavelet transform plots of 18sec(Series1) time series.....112
Figure 60: Time series plot at Saldanha Bay on 26th September 2013 at 09:00 113
Figure 61: Time series plot at Saldanha Bay on 28 September 2013 at 09:00 113
Figure 62**:** Rescaled range values for 280 data segment of data on the 26 September 2013.115
Figure 63: Scatter plot of rescaled range values of 280 data 116
Figure 64: Comparative rescaled range (R/S) values for the Hurst exponent for 26 and 28 September 2013. 117
Figure 65: Comparative singularity spectra plots for the 26 and 28 September 2013.....119
Figure 66: Holder exponent probabilities of non-exceedance for Saldanha Bay on the 26 and 28 September 2013. 121
Figure 67: Power spectral density envelopes in the Fourier domain for time series of 26 and 28 September 2013. 122
Figure 68: Log-log plot of power spectral density plots for time series of 26 and 28 September 2013 123
Figure 69: PSD plots of the time series in the wavelet domain. 124
Figure 70: Continuous wavelet transform plots of time series on the 26 September 2013 ...125
Figure 71: Continuous wavelet transform plots of time series on the 26 September 2013 ...126
Figure 72: Continuous wavelet transform and modulus maxima chains for time series recorded at 09:00 on the 26 September 2013.....127
Figure 73: Continuous wavelet transform and modulus maxima chains for time series recorded at 09:00 on the 28 September 2013.....128
Figure 74: Continuous wavelet transforms and modulus maxima chains for 180 seconds of time series recorded at 9:00 on the 28 September 2013 130
Figure 75: The singularity power spectral envelopes for the time series on 28 September 2013 131
Figure 76: Time series of sea surface displacements at Ngqura Harbour on 6 August 2012 and 10:30 h 132

Figure 77: Time series of sea surface displacements at Ngqura Harbour on 8 August 2012 and 10:30 h. 132
Figure 78: Scatter plot of rescaled range values: 6 and 7 August 2012. 134
Figure 79: Scatter plot of rescaled range values: 8 August 2012. 135
Figure 80: Comparative plots of average R/S values for 6 and 8 August 2012 136
Figure 81: Comparative singularity spectra plots for 6/7 August and 8 August 2012 137
Figure 82: Power spectral density plots for time series of 6/7 and 8 August 2012 139
Figure 83: Log-log plot of power spectral density plots for time series of 6 and 8 August 2012 140
Figure 84: Wavelet scaling exponent 141
Figure 85: Continuous wavelet transform of time series at Ngqura on 6/7 August 2012. 143
Figure 86: Continuous wavelet transform of time series at Ngqura on 8 August 2012 144
Figure 87: Continuous wavelet transform and modulus maxima chains of time series records at 21:00 on 6 August 2012. 145
Figure 88: Continuous wavelet transform and modulus maxima chains of time series records at 21:00 on 8 August 2012. 145
Figure 89: Continuous wavelet transform and modulus maxima chains of 250 time series records at 21:00 on 8 August 2012 146
Figure 90: Singularity spectral power envelopes for Ngqura 148
Figure 91: Comparative singularity and wavelet modulus maxima spectra for Saldanha Bay on 26 September 2013 151
Figure 92: Comparative singularity and wavelet spectra for Saldanha Bay on 28 September 152
Figure 93: Comparative singularity and wavelet spectra for Ngqura 153
Figure 94: Comparative singularity and wavelet Spectra for Ngqura 154
Figure 95: Singularity Spectra of Long Term Time Series 155
Figure 96**:** Period averaged singularity power spectra (5 to 15 seconds) for Ngqura Harbour on 8 August 2012 157
Figure 97: Period averaged singularity power Spectra (5 to 15 seconds) for Saldanha Bay Harbour on 22 June 2013 158
Figure 98: Period averaged singularity power Spectra (5 to15 seconds) for Saldanha Bay Harbour on 25 June 2013 159

Figure 99: Period averaged singularity power spectra (5 to 15 seconds) for Saldanha Bay Harbour on 13 August 2013.....160
Figure 100: Period averaged singularity power spectra (5 to 15 seconds) for Saldanha Bay Harbour on 18 August 2013.....161
Figure 101: Period averaged singularity power Spectra (5 to 15 seconds) for Saldanha Bay Harbour on 28 September 2013 162
Figure 102: Singularity spectra for both Saldanha bay and Ngqura harbour 170
Figure 103: Holder exponent (h) values for non-hazardous sea states at Saldanha Bay and Ngqura Harbours.....172
Figure 104: Holder exponent (h) values for hazardous sea states at Saldanha Bay and Ngqura Harbours.....173
Figure 105: Singularity power distributions at Saldanha Bay and Ngqura Harbours.....176

List of Tables

Page

Table 1: Matrix of domains and methods of analysis with fractal dimension 13
Table 2: Suggested maximum surge amplitudes for dry- and liquid bulk carriers as well as container ships 19
Table 3: Maximum surge amplitudes for different mooring line types and resonant wave periods in San Pedro Bay study. 20
Table 4: Maximum amplitudes for 100 per cent efficiency of container ship loading 21
Table 5: Updated maximum significant wave amplitudes for 100 per cent efficiency of container ship loading 22
Table 6: Details of broken and extra mooring lines 26
Table 7: Parted mooring schedule for period June to 28 August 2013 at Saldanha Bay Harbour [ref: Port Control at Saldanha Bay and Capt. P Stowe] 27
Table 8: Details of typical instances of long wave action at Ngqura Harbour. (Stuart. 2013) 29
Table 9: Bulk terminal drafts at Saldanha Bay 31
Table 10: Bulk terminal drafts at Ngqura Harbour 40
Table 11: Radii of circles and number of encapsulated squares 56
Table 12: Time series characteristics identified by Hurst exponent values 60
Table 13: Standard deviation of Hurst exponents derived from short series. 83
Table 14: Mathematically generated time series parameters 91
Table 15: Saldanha Bay Harbour data record details 92
Table 16: Ngqura Harbour data record details 93
Table 17: Coordinates of time series in open lake water wave data 97
Table 18: **Comparison of spectral scaling exponents** 107
Table 19: Significant wave heights (Hm0) and Peak frequencies (fp) 114
Table 20: Summary of fractal indices for singularity spectra on the 26 and 28 September 2013 120
Table 21: Significant wave heights (Hm0) and peak frequencies (fp) 133
Table 22: Summary of fractal indices for singularity spectra on the 6 /7 August and the 8 August 2012. 138
Table 23: Comparative significant wave heights, peak frequencies and peak periods 165

Table 24: Fractal dimension and indices for hazardous BIW sea states at Saldanha Harbour. 167
Table 25: Comparison of fractal dimensions and Hurst exponents for the ocean surface and for vertical sea surface displacements.....168
Table 26: Range of the following fractal indices for both Saldanha Bay and Ngqura harbours during hazardous sea states.....171
Table 27: Probabilities of non-persistence and persistence at Saldanha Bay and Ngqura Harbours.....174

1 INTRODUCTION

1.1 Infragravity waves

The stochastic dynamics of the sea surface and infragravity waves have been a matter of keen interest and research for many years. Munk (1949) and Tucker (1950) found that there was a strong correlation between swell and infragravity waves and it was thought that the swell caused the latter waves (Herbers et al. 1995). Longuet-Higgins and Stewart (1962) proposed that second order infragravity waves are generated by non-linear frequency difference interactions between pairs of swell components; they suggested that the trapped infragravity waves are somehow released from the generating wave group systems when the latter break in the shallower waters at the shoreline (Herbers et al. 1995). Once released, the waves were either reflected back from the coast as seaward travelling free leaky waves, or they travelled along the coast as free edge waves, trapped by refraction within the breaker zone. The difference between the aforementioned free wave systems depends principally on the angle of incidence on the incoming forced wave systems.

Infragravity waves cannot be visually detected because of their very low amplitudes, which are generally in the order to 100 to 300 mm, and frequencies in the order of .04 to .004 Hz (Herbers et al. 1995). Their vertical displacements and frequencies cannot be measured directly from the time series data collected at typical tethered waverider buoy installations as this instrumentation can only accurately record waves with minimum frequencies in the order of .03 Hz (periods in the order of 30 seconds). Infragravity waves can only be accurately measured by relatively sophisticated instrumentation mounted on the sea floor.

Surface elevations on a wave group scale were first linked to infragravity waves by Munk in 1949 and by Tucker in 1952 (Roelvink and Reniers, 2012), and in 1992 Okihiro et al noted that infragravity waves with typical periods of 25 to 200 seconds were coupled to groups of incident waves with typical periods of 4 to 25 seconds (Okihiro et al. 1992).

Wave groups have the subject of a great deal of research and it is well known that the water level in an area where high seas are grouped together tends to be lower than in an area of smaller waves, where it is higher (Goda, 2010). This difference in water level is caused by local variations in radiation stress, which is related to the transfer of additional momentum flux associated with wave groups. (Goda, 2010, Longuet-Higgins and Stewart, 1960 and 1964).

Infragravity waves are generally classified as either:

- Incoming, group bound, waves, or
- Outgoing, free, leaky waves, or
- Alongshore, free, edge waves.

One possible mechanism for the generation of incoming infragravity waves, which are bound to higher frequency wave groups, is the weak non-linear interaction between linear free waves Biesel (1952); Longuet-Higgins and Stewart (1960 and 1962) and Hasselmann (1962)(Okihiro. 1992)

Hasselmann (1962) identified that the principle forcing mechanism in the generation of infragravity waves is nonlinear quadratic interactions between swell waves (Thomson et al. 2007).

Radiation stresses in gravity wave systems with non-uniform amplitudes are another possible means for the generation of incoming infragravity waves (Longuet-Higgins and Stewart 1962). Laboratory tests on infragravity waves induced by wave groups in shallow water have shown that there was a good correlation between theoretical and measured values (Roelvink et al. 1992).

Longuet-Higgins and Stewart (1962) hypothesised that outgoing free infragravity waves were generated by the reflection of the mass transported by the incoming wave groups after the waves themselves had broken on the beach, but this hypothesis was not theoretically justified in any way (Oltman-Shay and Hathaway, 1989). Outgoing infragravity waves could also be generated by the slow modulation of the breakpoint (Symonds et al. 1982).

Sand (1982) observed that natural wave fields were usually represented by unidirectional wave trains in order to determine a first approximation of the characteristics of the wave field. He went on to note that long waves were usually modelled in the same way as unidirectional systems. In order to obtain a second order model for long waves, he derived three-dimensional expressions and transfer functions for group-induced long waves (Sand, 1982). The aforementioned derivations are based on the earlier work of Bowers (1977) and Hansen (1978) who proposed a one-dimensional solution of the Laplace equation for long waves (Sand. 1982).

Gallagher (1971) proposed that alongshore edge waves were generated by incoming waves with specific directional distributions and they are understood to be resonantly excited by the incoming wave fields (Okihiro et al. 1992). These waves either remain trapped along the coast by both refraction and reflection or they escape into deep water as leaky waves.

Okihiro and Guza (1996) found that infragravity waves can also be generated by Tsunamis (Thompson et al. 2007).

Laboratory testing to confirm whether or not a varying break point could generate free seaward travelling infragravity waves was inconclusive although, laboratory tests did confirm Gallagher's proposed mechanism for the generation of alongshore waves (Bowen and Guza, 1978) (Okihiro et al. 1992).

Notwithstanding the fact that the mechanism for the generation of free infragravity waves is unclear, bound waves, edge waves and reflections have all been detected in field observations at the shoreline (Okihiro et al. 1992).

Edge waves can be described mathematically as follows (Oltman-Shay and Hathaway, 1989):

$$\eta(x,y,t)=A\phi(x)\cos(ky-wt)$$

where: η = sea surface elevation

x, y = cross = shore and longshore coordinates

x = 0 at the shoreline and increases offshore

t = time

A = edge wave amplitude

ϕ = crosshore amplitude function

$$k=\frac{2\pi}{L}$$

$$\omega=\frac{2\pi}{T}$$

k and w = longshore wavenumber and radial frequency

L and T = longshore wavelength and period

Edge waves can have a number of modes and on a plane beach with slope β, the modes satisfy the following relation (Oltman-Shay et al. 1989):

$$\omega^2=gk\sin(2n+1)\beta \text{ for } n=0,1,2\ldots\ldots \text{ and } 2(n+1)\beta<2\pi:$$

where g=gravitational acceleration, and n=mode number

The 0^{th} edge mode has the smallest longshore wavelength while the highest mode has the longest wavelength with a wavenumber equal to the deep water wave number of $k=\omega^2/g$. This effectively means that edge waves remain trapped in shallow water. Using the same logic one can say that edge waves with wave numbers $k<\omega^2/g$ effectively become leaky waves returning to deep water (Oltman-Shay and Hathaway 1989).

It is interesting to note that both leaky and edge waves have components that are generated by reflection from the shoreline and that they both have standing structures comprised of nodes and anti-nodes in the cross-shore direction.

Freilich and Guza (1984) developed nonlinear, unidirectional models of shoaling gravity waves based on variations of the Boussinesq equations (Elgar and Guza, 1985). The models incorporate coupled evolution equations for the derivation of both the amplitudes and phases of the temporal Fourier modes of the wave field (Freilich and Guza, 1984). The aforementioned processes broaden the frequency spectrum as energy is transferred to higher and lower frequencies; this is the result of frequency sum, f1+f2, and frequency difference, f1-f2, interactions between two component waves f1 and f2. In addition to broadening the spectrum, these interactions also couple the phases of the wave components causing waves to steepen and pitch forward (Herbers et al. 2003).

The two-equation stochastic model proposed by Kofoed-Hansen and Rasmussen (1998) agrees with wave height measurements of ($H_{m0)}$ and wave periods (T_0), and predicts the non-resonant interactions as well as the transfer of energy to the lower harmonics very accurately.

Mathematical models of incoming long waves in shoaling waters have been a fairly recent development into the study of the phenomenon. One of these models that is broadly used for the analysis of infragravity waves in shallow water is XBeach.

Roelink et al designed XBeach in 2009 (Buckley and Lowe, 2013) and is comprised of a coupled, phase averaged, spectral model for swell as well as a non-linear shallow water model for infragravity waves. This makes the model very versatile which is able to process the combined effects of depth integrated 2D wave groups together with their associated infragravity wave systems (Roelink et al. 2009).

Other nearshore models include SWASH and SWAN (Buckley and Lowe 2013).

All of the above models are able to determine bulk sea swell wave heights over steeply sloping seabed profiles, but XBeach is the only one able to forecast bulk infragravity wave heights and spectral transformations (Buckley an Lowe . 2013).

The amplitude of long waves has been found to be proportional to the narrowness of the wave frequency spectrum with higher wave amplitudes being associated with a more peaked spectrum (Harkins and Briggs (1994); Sand, 1982). This characteristic of long waves is particularly interesting insofar as it relates directly to the study of long

waves around the South Africa coastline where the seas have typically been known to be narrow banded spectra. The long waves also cause excessive moored ship motions, which have a significantly negative impact on the efficiency of harbour operations around the coast.

1.2 Long waves in Table Bay and Saldanha Bay

In 1953 Wilson published the findings on his research into the occurrence of Seiches in Table Bay leading to long wave action in Duncan Dock. He concluded that Table Bay was subject to low frequency Seiches with significant amplitudes and he found that they did not occur together with swells, nor were they caused by seismic events. However he noted that there was a positive correlation between these and those occurring in Port Elizabeth, as well as with local barometric oscillations in both centres. He also found that the frequency of the Seiches was in the range from 'one or two to about 15 occasions per year' (Wilson, 1953).

Seiches are another type of long wave system that is no less interesting than infragravity waves. Seiches are long period standing waves that are either formed in completely enclosed water areas, such as lakes, or in partially enclosed water areas, such as open bays or harbours open to the sea. In the former case either atmospheric pressure variations, or wind, or both generate them, and in the latter case they are principally generated by long waves from the open sea (Rabinovich, 2008).

Botes et al. (1982) found that waves with frequencies from .005 Hz to .02 Hz occurred at the end of the Duncan Dock's main breakwater in Table Bay most of the time (CSIR Report C/SEA 8023, 1980). This finding was based on the analysis of short and long wave data collected in Table Bay and at the cooling water intake for the Koeberg Nuclear Power Station. Short waves, with periods of 1 to 30 seconds, were recorded with a waverider buoy and long (infragravity) waves with periods of 50 to 110 seconds were recorded with a pressure transducer. In his report, Botes found that up until 1982 long wave data in South Africa was 'virtually non-existent' and he noted that there was an urgent need for a better knowledge of the origin and generation of long waves (Botes et al. 1982).

Long wave action in Duncan Dock ceased to be a problem with the construction of the outer Ben Schoeman Dock in 1975 and other infrastructure changes within Duncan Dock.

Saldanha Bay Harbour was constructed during the period from 1973 to 1976 and since then it has been exposed to long wave action. A field study of moored ships in Saldanha Bay was carried out by the CSIR in 1987 and in 2003 Moes presented a paper on 'Storm conditions and long waves along the coast of South Africa', which incorporated details of the phenomenon in Saldanha Bay.

In 2003 Van Giffen et al. compared a simulated set of long wave conditions in Saldanha Bay harbour with measured records. They found that the energy levels of the two data sets were comparable, but there were significant variations between the locations of the derived spectral peaks.

More recently, in 2009 Van der Molen and Moes published a paper on 'General Characteristics of South African Ports and the Safe Mooring of Ships', which also incorporated references to Saldanha Bay.

In 2006, C Soler, a postgraduate student at Delft University of Technology carried out research into the topic of swell and wave-groups at Saldana Bay. His work was based on the analysis of storm data and the use of a numerical model SURFBEAT, which models the propagation of long waves generated by swell seas to determine the wave energy distribution in Saldanha Bay Harbour.

The Ports in South Africa are generally exposed to long-period wave energy, which are generated by swell wave groups (Rossouw et al. 2013). This finding was concluded after data collected from those Ports, which were known to experience ship-mooring problems associated with long wave action, had been analysed.

1.3 Analysis of sea surface displacements

In 1980 Funke and Mansard identified that sea surface displacements could only be adequately simulated by combining frequency distributions derived from variance

spectral density, S(f), criteria with the wave grouping 'phenomenon' (Funke and Mansard, 1980).

Funke and Mansard developed the Smoothed Instantaneous Wave Energy History (SIWEH) model for the synthesizing of irregular waves that included wave groups. The model describes the wave group activity in a wave train in an alternative way to the 'envelope functions' (Funke et al. 1980).

The SIWEH method of analysis describes the temporal variation of energy in a wave train, but it fails to give any information of the spectral components within the train. On the other hand, the Fourier analysis method is a well-established technique for the global spectral analysis of wave trains, but it does not give any information on the temporal distributions of the spectral energy within a wave train. This shortcoming is overcome to some degree by the Short Term Fourier Transform (STFT) method of analysis, which does give information on the temporal distribution of spectral energy in a wave train, but this is based on a single window size which limits its resolution at different frequencies. This shortcoming is in turn overcome by the Continuous Wavelet Transform (CWT) method of analysis providing both local frequency and temporal distributions in a wave train (Schlurmann, 2002).

This research will include both Fourier and CWT methods of analysis.

1.4 Problem statement

Incoming infragravity waves are a significant hazard to moored shipping operations in both the Saldanha Bay and Ngqura harbours. This hazard leads to the following risks:

- Loss of revenue or delays to Port operations due to shipping companies declining to use harbour specific mooring ropes during in-port periods,

- Injury and/or loss of life during re-mooring operations that have to be undertaken when moorings part during vessel loading operations,

- Loss of time and delay costs when vessel loading has to be stopped while the hazardous conditions prevail,

- Loss of time and delay costs when ships have to abort loading and leave the quayside, as well as the harbour during loading.

It would be reasonable to expect that the characteristics of sea states, such as surface roughness measured by a waverider buoy would be different at Saldanha Bay and Ngqura harbours, due to their different types of exposure to the open ocean and long swell environments, but there is currently no way of quantifying the different characteristic.

A better understanding of the geometric characteristics of sea states associated with bound infragravity wave systems around the South African Coastline can only stand the Coastal and Port Engineering professions in a better stead for both the optimising of port operations and for the planning and design of new works in areas that are affected by this hazard.

Holthuijsen (2008) has observed that:

> wave conditions may well be similar in the sense that the significant wave height and period are equal, but they may still be very different in detail: a mixed sea state of wind sea…….and swell …….. may have the same significant wave height and period as a slightly higher wind sea without swell. To distinguish such conditions more parameters are needed.

He goes on to say that 'any small number of parameters would not, in general, completely characterise the wave conditions', and he proceeds with a discussion of spectral analysis.

1.5 Hypothesis

Sae sates associated with incoming infragravity waves bound by surface wave groups are multifractal systems that can be geometrically characterised and described in terms of both their fractal dimensions and the distribution of their singularities enabling one to:

- Characterise, quantify and describe different infragravity wave systems,

- Make comparisons between different infragravity wave sea states.

1.6 Study aim

The aim of this research is to characterise the sea states related to infragravity wave systems on the basis of the shape of vertical sea surface displacements.

Fractal dimensions are considered to be an appropriate method for the study of sea state geometrics because they are closely associated with, and inextricably linked to, the structure of constituent wave groups.

The abovementioned wave groups are expected to have characteristically self-similar geometric shapes that constitute fractal systems and that could be used to characterise bound infragravity wave sea states.

Particular fractal dimensions and singularity distributions that could be used to profile a sea state comprising hazardous Bound Infragravity Waves (BIWs) will be identified.

All of the analysis used in the research will be based on the same single point time series data that is currently being used for the conventional spectral analysis processes that are required for the planning and design of coastal and port engineering works.

1.7 Approach

This research will be based on the fact that short waves and swell, with periods of 4 to 25 seconds, are known to exist together with infragravity wave systems, with periods of 25 to 200 seconds. The sea state wave trains are non-stationary features that are better analysed over shorter time segments than those normally used for the analysis of infragravity waves *per se*, provided that the length of the series being analysed contains sufficient samples to represent the sea state.

The hypothesis will be tested by determining and comparing the fractal properties of the following sets of times series data collected from both Saldanha Bay and Ngqura harbours:

- A set of data collected during an identified period of known long wave action.

- A set of similar data collected two days before the abovementioned period of long wave action.

In the case of Saldanha Bay, the above sets of data will be comprised of records collected at 3 hourly intervals over a 15 hour period during which time 26 moorings were broken and 4 new moorings were laid.

Similarly, two sets of data will be used for the analysis of Ngqura Harbour conditions during a period when a vessel broke a mooring line and long waves were recorded outside the harbour.

The fractal properties of the two sets of analysis at each harbour will be compared in order to identify any variances or typical characteristics that may have been present and could be used to differentiate between hazardous and non-hazardous sea states.

Similarly, comparisons will be made between the fractal properties of the hazardous sea states at each of the harbours in order to identify any characteristic variances that could be used to differentiate and categorise the different harbour locations.

The null hypothesis will be proven if either of the different sets of data was not fractal, or there were no significant differences between the fractal dimensions and the singularity distributions of the two sets of data at each harbour.

In order to validate the use of the proposed fractal analysis techniques for the analysis of sea surface displacement data, they will first applied to the analysis of time series data collected from spatial video imagery of an open water wave field on the Great Lakes of the USA. This process will enable the relation of fractal geometric dimensions to video imagery of the representative wave field.

The different fractal analysis techniques that will used to analyse the time series data have been shown in Table 1 together with details of the domain of the analysis, the method of analysis and the fractal dimensions that were derived for each set of data.

The fractal dimensions used in the research will be derived by the following methods of analysis:

- The rescaled range (R/S) method,

- The Multifractal Detrended Fluctuation Analysis (MDFA) method,
- The Power Spectral Density (PSD) method in both the Fourier and the wavelet domains, and
- The Wavelet Transform method

Table 1: Matrix of domains and methods of analysis with fractal dimension

Domain of Analysis	Method of Analysis		Fractal Dimensions						
			Hurst exp.	Fractal Dim.	Hausdorff Dim.	Holder exp.	Singularity Spectrum	Persistence Exponent	Singularity Distribution
Time Domain	Rescaled range (R/S)		H	D					
	Multifractal Detrended Fluctuation (MDFA)		H	D	D(h)	h	SS		
Spectral Domain	Fourier Transform Analysis (1/f) scale							β	
	Wavelet Transform Analysis	(1/f) scale						β	
		Modulus Maxima							SD

1.8 Constraints

A significant initial constraint to the scope of this research has been the difficulty in obtaining records and details of incidents involving either excessive ship motions or the parting of moorings. This information was required in order to benchmark an occurrence of a typical hazardous bound infragravity wave sea state.

The constraint was removed to some degree after the time and details of one incident had been obtained from a Shipping Agency in Saldanha Bay. Once this had been done and the topic of this research had gained credibility, access was gained to other incidences and locations for analysis.

The constraint has resulted in the fact that that the research is based on the analysis of a very limited number of incidences.

1.9 Overview of chapters

Chapter 1 provides an introduction to the research that includes the problem statement, the hypothesis and the research methodology.

Chapter 1 introduces the topic of infragravity wave systems and the previous research that has been carried out into the analysis of infragravity waves on the west coast of South Africa and elsewhere. The chapter concludes with details of the problem statement, the hypothesis, the study aim, the approach and the constraints of the research

Chapter 2 covers general details of moored ship motions as well as typical details of hazardous long wave action at Saldanha Bay an Ngqura Harbours.

The chapter also includes details of the relevant Infrastructure, Systems and Wave reporting methods at both harbours.

Chapter 3 is comprised of a literature review of fractal structures and dimensions before continuing to discuss the methods that have been used for the derivation of the fractal dimensions in the research, including the following:

- The Rescaled Range (R/S) and Multifractal Detrended Fluctuation Analysis (MFDA) methods used in the time domain, and
- The Spectral analysis in the Fourier and wavelet domains, and
- The Continuous Wavelet Transform analysis in the time-frequency domains.

Chapter 4 provides details of the measurements that were selected for the research. These measurements are comprised of open lake water time series data, as well as open seawater single point time series data from both Saldanha Bay and Ngqura harbours.

Chapter 5 covers the analysis of the measurement data, providing details of the analysis software, the results of the analysis for the open lake water and the Saldanha Bay and Ngqura harbours.

Chapter 6 deals with the findings of the research including the state of fractal physics research, details of Saldanha Bay and Ngqura harbours, conventional wave characteristics of open lake water as well as Saldanha Bay and Ngqura harbours; fractal dimensions and indices of open lake water wave field as well as Saldanha Bay and Ngqura harbours. The chapter goes on to confirm the research objectives and methodology before comparing the fractal dimensions of hazardous bound infragravity wave sea states in Saldanha Bay and Ngqura harbours.

Chapter 8 sets out the conclusions of the research insofar as the ocean wave continuum and sea surface geometry is concerned before summarising the findings and contributions of the research. Finally the chapter includes details for future research.

1.10 Summary of Chapter 1

Chapter 1 introduces the research by outlining previous work carried out in connection with the analysis of long wave systems in Table Bay as well as in Duncan

Dock and Saldanha Bay Harbours. The introduction also refers to infragravity waves and alternative methods for the analysis of wave trains incorporating wave groups.

The chapter gives details of the problem statement, which will be addressed in the research, and records the hypothesis, study aim, approach and constraints that form basis for this research.

2. HAZARDOUS LONG WAVE ACTION ON THE WEST AND SOUTH EAST COASTS OF SOUTH AFRICA

2.1 Introduction

van der Molen and Moes (2009) researched the safe mooring of ships in South African ports, and they concluded that long wave action was the cause of the mooring problems in Saldanha Bay. They established that this action was caused by long wave energy that was focused on the harbour jetty area and noted that the solution developed to mitigate the effects of the wave action was comprised of the optimisation of mooring line configurations at the quayside.

Rossouw et al. (2013) compared the significant heights of short waves recorded by the waverider buoy at the entrance to Saldanha Bay Harbour with those of the long waves recorded by a pressure sensor on the last caisson at the end of the harbour jetty. The correlated data was found to contain some scatter, together with an interesting lower envelope function. In the published paper it was proposed that the envelope represented the bound long waves and that the scatter was caused by free long waves, which may also have entered the bay. In the published paper it was noted that the data would also have included long waves reflected from the shore inside the bay.

2.2 Moored ship motions and the parting of moorings during long wave action

Moored bulk carriers in Saldanha Bay harbour are subject to surge, sway and yaw motions while moored container ships in Ngqura harbour are subject to excessive surge motions. These motions are shown in red in Figure 1 where they have been recorded together with the other typical ship motions in the six degrees of freedom.

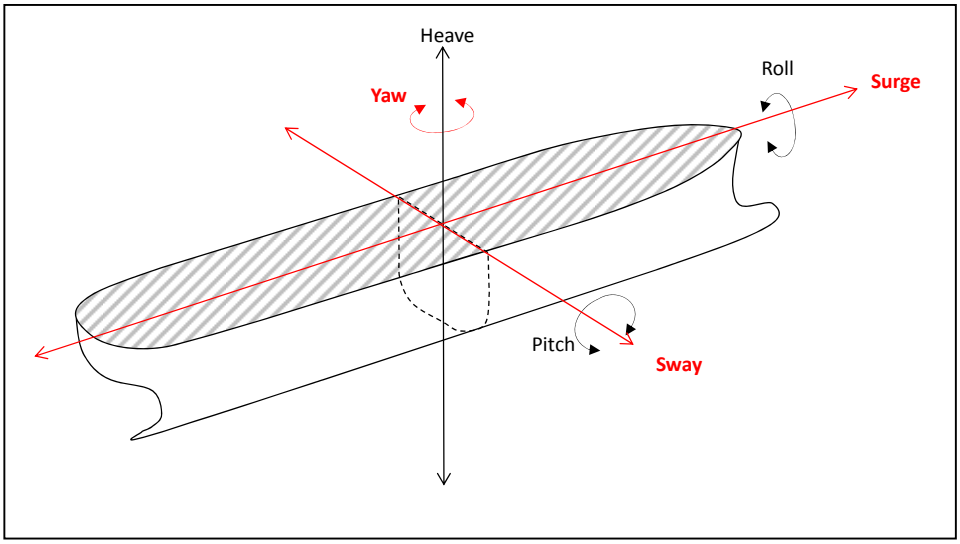

[Ref: Introduction in Ship Hydrodynamics]

Figure 1: Degrees of ship motions

Moored bulk carrier and container ship systems, comprising the ship with its moorings and fenders, have natural response periods ranging from 20 seconds to minutes and they resonate with loads applied in this frequency range (van Oorschot. 1976). These loads can be exerted by non-linear interactions between the vessels and low frequency group bound long wave systems, comprising both the fundamental bound wave and the constraining wave groups (Grant and Holboke, 2004).

The natural periods of free sailing ships are different to those of moored ships and long wave systems do not have a significant impact on these vessels.

Excessive moored ship motions due to long wave action have a significantly negative impact on berth downtime and the efficiency of loading operations. Criteria for the (Un)Loading of Container Vessels has been researched in depth by an International Working Group convened by the Maritime Navigation Commission (MarCom) which is a part of The World Association for Waterborne Transport Infrastructure (PIANC). The Working Group has drafted a set of recommended criteria for maximum allowable ship motions, which are based on both a procedural and a numerical analysis of container handling operations. These recommendations are included in

PIANCs Report No. 115-2012, which was published in 2012. This report found that the type of container or spreader placing criteria had a significant effect on loading efficiencies and allowable ship motions, because of their different geometrical placing tolerances.

Earlier research by Yuen (1986) defined berth downtime as 'the length of time that mooring capacity limits are exceeded', and he has suggested that berth downtime is a function of the following criteria:

- Vessel motions
- Mooring Line Loads
- Fender deflection and hull pressure

It has been suggested that bulk carrier and container ship motions, in excess of the values given in Table 2, should be considered to be excessive (Yuen 1986).

Table 2: Suggested maximum surge amplitudes for dry- and liquid bulk carriers as well as container ships

Type of Ship	Maximum Surge Amplitude for 100 % Efficiency of Loading
Dry Bulk Carrier	1.52 m
Liquid Bulk Carrier	3.05 m
Container Ship	0.15 m

[Ref: Yuen, 1986]

Yuen carried out a ship motion and mooring analysis study for planned new harbour works to be constructed in San Pedro Bay, California in (Yuen, 1986) in order to evaluate moored ship responses for different mooring configurations as a function of wave period. The study was based on the assumption that the most critical waves would be approaching the moored vessel directly from the stern, and the computed maximum surge displacements for different types of mooring lines and resonant wave periods, are shown in Table 3.

Table 3: Maximum surge amplitudes for different mooring line types and resonant wave periods in San Pedro Bay study.

Description of vessel	**Mooring line types**	**Resonant Wave Period (seconds)**	**Maximum Surge Amplitude (metres)**
Dry-bulk carrier (Post Panamax: 100 00 DWT)	Dacron (Polyester) Steel	190 40	.65 .27
Oil Tanker (265 000 DWT)	Dacron (Polyester) Steel	210 80	.39 .64
Container Ship (Panamax)	Dacron (Polyester) Steel Dacron and Steel	120 30 70	.62 .22 .46

[Ref: Yuen 1986]

Polyester (Dacron type) mooring lines have similar benefits to those of Nylon, from the point of view of strength (twice that of natural fibre) and resistance to wear, but they have markedly less elasticity. Mooring ropes of High Modulus Polyester (HMPE) (Dyneema Fibre type) have not been included in the summary in Table 8 but they are stiffer than Polyester, with 25 per cent to 30 per cent of the extension at breaking (Boesten, 2014).

Surge is the most critical motion from the point of view of loading and unloading of container vessels because the ship-to-shore cranes are not able move along the quay to accommodate the surging ship motions. Detailed numerical modelling has shown that this constraint has a significant negative impact of loading efficiencies (Moes et al.

undated). Maximum vessel motion amplitudes, based on the input from researchers including Jensen (1990), Smitz (1992), D'Hondt and Moes (2000) are illustrated in Table 4 (Moes and Terblanche, undated).

Table 4: Maximum amplitudes for 100 per cent efficiency of container ship loading

Principle Motion	Jensen et al, 1990	Smitz, 1992	PIANC, 1995	D'Hondt, 1999	Moes, 2000
Surge	0.5 m	0.5 m	0,5 m	0.24 m	0.3 m
Sway	0.4 m	0.3 m	0.6 m	0.22 m	0.3 m
Heave	0.45 m	0.3 m	0.4 m	0.20 m	0.3 m
Roll	1.5 deg	1 deg	1,5 deg	0.24 deg	0.5 deg
Pitch	0.75 deg	-	0.5 deg	0.4 deg	0.5 deg
Yaw	0.25 deg	-	0.5 deg	0.1 deg	0.5 deg

[Ref: Moes, H)

D'Hondt's criteria are the most stringent and are based on the container cell and pin tolerances.

In 2012, the PIANC working group updated their criteria detailed in Table 4, and the new criteria for maximum allowable significant motion amplitudes have been listed in Table 5.

Table 5: Updated maximum significant wave amplitudes for 100 per cent efficiency of container ship loading

Principle Motions	Maximum Significant Motion Amplitudes
Surge	0.2 to 0.4 m
Sway	0.4 m
Heave	0.3
Roll	1.0 deg
Pitch	0.3 deg
Yaw	0.3 deg

[PIANC Report Number 115-2012]

The criteria derived by Moes in Table 4, are based on the following:

- The placing tolerances of containers,
- The avoidance of along quay crane movements, to accommodate surge,
- The significantly longer periods of transverse vessel motions (surge, sway and yaw) in comparison with the rotational motions (heave, roll and pitch) (Moes et al. undated).

2.3 Long wave actions at Saldanha Bay and Ngqura Harbours

Infragravity waves have always been a particular concern in the Port of Saldanha Bay[1], on the West Coast, and The Port of Ngqura [2] on the South-East coast, because of their action on moored bulk carriers and container ships. A locality Plan, showing the position of the harbours can be seen in Figure 2.

[1] Also referred to as Saldanha Bay Harbour
[2] Also referred to as Ngqura Harbour

Ref: Mainport Africa website

Figure 2: Plan showing the localities of the Port of Saldana and the Port of Ngqura.

In 2003 Van Giffen et al carried out research at Saldanha Bay harbour to investigate the use of an existing numerical wave model, which had been developed for the simulation of long waves generated by grouped short waves in a semi-enclosed bay or harbour, to forecast long waves at the harbour. The forecast data was compared to measured long wave data recorded in the harbour.

Waverider buoy data, collected from a site immediately outside the harbour entrance was used as input for the model.

Van Giffen found that the model's forecasts for the overall energy generated by the wave systems in the harbour correlated fairly well with those derived from the measured data. However, he found that there was no significant correlation between the peak frequencies of the forecast and measured data.

2.3.1 Typical incidents of mooring failures in Saldanha Bay Harbour

A typical mooring configuration for a Cape size bulk carrier has been shown in Figure 11 and details of the broken and the additional mooring lines are given in Table 3.

Headlines, stern lines and breast lines are typically comprised of polypropylene rope with the forward and stern springs being made of steel wire rope. The head and stern mooring lines stabilise the vessel against the quay, while the breast lines prevent the ship from breaking away from it. The springs are the primary stabilisers against longitudinal forces.

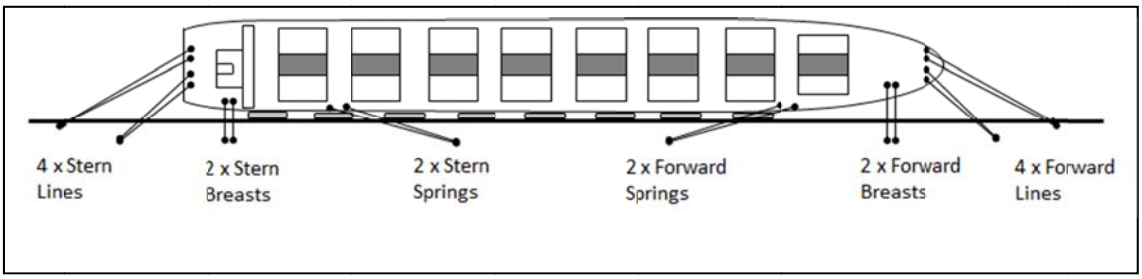

Figure 3: Typical mooring layout for a Cape size bulk carrier

The combined effects of the wave dynamics in the harbour cause moored bulk carriers to move in a typical ‘figure of eight motion’, (Interview with S Schoeman on 27 November 2013) and this motion was the main cause of one of the most significant instances of mooring failures at the terminal on the 28 September 2013.

During this incident 26 mooring lines on the bulk carrier Taurus, a Capesize vessel (170 000 DWT), were broken during loading over a 13.5 hour period from 07:00 hours to 20:30 hours. In addition, four new mooring lines were added during this time.

Experienced personnel on the vessel at the time of the incident have reported that the estimated dominant wave period during the incident was ‘somewhere between 30 and 50 seconds’, and that vessel was subjected to a ‘figure of eight’ yawing motion with

the bow and stern alternately moving away from the quay by some 4.0 to 6.0 m metres.

Details of mooring lines that either broke or were replaced on the vessel are given in Table 6.

Table 6: Details of broken and extra mooring lines

Time	Parted Mooring Lines	Extra mooring lines
07:00 to 08:30	2 x breast lines forward 2 x breast lines aft 2 x short stern lines	
09:12 to 10:42	1x breast line forward	1 x breast line forward 1 x breast line aft
12:24 to 13:30	3 x stern lines 1 x extra stern lines	
13:36 to 14:00		1 x line forward
15:12 to 15:42	1 x stern line 1 x breast line aft 1 x breast line forward	
16:24 to 16:54		1 x headline forward
17:06 to 17:36	1 x stern line	
17:34 to 19:36	1 x forward breast line aft 1 x headline 1 x breast line aft 3 x stern lines	
19:42 to 20:30	4 x stern lines aft 1 x breast line	

[Ref: S Schoeman: Details from vessel mooring log sheet]

A schedule of incidents involving broken moorings for the period from the 20 June 2013 to the 28 August 2013 has been given in Table 7.

Table 7: Parted mooring schedule for period June to 28 August 2013 at Saldanha Bay Harbour [ref: Port Control at Saldanha Bay and Capt. P Stowe]

Vessel	**Date**		**Waverider Buoy Wave Heights**		**Long Wave Height (recorded on outer caisson)**	**Parted Mooring lines**
			Significant Wave Height	Maximum Wave Height		
	(Month)	(Day)	(metre)	(metre)	(centimetre)	
Cape Heron	June 2013	20th	2.3	3.9	10	1 x Fwd. Breast
Anangel Innovation		21st	2.6	3.7	14	1x Aft. Breast 1 x Fwd. Breast
		22nd	2.7 2.6 2.0 2.1	4.5 4.1 3.1 3.3	15 32 12 15	1 x Stern 1 x Fwd. Spring 1 x Stern 1 x Stern
CPO Europe		23rd	1.7	3.0	10	1 x Head
Azul Victoria		25th	2.9	5,2	15	1 x Aft. Breast
Southern Wisdom	July 2013	27th	2.8	4.3	13	2 x Head
Angel ll		29th	1.7	3.0	7	1 X Fwd. Breast
Pacific Canopus	August 2013	12th 13th 14th	1.6 2.8 2.5	2.4 4.0 4.3	8 20 15	1 x Aft. Breast 1 x Aft Breast 1 x Aft Breast
Braverus		18th 19th	2.5 1.7	4.4 2.9	30 6	1 x Aft. Breast 1 x Aft Breast
Golden Queen		27th	3.1	4.8	18	1 x Head

Standard operating procedures in the harbour provide for two tugs to be mobilised to steady a vessel during re-mooring but if it the tugs are required to return for a second attendance, the vessel is required to leave the quayside and the harbour (Interview with Capt. P. Stowe (31 March. 2014).

2.3.2 Typical incidents of mooring failures in Ngqura Harbour

The ability to load container ships at Ngqura harbour is governed by excessive horizontal ship motions, which either lead to the vessels becoming unmanageable from the point of view of container crane loading, or to the parting of moorings (Stuart, 2013). The most significant of the aforementioned ship motions is the surge motion. The ship-to-shore cranes cannot effectively manage this motion due to the fact that the cranes are not able to respond to accommodate the rapid ship movements. A crane must hold its position and wait for a surging ship to pass and return to the point where a container can be placed in the cell guides, or stacks, before it passes through the window (Moes et al. Undated). Details of long wave action and the harbour have been detailed in Table 8.

Table 8: Details of typical instances of long wave action at Ngqura Harbour. (Stuart. 2013)

Date	Time-Vessel Instability	Vessel Name & Description	Description	Mooring Arrangement	Reported Condition
8 August 2012	-	MSC Natalia	Broke mooring line	Not available	Long waves measured outside port. Over 0.3 m height.
2 August 2011	-	MSC Adriatic	Disruption of loading	Not available	
1 August 2011	-	-	Excessive vessel motion, no line breaking but difficult conditions to load. Main movement was surge of up to about 1.0 m	Mooring arrangements were reasonable but with polyprop ropes	-
7 July 2011	At night	MSC Zambia	Experienced surge in about 5 knot wind. Port claims fender damage.	5-3 configuration both ends. 3 out of 5 stern lines were near new. 4 lines had a good lead of 50m aft and one with a short lead of 20 m. 3 spring lines had a lead of 30m fwd. Polypropylene ropes.	Long waves measured in port. 110 s to 230 s ranges. Above 25cm height. Little wind.
7 July 2011	General complaint	General complaint	Excessive vessel movement	Not available	
23 April 2010	From 10h00 on 23rd to 15h00 on 24th	Mol Destiny (LOA 260 m), GRT 39 906)	Broke 6 lines	Not available	Hs over 3 m, Tp over 12 s
23 April 2010	01h00 to 15h00	MSC Marinor (LOA 304m GRT 73 819)	Broke 6 lines aft (stern lines and aft spring) and 2 fwd springs, whilst working at the berth. During unberthing snapped 1 spring.	Fwd 4 headlines, 1 breast line, 3 springs aft, 4 stern lines, 2 breast lines and 3 springs	Hs over 3 m, Tp over 12s

2.4 Description of Saldanha Bay and Ngqura Harbours

2.4.1 Saldanha Bay Harbour

(Latitude 33^{o} 02’ South and Longitude 17^{o} 58’ East)

2.4.1.1 Harbour layout

Saldanha Bay Harbour is situated on the exposed west coast of South Africa, where it is directly open to the ocean. A layout of the harbour has been shown in Figure 4.

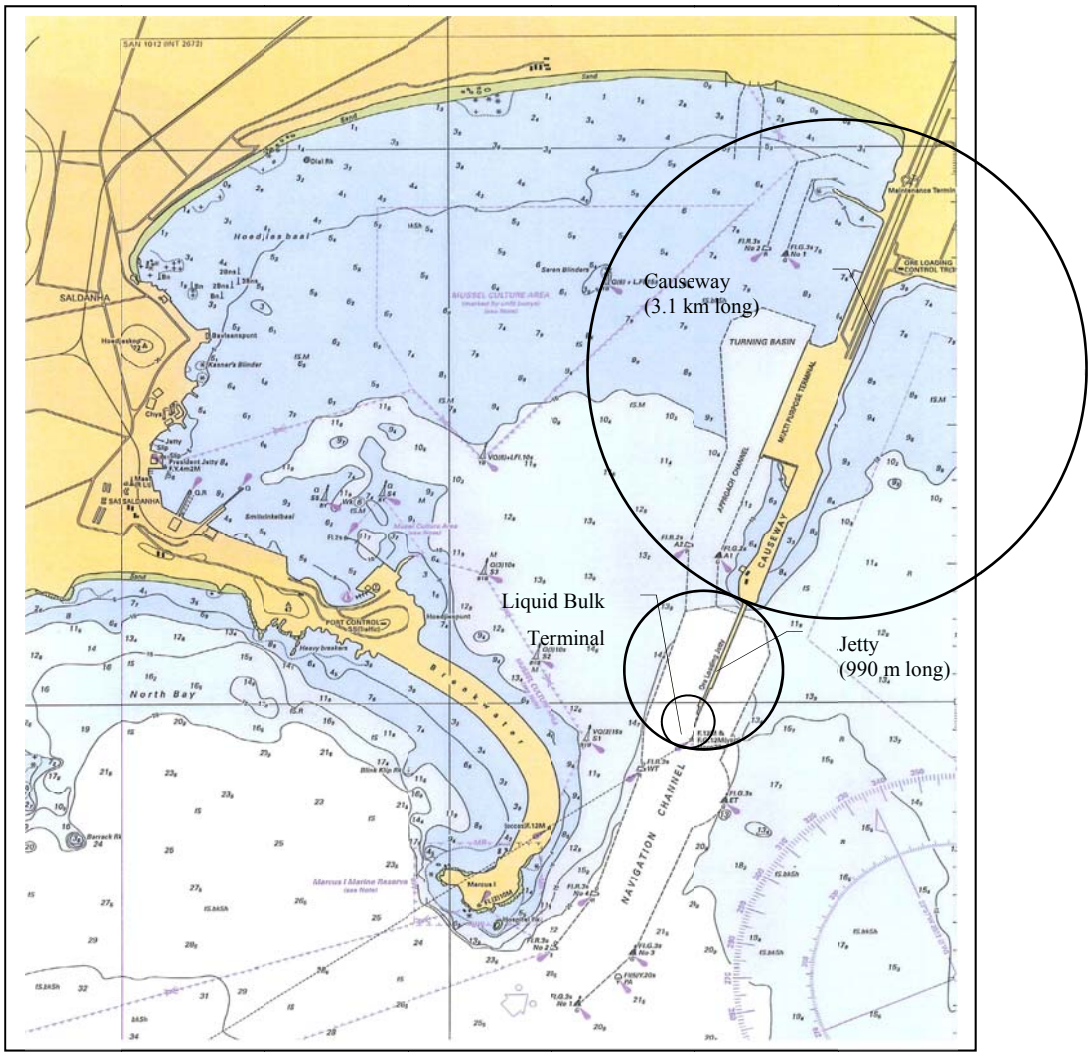

[Ref: SAN 1011]

Figure 4: Chart layout of Saldanha Bay Harbour, including bulk terminals

2.4.1.2 Bulk terminal facility

The bulk terminal complex at Saldanha Bay is shown inside the circles in Figure 7. It comprises a 630 m long iron ore and liquid bulk jetty (inside the smallest circle), close to the end of a 990 m long jetty (inside the middle size circle), and connected to the shore by a 3.1 km long causeway/breakwater (inside the largest circle).

The allowable draughts at the bulk terminals have been shown in Table 9.

Table 9: Bulk terminal drafts at Saldanha Bay

Terminal	Draft alongside quay	Maximum Permissible Draft
Ore Terminal	23.0 m	21.5 m
Tanker Terminal	23.2 m	21.5 m

[Ref: Transnet National Ports Authority website and Port Information and Port Operating Guidelines]

The liquid bulk and iron ore terminals have been shown in Figure 5 and two typical bulk carriers have been shown at their berths at the iron ore terminal, in Figure 6.

[Ref: shippingmovements.co.za website]

Figure 5: Oil tanker and bulk iron ore carrier shown at their terminals.

[Ref: Portstrategy.com]

Figure 6: Typical iron ore bulk carriers shown at the iron ore terminal

2.4.1.3 Mooring ropes and systems

Dyneema mooring ropes with quick release hook mooring systems similar to the typical details shown in Figures 7 and 8, have been installed at the terminals in order to mitigate the risk of broken moorings due long wave action, as described below.

[Ref: dyneema.com website]

Figure 7: Dyneema mooring ropes

Dyneema ropes are 15 times stronger than steel rope, on a weight-for-weight basis, and this makes them very effective for handling and ship mooring operations. Dyneema ropes are also safer than other ropes for the mooring of ships as the rope retracts in linear fashion, without the danger of backlash or snaking, if it is parted. This characteristic of the ropes mitigates, to some degree, the risks associated with parted moorings.

Quick release Hook Mooring systems, can be designed to measure and record both the tension forces in vessel mooring lines and any changes in the specified values caused by environmental loading due to the action of long waves, winds and tides. Typically, data from the system can be monitored to continuously assess the efficiency of the mooring layout and to initiate appropriate action to ensure that the specified capacities of the mooring system are maintained at all times. In this way, the risk due to partial or total breakout of a moored vessel can be significantly reduced.

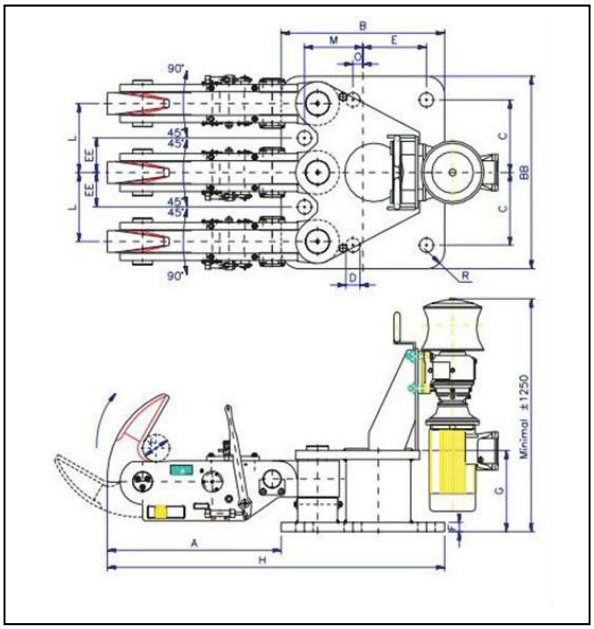

[Ref: alibaba.com website]

Figure 8: Typical details of a hook mooring installation.

Senior staff at Saldanha Bay are on round-the-clock attendance on the decks of the tankers during their loading operations and overloading of the mooring system can normally be obviated by the implementation of quick release mechanisms incorporated into the mooring hook assemblies.

Standard operating procedures at Saldanha Bay require that bulk carriers should be loaded in such a way that they can safely leave the quayside and the protection of harbour at any time during loading operations (Stowe P, Interview 31 March 2014). Ships must be kept under power during loading in order to leave the quayside at short notice if required to do so (Transnet Port Information and Operating Guidelines, 2009).

Long wave action at the harbour generally occurs during the winter months of May to August (Transnet Port Information and Operating Guidelines, 2009).

2.4.1.4 Wave recording and reporting methods

Open water wave data is recorded in real time by a waverider buoy located in an exposed environment at the entrance to the harbour, and long wave data inside the harbour is recorded at the outer caisson at the bulk terminal.

The waverider buoy is tethered in 23.0 metres of water at the location shown on the satellite image in Figure 9.

[Ref: Google Earth]

Figure 9: Satellite image showing the location of the waverider buoy at Saldanha Bay Harbour.

The waverider buoy measures and records the sea surface elevation, and Port Control measures and records the following meteorological data:

- Wind Speed
- Wind direction
- Air temperature, and
- Barometric pressure

The wave criteria governing whether or not ships are allowed to enter the harbour are currently being determined on the basis of the spectral analysis of the sea surface displacement data in the Fourier domain. This analysis is based on linear theory involving the addition of sinusoidal waves, and the assumption that the displacement data is stationary.

The abovementioned calculations are being applied very usefully, but they are limited insofar as derivation of long wave data is concerned, because the waverider buoy recording the raw data cannot directly record waves with periods in excess of 30 minutes.

The wave conditions and swell heights, as well as other meteorological data for the harbour is collected, processed and reported on by the CSIR. The reports are presented in close to real time on the Internet.

Typical screen captures of the general and long wave data at the harbour are given in Figures 10 and 11.

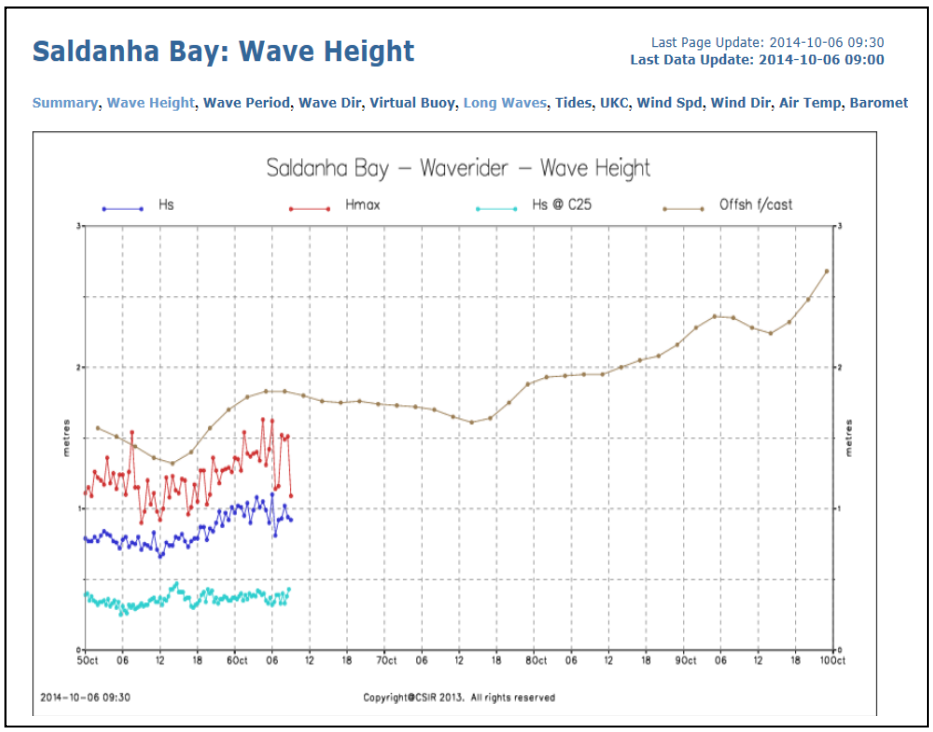

Ref: CSIR wavenet website

Figure 10: Typical screen capture of general wave data: (Hs, Hmax and forecast data)

The long wave heights recorded at the outer caisson of the bulk terminal are shown in Figure 11.

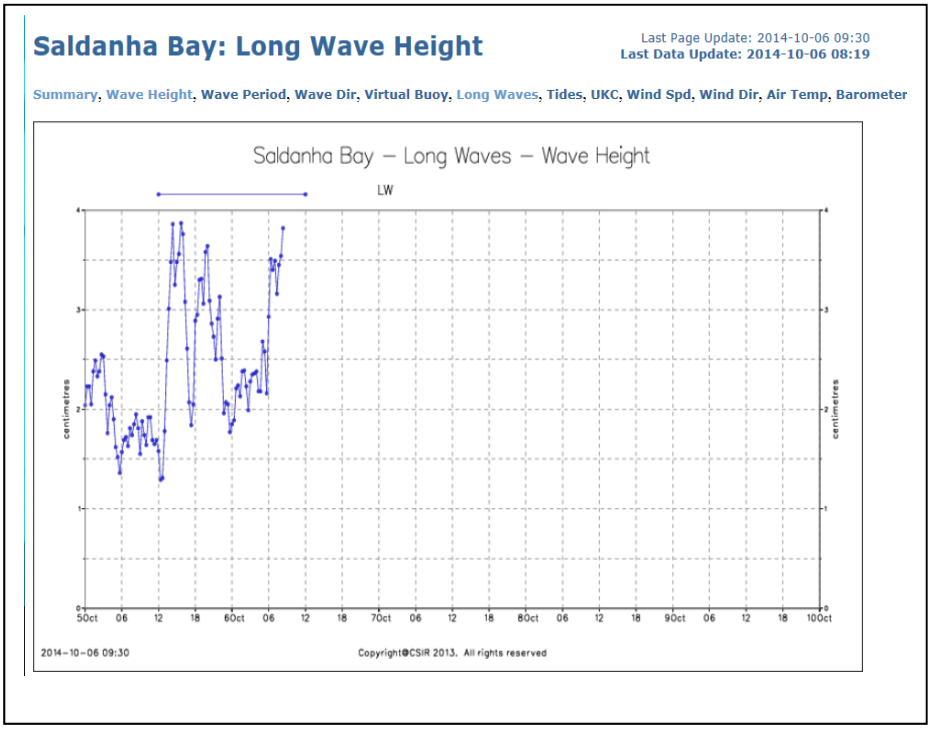

Ref: CSIR wavenet website

Figure 11: Typical screen capture of long wave height.

2.4.2 Ngqura Harbour (Latitude 33^{o} 46’ South and Longitude 25^{o} 40’ East)

2.4.2.1 Harbour layout

The harbour is situated inside Algoa Bay, on the South East coast of South Africa, and a section of chart showing its layout has been shown in Figure 12.

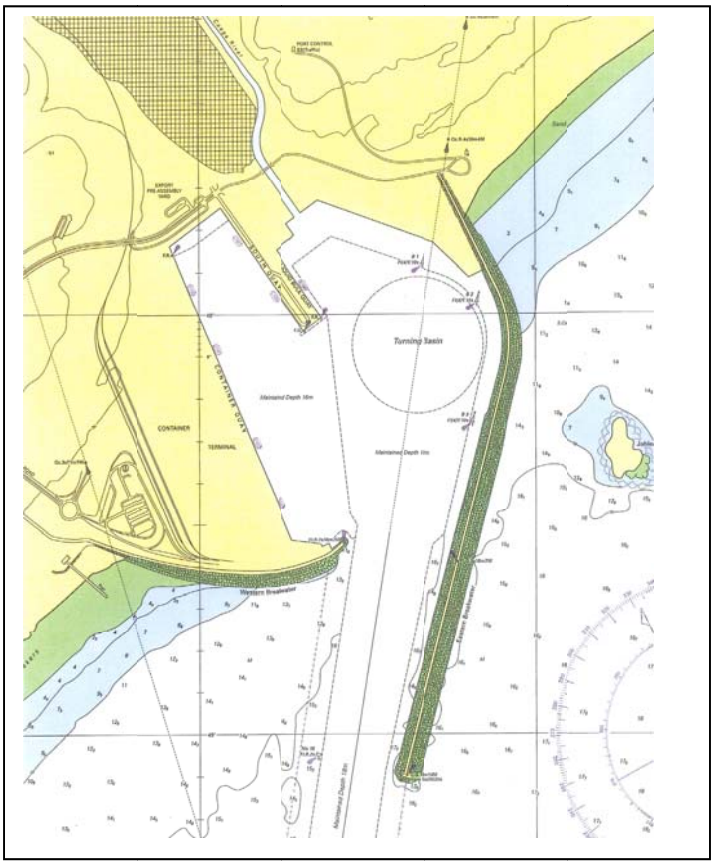

[Ref: SAN 1026]

Figure 12: Chart layout of Ngqura Harbour

A typical view of the container terminal at the harbour has been shown in the photograph in Figure 13.

Ref: Ports.co.za website

Figure 13: View of the container terminal in Ngqura Harbour

Details of the quay lengths and drafts alongside the quays at the Container Terminal have been given in Table 10.

Table 10: Bulk terminal drafts at Ngqura Harbour

Terminal	Quay Length	Maximum Permissible Draft
Container Terminal	780 m	16.5 m
Tanker Terminal	432 m	18 m

[Ref: Transnet National Ports Authority website]

The sea state outside Ngqura Harbour is monitored in real time by a waverider buoy moored 2 km off the end of the breakwater in 21.0 m depth of water. Typical screen captures of both the general wave and long wave details at the harbour are given in Figures 14 and 15.

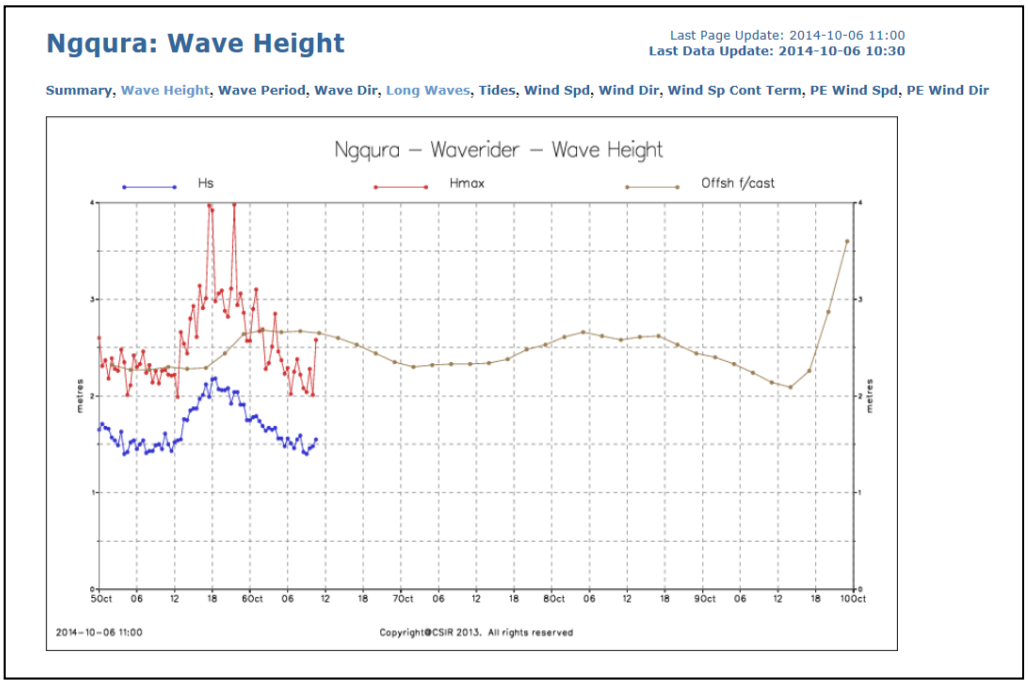

[Ref: CSIR wavenet website]

Figure 14: Typical screen capture of general wave data (Hs), (Hmax) and wave height forecasts)

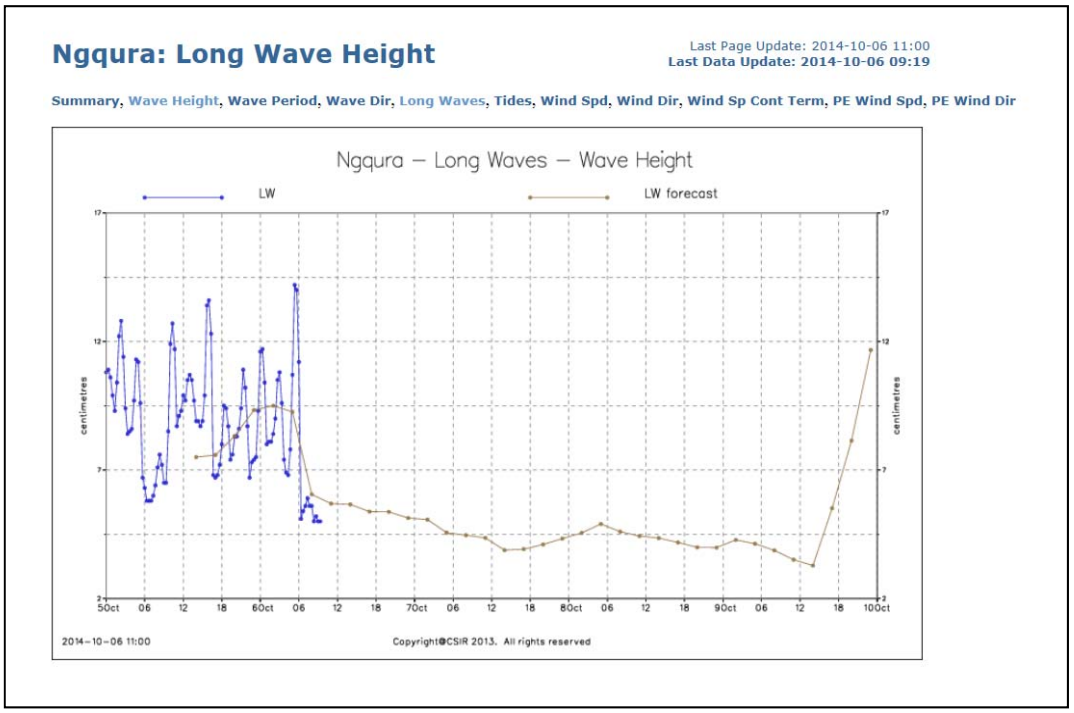

[Ref: CSIR wavenet website]

Figure 15**:** Typical screen capture of long wave height with forecast Long Wave height.

2.5 Summary of Chapter 2

Chapter 2 provides an overview of moored ship motions as well as typical details of hazardous long wave action at Saldanha Bay and Ngqura Harbours.

The chapter goes on to describe the relevant details of infrastructure and mooring systems as well as methods for the recording and reporting of wave data in the harbours.

3. LITERATURE REVIEW OF FRACTALS

3.1 Fractal structure and dimensions

Sea surface roughness is caused primarily by wind and wind-generated waves. Typically the roughness occurs over a range of degrees from highly irregular, choppy, seas to longer, smoother, swells. Many features of this roughness continuum, including their self-similar structures, can be visually observed in the time series records of sea surface displacements.

These self-similar structures are characteristic of fractal structures and the rest of this chapter will cover the formal aspects of fractal structures including their dimensions and methods of measurement.

The term ‘fractal’ is derived from the Latin adjective *fractus* and it is related to the verb *frangere*, meaning ‘to break’; to create irregular fragments. Scaling laws based on statistical self-similarity have been studied since the early 1900s; Mandelbrot first coined the term ‘fractal’ for a set of scaled characteristics with a non-integer dimension.

The concepts of Fractal Mathematics and Physics were developed in response to the need to be able to measure and describe properties that lay between formal Euclidean Geometry and chaos. In 1989 Mandelbrot wrote that fractal geometry ‘promises to be effective in Engineering’ (Mandelbrot, 1989). He went on to write:

> *Self-styled sophisticates tend to either forget or spurn the needs of the practical man (Engineer). One reason is that he (the Engineer) does not have the luxury of waiting until the phenomena he chooses or is asked to try and control have been explained to the satisfaction of the sophisticates. Instead he finds himself lost in Galileo’s dark labyrinth’ where he does not even know what signs to look for or what to measure (sic)*

According to Hughes (1995), the concept of fractal structures and sets is applicable to a wide range of highly irregular, self-similar[3] or self-affine[4], shapes and structures ranging from clouds and rain areas (Lovejoy and Mandelbrot, 1985) to the geometry of rolled-up paper balls (Cambou and Menon, 2011). In 1967 Mandelbrot demonstrated that the measured length of a coastline was in fact a fractal and depended on the scale, or length, of the straight-line segment used to measure it.

A fractal structure could comprise such elements as lengths and areas, as well as a number of singularities and can typically be described as a function of the scales of their measurement (Lopes and Betrouni, 2009).

A time series of sea surface displacement data has a fractal structure as it displays self-similar structures, which remain apparent at different scales of observation. This characteristic of the series has been illustrated in Figure 16, where the lower series are similar subsets of the original top series, at different scales in one direction only.

[3] Self-similarity: Where a part of an object is a reduced scale of the whole object in all directions.

[4] Self-affine: Where a part of an object is a reduced scale of the whole object in different directions

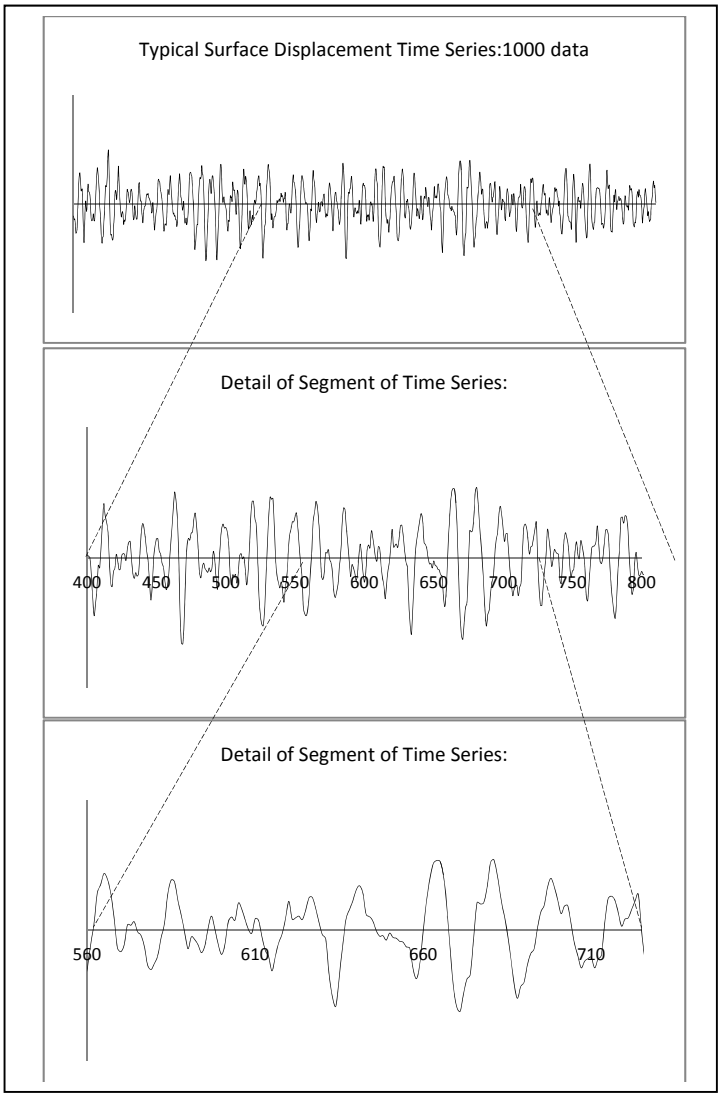

Figure 16: Illustration of self-affine structure in a sea surface displacement time series

Fractal dimensions of fractal sets, systems or structures allow the description, quantification and comparison of common characteristics such as the linearity, irregularly, complexity and singularity of different systems (Xiong et al. 2012).

The fractal physics of ocean surfaces and sea states has not received very much attention since the early work carried out by Phillips (1958), Longuet-Higgins (1994), Stiassnie (1988, 1991), and Elgar and Mayer Kress, (1989). More recent work on a

two-dimensional fractal model of the sea surface was carried by Berizzi and Pinelli in 1997, and fractal solutions to the long wave equations were investigated in by Ajiwibowo in 2002. Furthermore, Ozger worked on the analysis of the multifractal properties of significant wave heights in 2011. This work was based on data collected at 24 sites on the West Coast of the USA.

In contrast, the medical profession has carried out a great deal of recent research into the fractal analysis of time series in the fields of Cardiology, Physiology and Neurology. This work has been spearheaded by Lopes and Betrouni (2009), Babinec et al. (2005), Ihlen (2012), Eke et al. (2012), Deligniers et al. (2011), Shimizu et al. (2004) and Riley et al. (2012).

In addition to the above, research for this dissertation has found that a considerable amount of attention has also been given to the fractal analysis of financial markets.

3.2 Fractal dimensions

Fractal dimensions can be comprised of either integer, or non-integer values depending on whether they represent deterministic shapes or random structures occurring in nature (Hughes, 1995). Euclidean geometric systems can be analysed in a strictly statistical sense on the basis of formal geometry and dimensions such as mean and variance (Eke et al. 2012). However, this does not apply to natural fractal structures, and series, which depend on both the scales of observation and related power law functions (Lopes and Betrouni 2009).

Fractal dimensions can relate to either the geometry or the occurrence of singularities of a form and they include the Scaling Dimension (D), the Hurst exponent (H), the Holder exponent (h) and the Hausdorff Dimensions (Dh), the latter being a function of the Holder exponent. These dimensions allow one to quantify and compare common characteristics of similar fractal systems or structures. They are all different to the more conventional Topological or Euclidean dimensions of length, area and volume, and therefore they need to be defined very differently as set out and discussed below.

3.2.1 The scaling dimension (D)

The scaling dimension (D) can be defined for a topographic set Ω, which can be subdivided into smaller geometrically similar sets, R, which can be made congruent with Ω by multiplication with a magnifying factor M, as follows (Hughes, 1995):

$$D = \frac{\log(\text{number of sets})}{\log(\text{multiplication factor})} = \frac{\log(R)}{\log(M)}$$

Scaling dimensions can be used to measure the dimension of Euclidean lines, areas and cubes, as well as shapes and sets, and their application to the former system is illustrated as follows:

- A line of unit length can be sub-divided into two halves, or geometric replicas as shown in Figure 17, which can be made equal to the original line by magnifying by 2. In this case both R and M would both be equal to 2.

  In terms of the above definition of scaling dimension of the line would be:

  $$D = \frac{\log(R)}{\log(M)} = \frac{\log(2)}{\log(2)} = 1$$

- Similarly a square with unit side lengths can divided into 4 geometric replicas, as shown in Figure 17, with a scaling dimension of:

  $$D = \frac{\log(R)}{\log(M)} = \frac{\log(2^2)}{\log(2)} = 2$$

- Similarly a cube with unit side length, breadth and height can be divided into 8 geometric replicas, as shown in Figure 17, with a scaling dimension of:

  $$D = \frac{\log(R)}{\log(M)} = \frac{\log(2^3)}{\log(2)} = 3$$

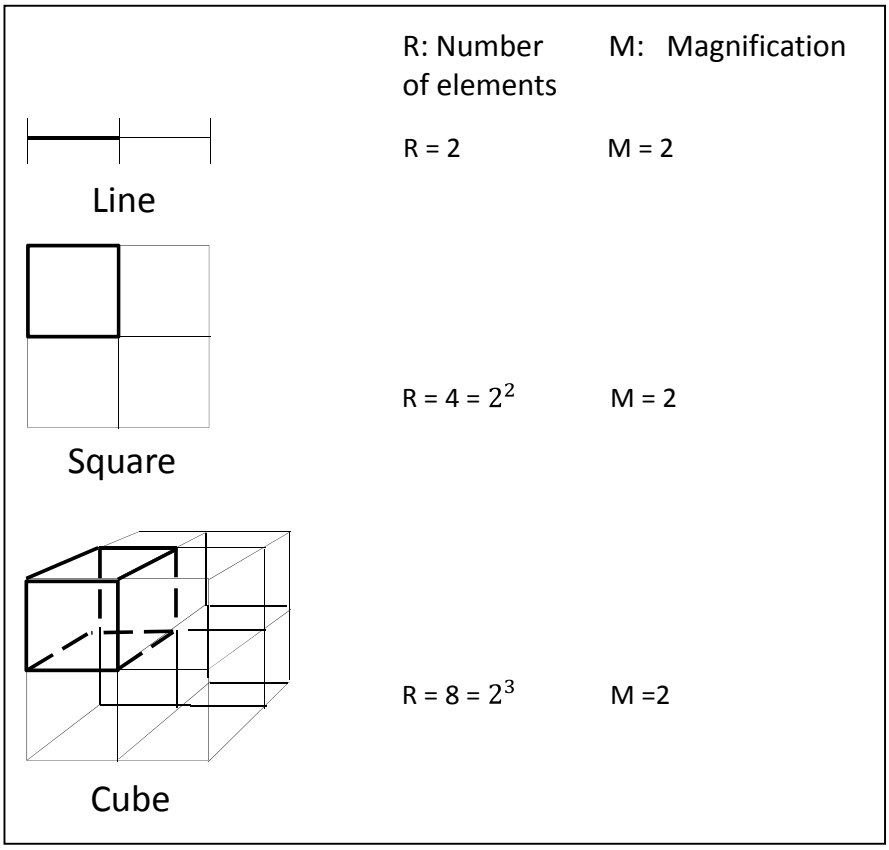

Figure 17: Euclidean dimensions

In naturally occurring fractal structures the scaling dimension is defined as follows:

$$D = \lim_{size \to 0} \frac{\log(bulk)}{\log(size)},$$

where bulk could be either a volume, or a mass, or a set of data, and size is a linear distance. In this case, D need not be an integer as is in Euclidean space (Theiler 1990).

The scaling dimension D is related to the Hurst exponent by the following formula:

$$D=2-H$$

3.2.2 The Hurst exponent (H)

The Hurst exponent is commonly applied to the analysis of fractal time series where there is no equivalence between the time axis, t, and the measured value axis, x(t). In this case the concept of self-similarity cannot be directly applied to the series, as a scaled increase in the time dimension will not be directly equivalent to the same scale increment in the measured values. In fact the rescaling of the time dimension by a factor, a, will require a rescaling of the measured values by a different factor equal to a^H in order to ensure self-similar, or statistically similar series. If this is done then the following scaling function, which describes a self-affine series, becomes applicable:

$$x(t)= a^H x(t)$$

where H describes the type of self-affinity and is known as the Hurst exponent (Kantelhardt, 2008).

The Hurst exponent is a measure of the irregularity, or roughness, of a series and it takes on typical values of between 0 and 1. The H value of between 0 and .5 indicates a rough and irregular series with none or little attenuation, while an H value of between .5 and 1 is indicative of a smooth series with good attenuation characteristics. For example, if the H value is .5, this indicates that a scale of 2 must increase the measured value axis if the time axis is to be increased by a scale of 4 (Kantelhardt, 2008).

The Hurst exponent is most directly applicable to a series with a monofractal structure where a whole series has only one fractal structure, and it is a measure of a global characteristic in the case of the more typical multifractal series where the fractal structure of the series varies point wise along the series (Makowiec et al. 2009).

The Hurst exponent, H, can be related to the Hausdorff, or Fractal Dimension D by the simple equation:

$$D=(n+1)-H,$$

where n is the Euclidean Dimension (n = 1, 2 or 3) of the measured space, whether it be a line, an area or a cube, respectively (McSharry, 2007).

3.2.2.1 Holder exponent (h)

The Holder exponent (h) of a function f(t) can be defined as the largest exponent such that there exists a polynomial $P_n(t)$ of order n, which satisfies:

$$|f(t)- P_n(t-t_0)|= O|t-t_0|^h$$

for t in the neighbourhood of t_0 (Shimizu et al. 2004).

The variance between the functions, $|f(t)- P_n(t-t_0)|$, represents the magnitude of the singularity and is proportional to 1/h, therefore $h_{(n)} \propto {}^{1}/_{\text{variance}\ (n)}$

This relationship is illustrated in Figure 18.

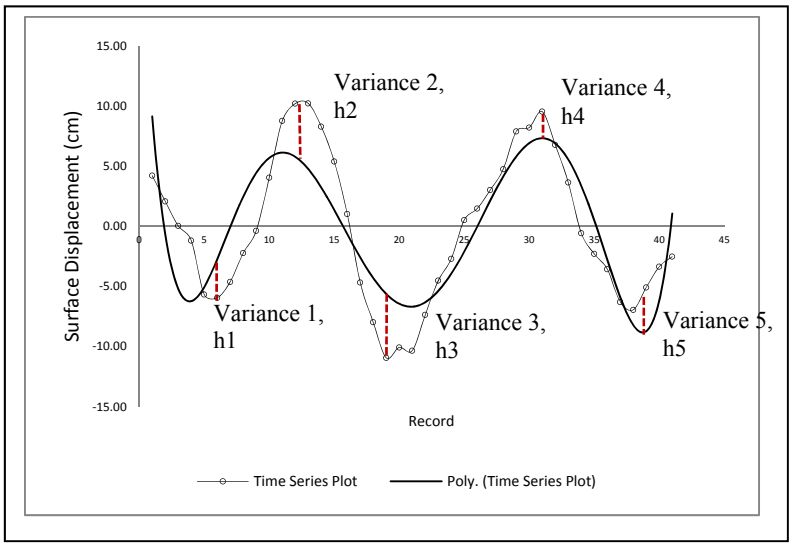

Figure 18: Illustration of Holder exponent values for a typical time series.

The Holder exponent can be considered to be a measure of the degree of a singularity at t_0 and the high values of $h_{t0} > 1$ that indicate a well-behaved smooth series where adjoining values of f(t) are similar to $f(t_o)$. However, if $h_{t0} < 1$ then the adjoining values of f(t) will vary widely. The series f(t) can be broken down into a set of h_t values equal to $\{h_t : t > 0\}$ (Makowiec et al. 2009).

The Holder exponent (h_t) is effectively equal to the local Hurst exponent and the most frequently occurring value of h_t for a function f(t) is equal to the global Hurst exponent value for the full series.

3.2.3 Hausdorff Dimension

Mandelbrot (1983) defined a fractal set as one where the Hausdorff Dimension, D, is defined as the logarithmic ratio of the number, N, of an objects internal homotheties to the reciprocal of the scale of the measurement, s (Lopes et al. 2009).

$$D = \frac{\log N}{\log \frac{1}{s}}$$

A homothety can broadly be defined as a scaled linear transformation.

3.3 The fractal structure of ocean wave systems

Conceptually the world's ocean wave system can be considered to be a fractal system comprised of characteristic wave types ranging from tides at the largest scale, to capillary waves at the smallest scale. Such a system has been shown diagrammatically in Figure 19.

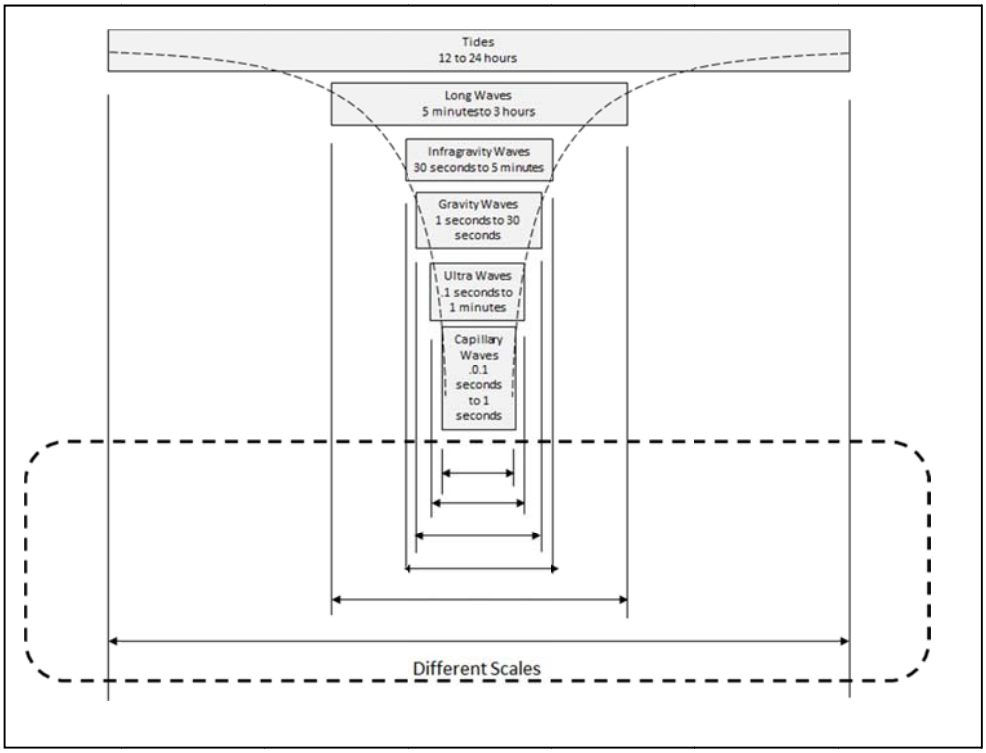

Figure 19: Diagrammatic representation of ocean wave fractal system

The concept of self-similarity in a wind-wave system is not new and the required conditions for a fractal structure can be achieved in the case of ocean waves if there is a significant difference between the length scales of the different waves being analysed (Longuet-Higgins, 1994).

Various power-law spectra suggesting dynamic self-similarity have been suggested for the description of fractal systems since Phillips re-examined the processes of energy input from wind stress (Liu. 1988).

In 1988 Stiassnie published a paper in which he developed a purely mathematical model for the derivation of a fractal dimension for the free-surface elevation of the ocean. In his research, he linked the Zakharov equation for the evolution of Fourier components in a shoaling wave field with the Hasselmann energy transfer equations for nonlinear shoaling waves, and Pierson's linear model as well as the Weierstrasse-Mandelbrot function. In this way he found that there was a possibility that the free surface of the ocean could become a fractal system with a fractal dimension, D, of between 2 and 3. Further, he also proposed that this dimension could be reduced to

4/3 when waves from one direction had the same amplitude as waves from the directly opposite direction (Stiassnie, 1991).

In 2002 Ajiwibowo determined that the fractal dimension, D, of ocean wave profiles in Grays Harbour, Washington and at Sandy Duck in North Carolina was in the range of $1.5 < D < 1.8$.

The multifractal properties of significant wave height time series data, recorded in the open ocean at 24 sites off the west coast of the United States of America, have been investigated (Ozger, 2011). A wavelet based approach was used in the investigations and it was found that the peak Holder exponent values of the singularity spectra at the different sites were all less than .5. This indicates that the recorded significant wave heights were generally anti-persistent, with short correlation periods. Slightly higher exponent values, closer to .5, were recorded in the deeper water locations further offshore and this was found to be indicative of the fact that the series at these sites had more persistent trends.

The early work on the study of statistical scaling laws began with Bachelier and his work, followed in by Kolmogorov (1941), Mandelbrot (1963) and Frisch (1995), (Lopes and Betrouni, 2009).

As mentioned above, fractal and multifractal scaling laws have been found to be applicable to the analysis of both sea surface and water wave characteristics for some time now. In addition, scaling laws have also been found to have applications in the following fields of research (Kantelhardt, 2008):

- **Physics**, including surface roughness and the chaotic spectra of atoms
- **Geophysics**, including water runoff, wind speed and seismic events
- **Astrophysics**, including X-ray light sources and sunspot numbers
- **Engineering**, including highway traffic and nuclear power generation
- **Medicine and Physiology**, including heartbeat, blood pressure, nerve spike intervals and others, and
- **Economics**, including market trends and share transactions. (Kantelhardt, 2008)

The geometric features of a time series, such as wave groups in a time series of sea surface displacements, are visually apparent in the series, but are unable to be

accurately described or analysed by the more common techniques used for the analysis of time series.

Fractals can be considered to be geometric descriptors of the shape of scale invariant features (Billiones et at. 1999). As such, fractals are good descriptors of sea surface displacement time series which appear to represent chaotic, noisy systems but which contain irregularly recurring features such as wave groups.

Fractals as well as other shape descriptors, such as roundness and elongation, are independent of size and therefore the conventional Euclidean dimensions of maximum wave height (Hmax), significant wave height (Hm0) and peak frequency f(p), which are conventionally used to describe the sea surface. They are rather based on the frequency of occurrence of features such as singularities in a time series.

Notwithstanding the fact that fractal mathematics and fractal analysis techniques have been used fairly widely in the fields of ocean engineering, they do not seem to have been used in the field of coastal engineering for the analysis of bound infragravity wave sea states.

3.4 Methods of fractal analysis

3.4.1 Overview of fractal physics

If the small part of a large object is surrounded with a sphere of radius r, the number of components Σ, in the sphere increases as the radius of the sphere increases. The measure of Σ is not important as long as it is a function of the radius of the sphere (Lopes et al. 2009). If one could identify a relationship between the radii r_i of the spheres and the number of components Σ_i in the different sized spheres for a type of object, then one could describe the object in terms of this relationship. Further, one could then also compare it to another object with a different relationship between r_i and Σ_i.

This concept is illustrated in figure 20 for a set of circles with radii equal to

$$r_1 = 2, r_2 = 4, r_3 = 8 \text{ and } r_4 = 16, \text{ and}$$

a number of respectively surrounded squares equal to

$$\Sigma_1 = 12, \Sigma_2 = 44, \Sigma_3 = 180 \text{ and } \Sigma_4 = 772$$

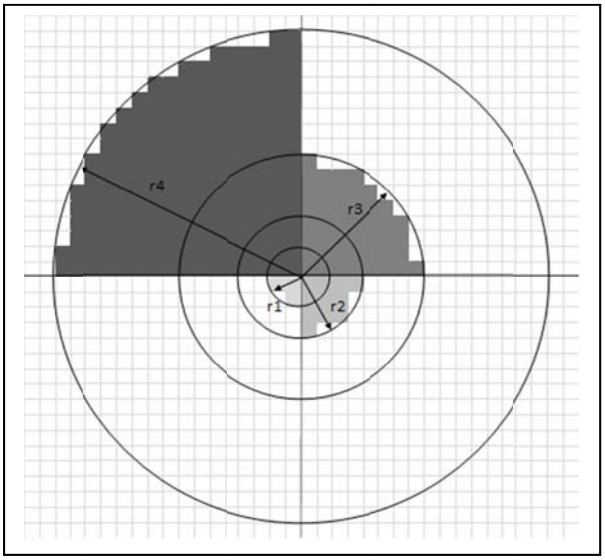

Figure 20: Sequential circles encapsulating numbers of squares

The radii of the circles and the number of encapsulated squares have been shown together with their respective log2[5] values in Table 11.

[5] Log2 = log to the base of 2

Table 11: Radii of circles and number of encapsulated squares

Radius of Circles		**Number of Squares encapsulated**	
(Arbitrary length)	Log2 Radii	(Σ)	Log2 (Σ)
2	1	12	3.584963
4	2	44	5.459432
8	3	180	7.491853
16	4	772	9.592457

A log-log plot of the radii and Σ values has been given in Figure 21 and the slope of the plot, which is equal to $D = {}^{\log2(\Sigma)}/_{\log2(\text{radius})}$, is 2. This dimension is the Euclidean dimension for a surface area as discussed in section 3.2.1.

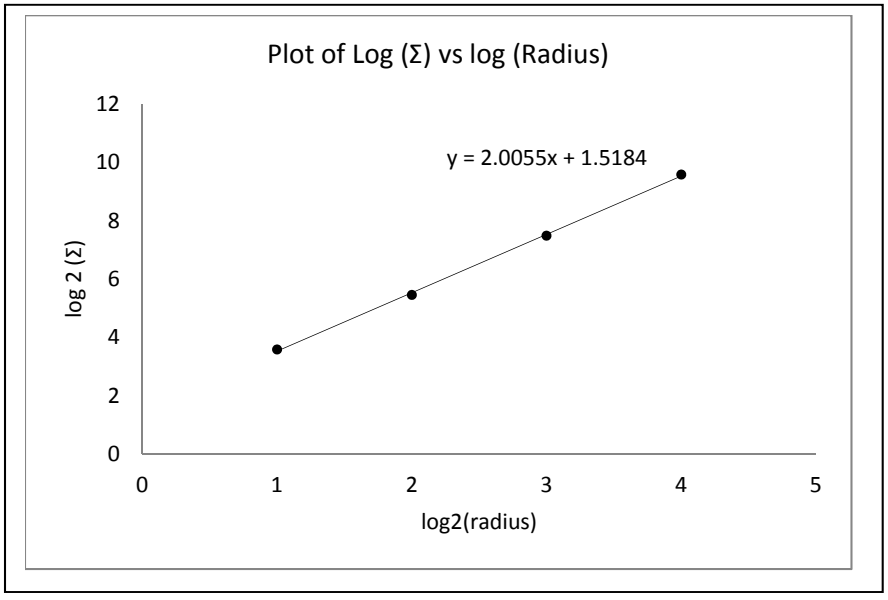

Figure 21: Log-log plot radii and of **Σ** values

The fundamental characteristic of a fractal object is that its description is a function of the scale of measurement.

Mandelbrot described the coastline as a typical fractal object because its 'length' depends on the scale (or ratio of the length of the object, L_o to the length of measure, l_m) (Mandelbrot, 1977). As the spatial resolution, L_o/l_m, of the coastline increases, so does the length of the coastline because there is more detail that can be measured at the increased spatial resolution. In this way the single Euclidean value of length, becomes a fractal set (Lopes and Betrouni, 2009).

Mathematical fractals can be exactly defined in terms Euclidean dimensions including statistics. However, naturally occurring fractals, which can be said to be statistically self-similar, can only be fully defined in terms of both a statistical similarity and a power law function relating the scale of observation (Eke et al. 2012).

Time series that are mathematically analysed are generally assumed to be comprised of continuous sequences of differentiable data. On this basis, a very close similarity to the time series can be derived by a Fourier analysis, and a short length of the series, close to any value, say t_i, can be approximated by the following Taylor polynomial, or power, series:

$$P(t) = f(t_0) + \frac{f'(t_0)}{1!}(t-t_i)^1 + \frac{f''(t_0)}{2!}(t-t_i)^2 + \frac{f'''(t_0)}{3!}(t-t_i)^3 + \ldots\ldots\ldots \frac{f^n(t_0)}{n!}(t-t_i)^n$$

In real life, vertical sea displacement time series are generally found to be 'noisy' functions that are almost impossible to fully describe by either a Fourier or Taylor Series. In addition, these time series can include features such as wave groups, which can occur irregularly throughout the series. In these cases, the series can be comprised of a number of irregular varying increments in sequential data and this makes it very difficult to approximate with a well-behaved function such as a polynomial. The difference between a measured time series and the closest fitting polynomial is generally defined to be a local singularity, as shown in Figure 18.

A time series with local singularities can be described mathematically as follows:

$$P(t) = f(t_0) + \frac{f'(t_0)}{1!}(t-t_i)^1 + \frac{f''(t_0)}{2!}(t-t_i)^2 + \frac{f'''(t_0)}{3!}(t-t_i)^3 + \ldots\ldots\ldots \frac{f^n(t_0)}{n!}(t-t_i)^n + \frac{f^h(t_0)}{h!}(t-t_i)^{h_i}$$

where h_i is a non-integer number representing a local singularity of the function at $t = t_i$.

The abovementioned features and singularities in a time series could be scale invariant with either monofractal or multifractal characteristics (Ihlen, 2012).

Monofractal scale invariant time series, $f(ct)$, with either only one, or else a very dominant singularity can be written mathematically as:

$$f(ct) = c^H f(t),$$

where C is a constant and H is a global power law exponent, known as the Hurst exponent (Ihlen, 2012). The Hurst exponent can be considered to describe the general roughness or irregularity of a time series as defined by its deviations from a well-behaved, smooth polynomial function.

A multifractal series with a number of different singularities can be considered to contain a range of degrees of roughness and this type of series can best be represented by a Multifractal (or Singularity) Spectrum.

The Hurst exponent is named after the British hydrologist, H E Hurst who first identified it during his work in connection the measuring the long-term storage capacity of reservoirs. The Hurst exponent has become a commonly used index for the fractal description of both non-correlated or correlated fractional Gaussian noise (fGn), as well as non-diffused and diffused fractional Brownian motion (fBm) (Delignieres, 2011). This continuum is shown diagrammatically in Figure 22.

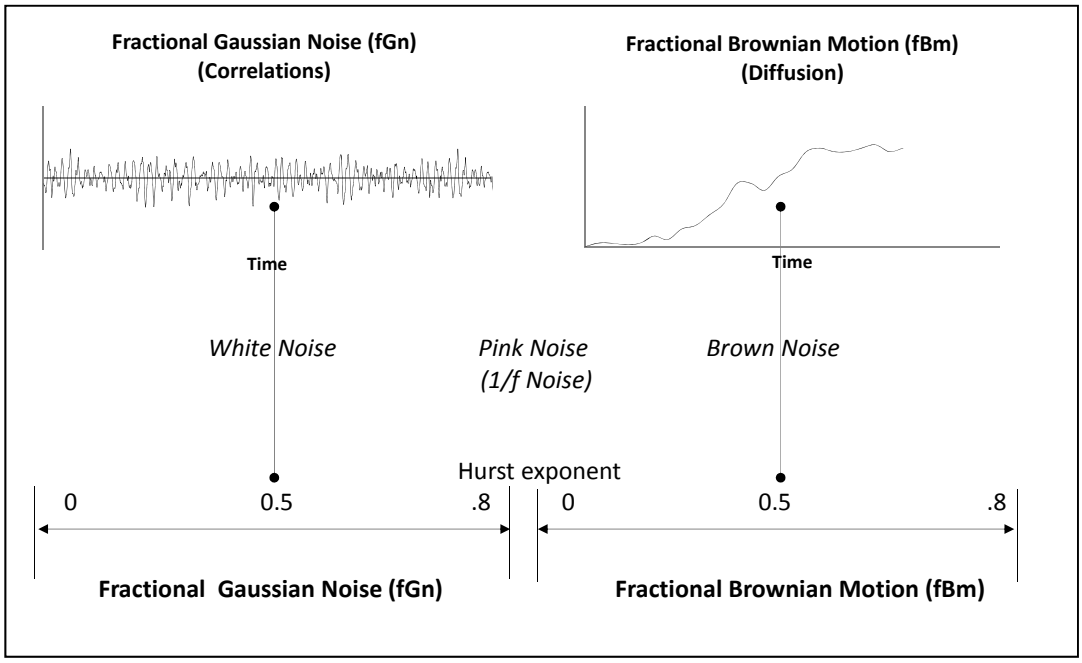

(Ref: Sourced from Delignieres et al, (2011)

Figure 22: Fractal time series continuum

The Hurst exponent can be related to the generally used fractal dimension, D, by the formula:

$$D = (n+1) - H,$$

where n is the Euclidean dimension of the object being measured (n = 1 for a self-affine line which is 1 Dimensional).

Fractional Gaussian noise series are generally stationary with a broad range of correlation characteristics, whereas fractal Brownian motion series are non-stationery with a broad range of diffusion characteristics. These two types of series are very different and yet they are linked in that the increments in the fBm series (obtained by subtracting each value of the time series from its predecessor) formed by the fGn series. Conversely, a cumulatively summed fGn series forms the fBm series (D Delignieres et al, 2006).

In the case of the fGn series the value of H indicates the global degree of correlation of the complete series, while in the latter case it indicates the global degree of correlation of the steps in the series.

The different characteristics of time series that can be identified by the Hurst exponent have been summarised in Table 12 (Delignieres, 2006).

Table 12: Time series characteristics identified by Hurst exponent values

Hurst Value	Type of Series	Time Series Characteristic
$0 < \mathbf{H} < .5$	fGn fBm	The series will be uncorrelated with increases in the series probably being followed by decreases, The series will be non-persistent and increases in the increments probably be followed by decreases in the increments
$\mathbf{H} = .5$	fGn and fBm	The series will not contain significant long-term statistical correlations.
$.5 < \mathbf{H} < 1$	fGn fBm	The series will be correlated. The series will be persistent

Non-correlated and non-persistent series, as well as correlated and persistent series contain characteristics that segregate them from purely random series.

The Hurst exponent is a good single parameter for the representation of an average fractal characteristic of a complete time series, but it is not applicable for the analysis of local singularities and intensity fluctuations in complex multifractal series. In these cases another exponent, known as the Holder exponent, $h(t)$ is used. A multifractal series can best be defined by a whole set of Holder exponents (Shimizu et al. 2004) as follows:

> Multifractal mathematics assumes that different degrees of singularity are grouped in fractal sets, K_h bound into a larger system. In this way a multifractal series can be described by the number and size of these sets, as

determined by the Hausdorff dimension D(h) that is a function of the Holder exponent (h).

The core objective in the classification of local singularities in a fractal series is the determination of the magnitude, or percentage of the series occupied, by the singularity (Shimizu et al. 2004).

A typical multifractal time series of a natural phenomenon will generally be comprised of a range of Holder exponent values representing different degrees of roughness. In 1919, the Hausdorff dimension, D_h was defined to be a measure of distribution of the set of Holder exponents in a given time series. The values of D_h are considered to represent the strengths, or frequency of occurrence of the respective Holder exponents, and the singularity spectrum can be considered to represent the probability density function of local Holder exponents (Khan and Fadzil, 2007).

An example of a typical Singularity Spectrum has been shown in Figure 23.

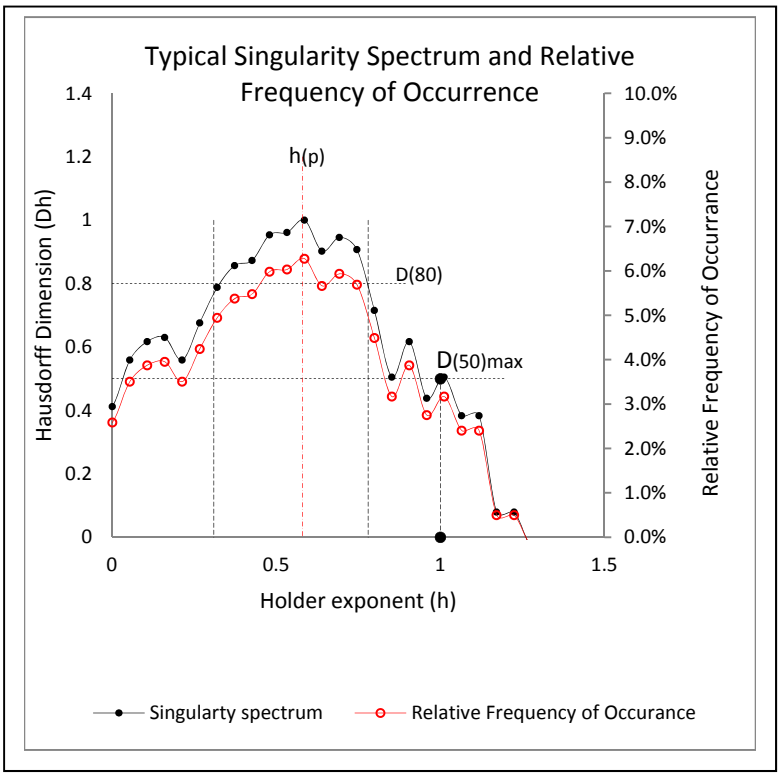

Figure 23: Typical singularity spectrum

The most frequently occurring Holder exponent, h(p), with a Hausdorff dimension = 1, is equal to the global Hurst exponent for a series. Values of h with $0 < h < .5$ represent degrees of roughness or non-correlation in a series, and values of h with $.5 > h > 1$ represent degrees of smoothness or correlation, which are most prevalent in a series.

Singularity spectra are normally characterised and compared on the basis of their overall widths at the base of the spectra, and the width of the spectrum the point where the Hausdorff dimension is .8, (D80 per cent). The former width indicates the degree of overall fractal complexity in the series, and the latter width indicates the degree of fractal complexity in the core of the series. Another indicator, which has been used in this research to indicate the maximum degree of smoothness with a 50 per cent relative frequency of occurrence, is the maximum Holder exponent with a Hausdorff dimension of .5, D(50).

The cumulative frequency function of the Singularity Spectrum comprises the probability of non-exceedance function for the series. This function indicates the percentage probability that any selected exponent value in a series will not be exceeded. The probability of exceedance is equal to 1 – (probability of non-exceedance).

The Probability of non-exceedance curve for the singularity spectrum in Figure 23 is shown in Figure 24.

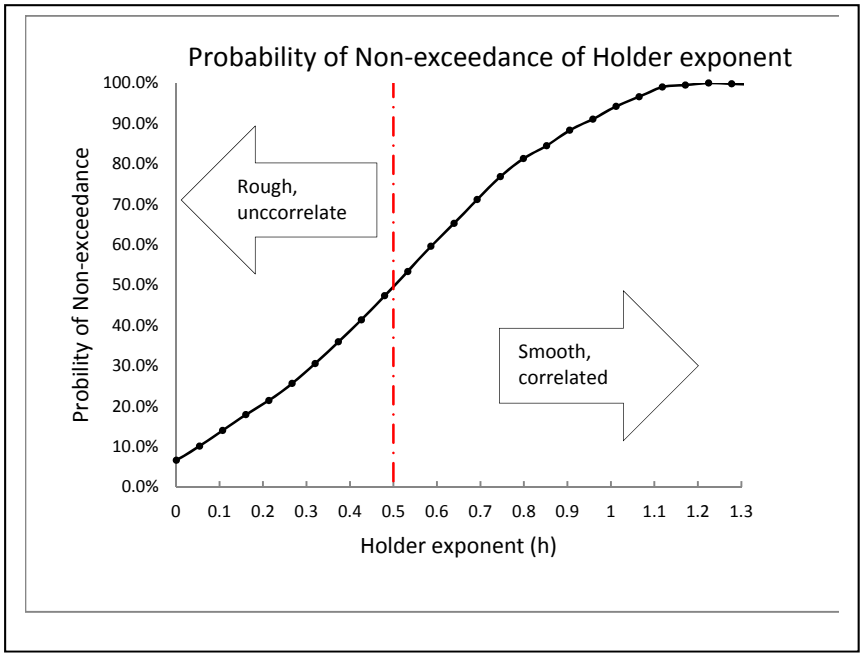

Figure 24: Cumulative frequency / probability on non-exceedance

3.5 Measurement of fractals

In the early stages of time series analysis, attention was focused on descriptive statistics such as the mean value of the data. Variability within a series of data or laboratory results was not considered to be important and the effects of variability were removed from analysis by means of averaging over a number of sequences, or trial results, as the case may be. In the case of a time series, variability effects were removed by filtering (Diniz et al. 2011).

More recently, in the last 30 years, interest in the analysis of dependencies in a time series has become an important topic in research and, in this regard, special attention has been given to short- and long-term dependencies. A short-term dependency is considered to apply when the current value of data can be considered to be dependent only on its previous value, or on a few previous values, in a series. On the other hand, long-term dependencies occur when correlations in a series occur over a number of time scales, over a long period of time. Series with this characteristic are referred to as '1/f noise' (Rangarajan and Ding, 2001, Diniz et al. 2011).

The following methods in the time and frequency domains can be used for the determination of the Fractal Indices and the Fractal Dimension of a time series:

- Time domain Methods include:
    - The Rescaled Range (R/S) analysis method, and
    - The Multifractal Detrended Fluctuation Analysis (MDFA) method.
- Frequency Domain methods include:
    - The Power Spectral Density (PSD) analysis method in the Fourier Domain
    - The (PSD) analysis method in the Wavelet Domain, and
    - The Wavelet Transform Modulus Maxima (WTMM) method in the frequency domain.

The first of the methods in each domain is usually applied to the fractal analysis of single, stationary series (Kantelhardt, 2008), and it is not uncommon to use either of them for the initial analysis of a fractal time series. However, it has been found that the PSD method in the Fourier domain is open to producing the incorrect results

(Rangarajan and Ding, 2001) as it is based on linear theory and the assumption that the series being analysed is stationary.

The R/S method is based on the determination of the Hurst exponent from averaged, normalised, scaled subdivisions of a series, and the PSD methods are based on the derivation of the spectral exponent, β, by the means of a Fourier and a Wavelet Analysis of the series.

The last two methods in each domain are based on multifractal analysis methods.

The short-term irregularity (persistence) of a Gaussian noise (Brownian motion) time series can often be used to identify whether a particular series is either monofractal or multifractal, and this determines the most applicable model to be used for the fractal analysis of the series (Marmelat et al, 2012). However, this methodology can be difficult to implement if the series to be analysed is bounded within finite limits, as shown in Figure 25.

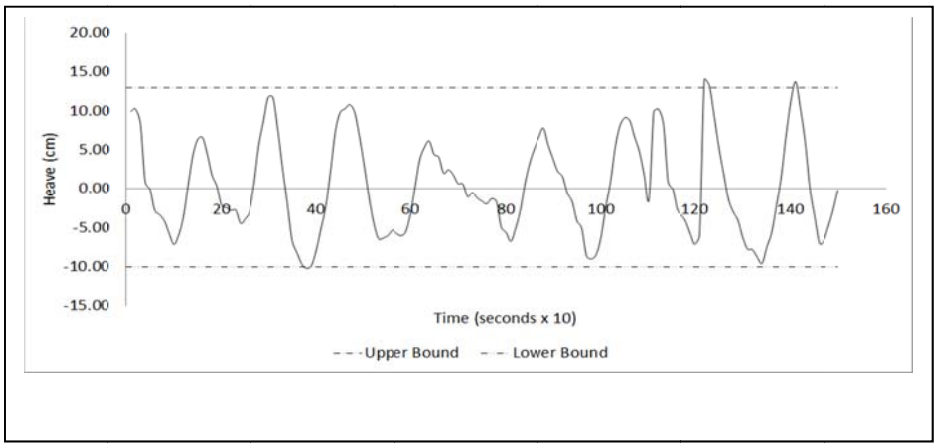

Figure 25: Typical bounded time series

A Brownian motion (fBm) series is generally not limited and fluctuations increase exponentially with time. However, a bounded series cannot exceed functional limits imposed on the series by external factors, such as physical constraints (Marmelat et al, 2012). In this case a series could display short term, persistent fBm characteristics with long-term anti-persistence motions (Delignieres et al, 2011). This is clearly the

case for sea surface displacements where maximum surface displacements are limited by gravity.

3.5.1 Rescaled Range method

Ranges from maximum to minimum values in a typical time series will vary from segment to segment of the series, as shown in Figure 26.

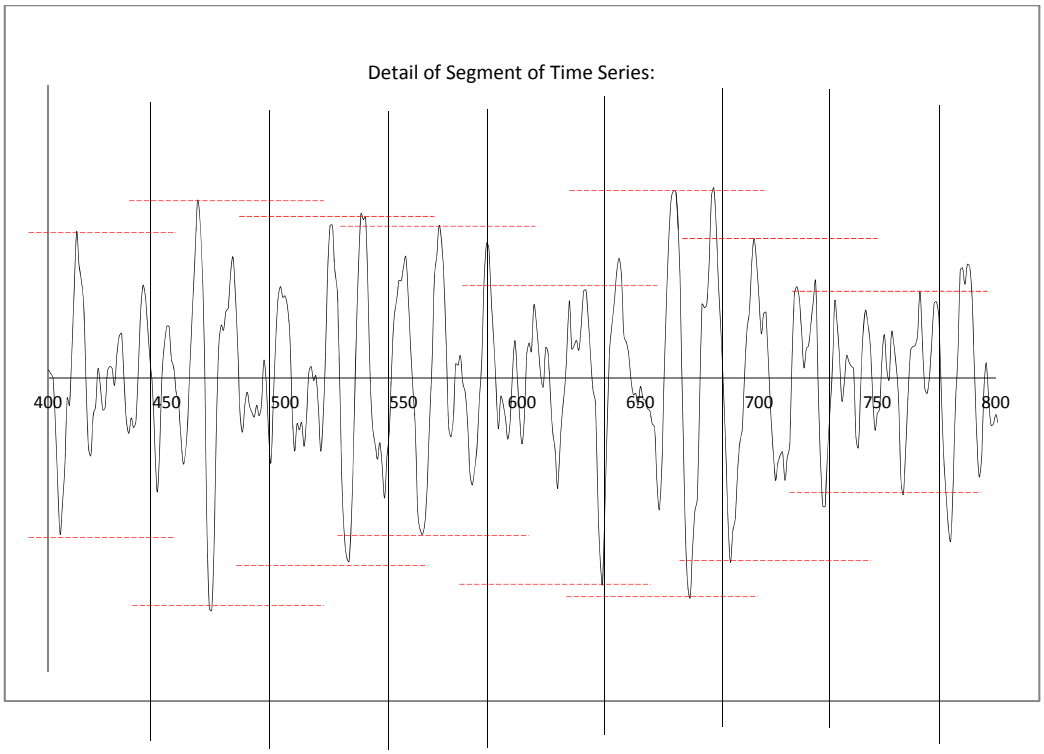

Figure 26: Variations in range for segments of a typical time series

The Hurst exponent of such a series can be determined by the rescaled range, R/S, method of analysis which is based on the assumption that the ranges for different scales of a fractal series follow a scaling law (Kristoufek, 2010).

A series with length L is divided up into a number N of adjacent subsegments with length, v, such that Nv=L. Each subsegment can be labelled I_n with n = 1,2,3.....N, and each element of the subsegment labelled $r_{k.n}$ with k=1,2,3……."v". The breakdown of the series in accordance with this system is shown diagrammatically in Figure 27.

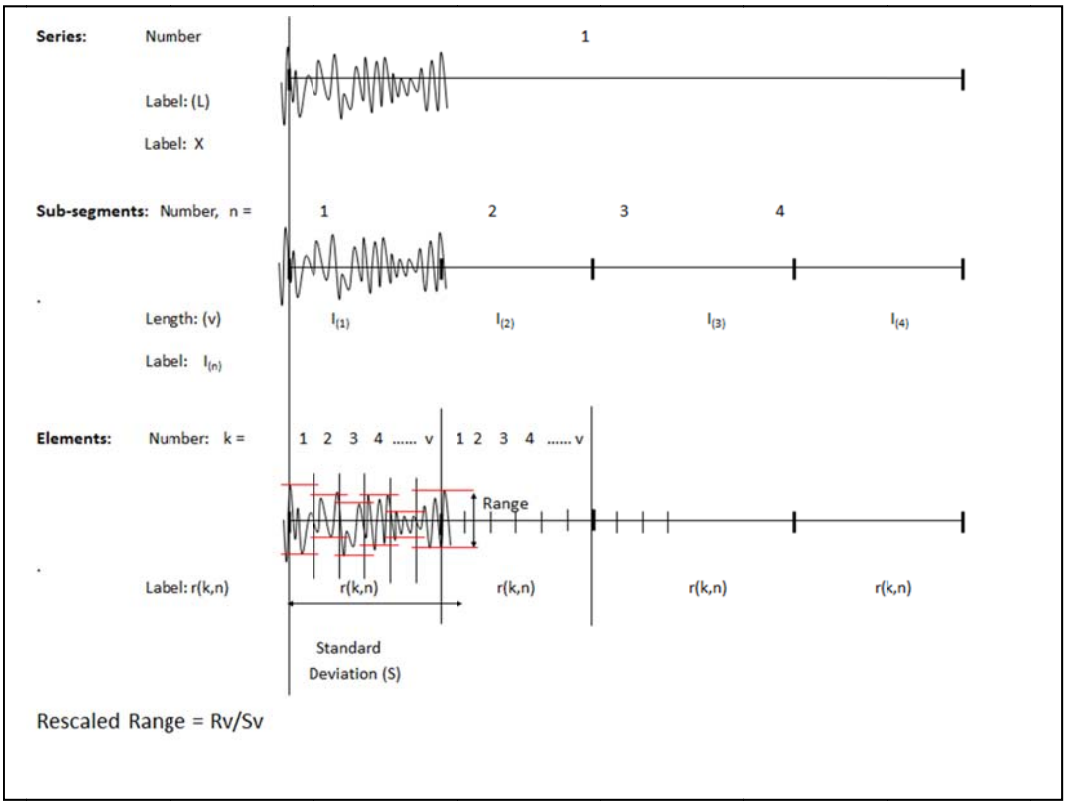

Figure 27: Breakdown of time series into subsegments and elements

The average value of the range R_{In} in each subsegment is calculated and normalised by the standard deviation S_{In} of the segment to form a rescaled range:

$$(R/S)_{In} = \frac{R_{In}}{S_{In}}$$

The above process is repeated for each sub-element length of v to determine average rescaled range values $(R/S)_v$

The length v is increased and the whole process is repeated before calculating the rescaled range value for the series:

$$(R/S)_v = C\, v^H$$

where C is a constant independent of v

Taking log values on each side of the equation:

$$\log_b (R/S)_v = \log_b C + H \log_b v$$

where H is the Hurst exponent.

$$H= \log_b(R/S)_v / \log_b v$$

The value of H can be determined from the slope of the log-log plot of $(R/S)_v$ and v.

3.5.2 Multifractal Detrended Fluctuation Analysis (MDFA) method

The MDFA method has been developed for the fractal analysis of a non-stationary series where the statistical properties of the series vary throughout the series (Kantelhardt et al. 2002). Multifractal Analysis methods address the inherent nonlinearity in a series in a direct way, rather than as variations on linear systems (Stanley et al. 1999).

The MDFA method of analysis is based on the evaluation of the different scaling behaviours of local fluctuations in a time series. To this end, the time series function to be analysed is broken down into non-overlapping segments for the determining their different profiles, trends and scaling functions (Kantelhardt, 2002).

Multifractal time series can be characterised by the degree of correlation (persistence) over both short and long terms. A series could have high short-term correlations, with long-term non-correlations, or it can have high long-term correlations, with non-correlations over the short term (Kantelhardt et al. 2002).

Complicated fractal series are made up of subsets with varying scaling behaviours, and are best represented by a Singularity Spectrum for a given series.

3.5.3 The Fourier power spectra density (PSD) method of analysis

Correlations, or persistence, in a time series can be measured in the spectral domain in terms of an inverse power law function incorporating a spectral scaling exponent β.

The aforementioned function and exponent are determined from an analysis of the rate of decay of the power law function S(f) in a PSD plot where the power in a series S(f) is related to frequency f by an inverse power law function with the exponent β as follows:

$$S(f) \sim {}^{1}/_{f^{\beta}} = f^{-\beta}$$

The scaling exponents of fGn and fBm process are related to the Hurst exponent by the following functions (Rangarajan and Ding, 2001):

$H=(\beta+1)/2$ for a fGn process, and

$H=(\beta-1)/2$ for a fBm process.

Correlations, or persistence, in the fGn and fBm time series generally have the following β values:

fGn process: $-1 < \beta < 1$, corresponding to Hurst exponent values of $0 < H < 1$, and fBm process: $1 < \beta < 3$, corresponding to Hurst exponent values of $0 < H < 1$.

A log-log plot of the power series of a bounded time series presents a negative slope in the high frequency range indicating short term persistent trends or correlations (Marmelat et al, 2012; Delignieres et al, 2011).

Sea surface displacement time series generally have steep negative slopes, with $\beta = 2$ to 3, in the high frequency range. This characteristic can clearly be seen in the power spectral density plots of two typical time series in Figure 28. These values are indicative of fBm, with persistence in the short term. The equivalent values of the Hurst exponent would be $.5 < H < 1$,

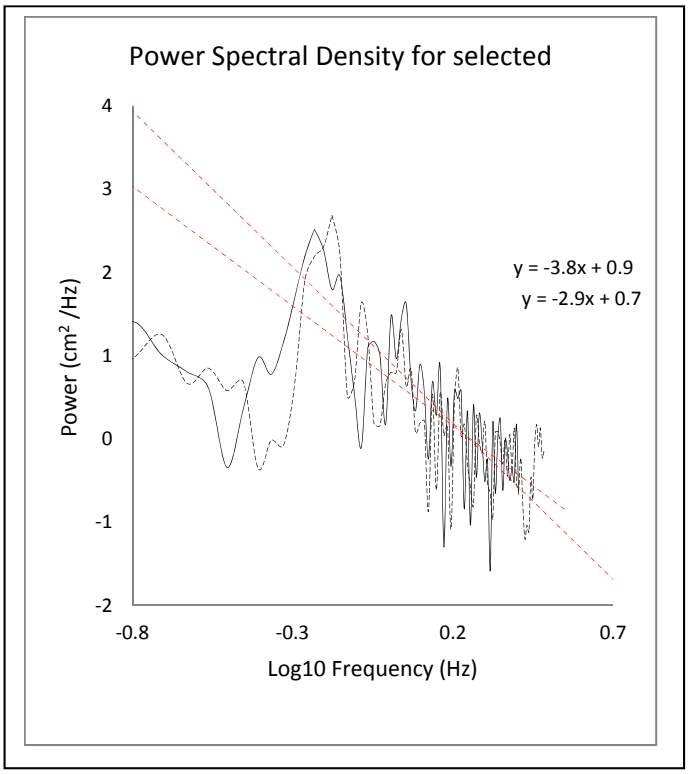

Figure 28: Plot of β values for long term short-term correlation

3.5.4 Wavelet transform methods

The wavelet transform is a convolution of a time series, f(t), with a short wavelet 'mother' wavelet. Wavelets are defined by the formula $\psi(t)_{(s.b)}$ where s and b define the dilation and translation of the wavelet $\psi(t)$.

The general form of a wavelet can be defied as $\psi(t)_{(s.b)} = \frac{1}{\sqrt{s}} \psi(t) (\frac{t-b}{s})$ where s > 1, and b ∈ (set of real numbers).

In terms of the above the mother wavelet is the general form with s = 1and b = 0.

A number of standard, or mother wavelets, have been developed and are used in continuous wavelet transform analysis. These standard forms include the following more common ones:

- The Morlet wavelet,
- The Mexican Hat wavelet

- The Shannon wavelet

The mother wavelet that has been used in the analysis in this research is the Morlet wavelet as defined as follows:

$$\psi(x)= e^{-t^2/2} \cos(2 \pi f t)$$

The wavelet transform of a function f(t) is represented by wavelet coefficients

$$C_{(s,b)} = < f(t); \psi(t)_{(s.b)} >$$

where $< \cdot ; \cdot >$ defines the inner, or scaler, product of the series and the wavelet transform. (Sarker et al. 2002)

A graph of the wavelet has been shown in Figure 29 and graphs of a family of dilated and translated Morlet wavelets have been shown in Figure 30. The frequency and period of the wavelets are determined on the basis of their Fourier transforms and, on this basis, the frequency of the Morlet wavelet is equal to 1/scale, and its period is equal to the scale of the wavelet.

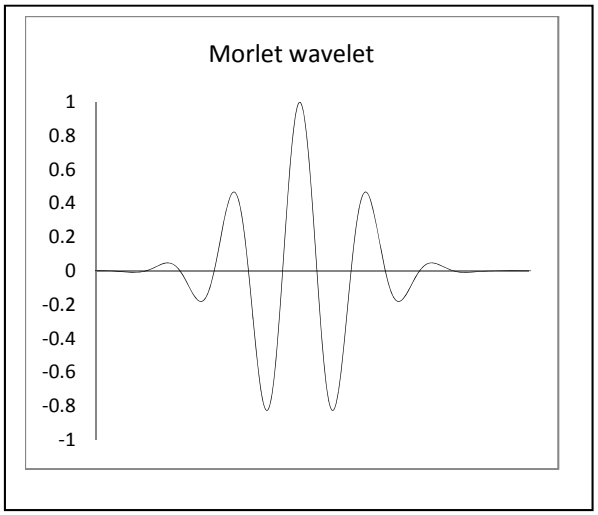

Figure 29: Graph of Morlet wavelet

The mother wavelet function can be re-written as, $\psi(x)_{s,b}$, to allow it to be moved, or translated, through different filtered levels of the series, at different scales. The scaling and translation of the mother wavelet function are achieved by the variables, s

that changes the scale or width of the wavelet, and b that changes the position of the wavelet.

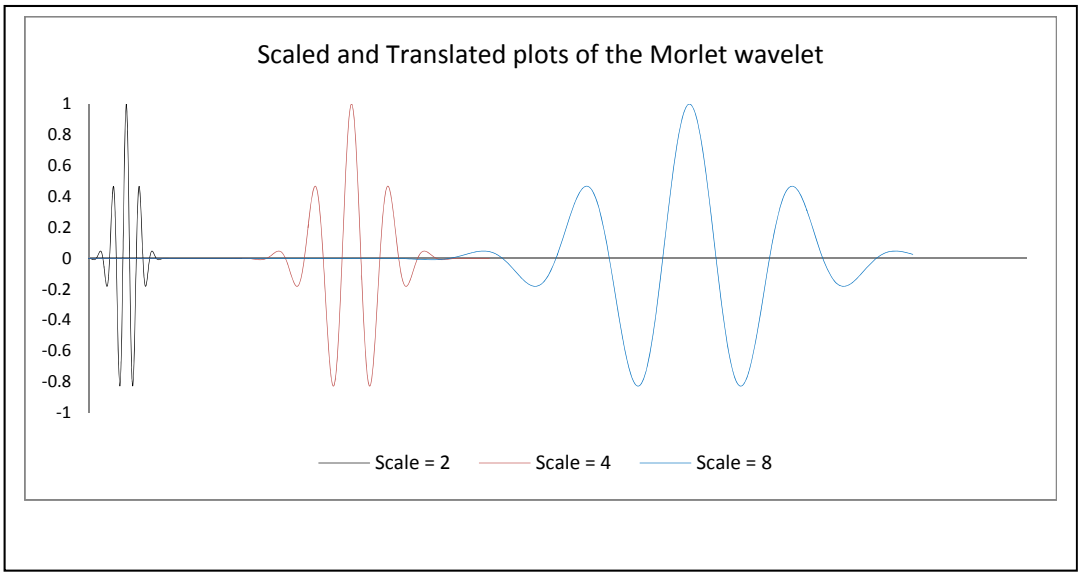

Figure 30: Graph of dilated and translated Morlet wavelets

The wavelet function is normalised at each scale so that it has unit energy.

The objective of the wavelet transform analysis is to decompose a time series into a binary tree structure of energy levels at different cascading frequencies. The scales in a typical wavelet transform structure are very often selected on the basis of their being octave, or 2^2, increments (Jones et al. 1995), as shown diagrammatically in Figure 31.

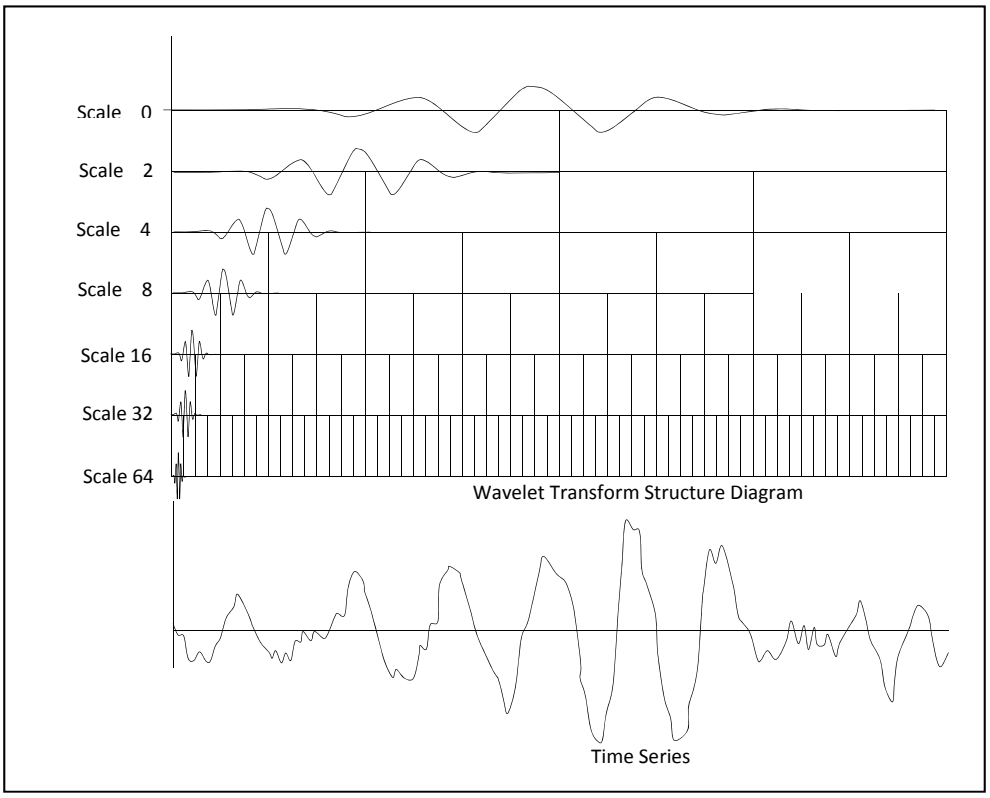

Figure 31: Diagram of a typical continuous wavelet transform structure.

Given the above, the wavelet transform can be defined as follows:

$$Wf_{(s,b)} = \frac{1}{\sqrt{s}} \int_{-\infty}^{\infty} f(x)\psi\left(\frac{x-b}{s}\right) dx$$

where $s,b \in \mathbb{R}$ and $s > 0$

The wavelet transform effectively decomposes a time series into different scales by applying a high and low pass filtering process at each scale. The high pass series at each of the scales is retained at the level of the scale, and the low pass series is filtered further at the next higher scale. This process is illustrated diagrammatically in figure 32.

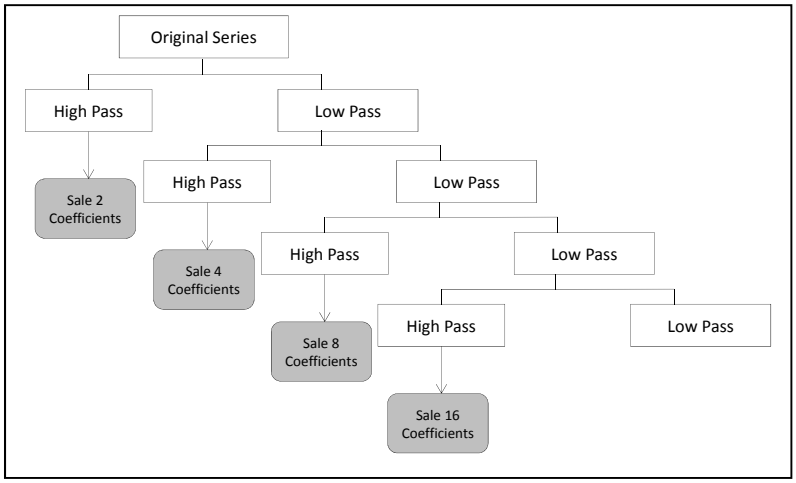

Figure 32: Diagram of wavelet filtering process

The convolution of a polynomial of degree n with a wavelet containing n vanishing moments will be zero. This characteristic of a wavelet convolution with a time series is very useful in fractal analysis because the result of the convolution is a series of the differences between the time series and the polynomial. These differences, by definition, represents the local Holder exponent and the less the difference the higher the Hurst exponent (Farrar and Wordon, 2013).

A time series of typical sea surface displacements has been shown in Figure 33 and Continuous Wavelet Transform (CWT) plots of the of the Relative Energy in the wave train have been shown in the mesh and contour plots in Figures 34 and 35 respectively to illustrate the aforementioned outputs of the transform.

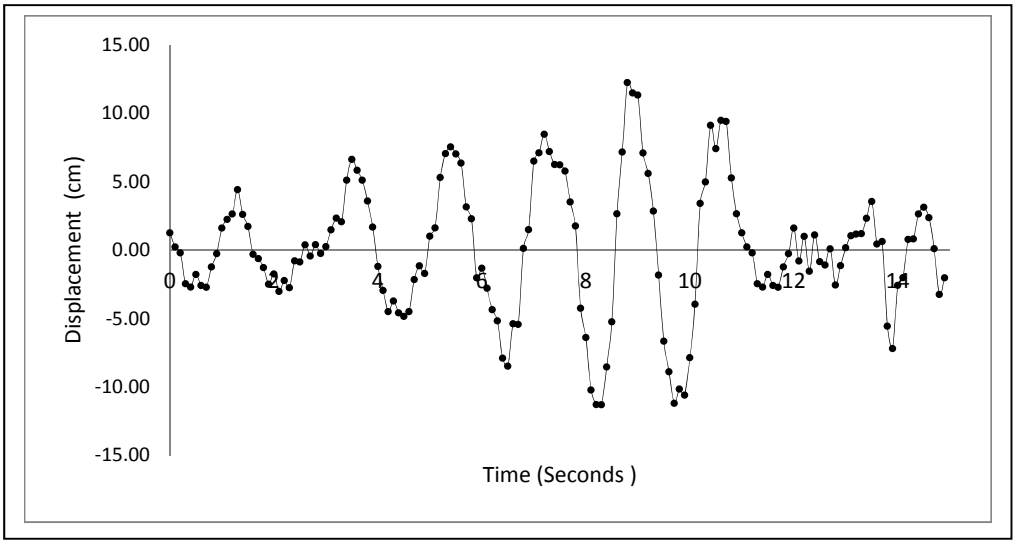

Figure 33: Time series of a typical sea surface displacement sequence.

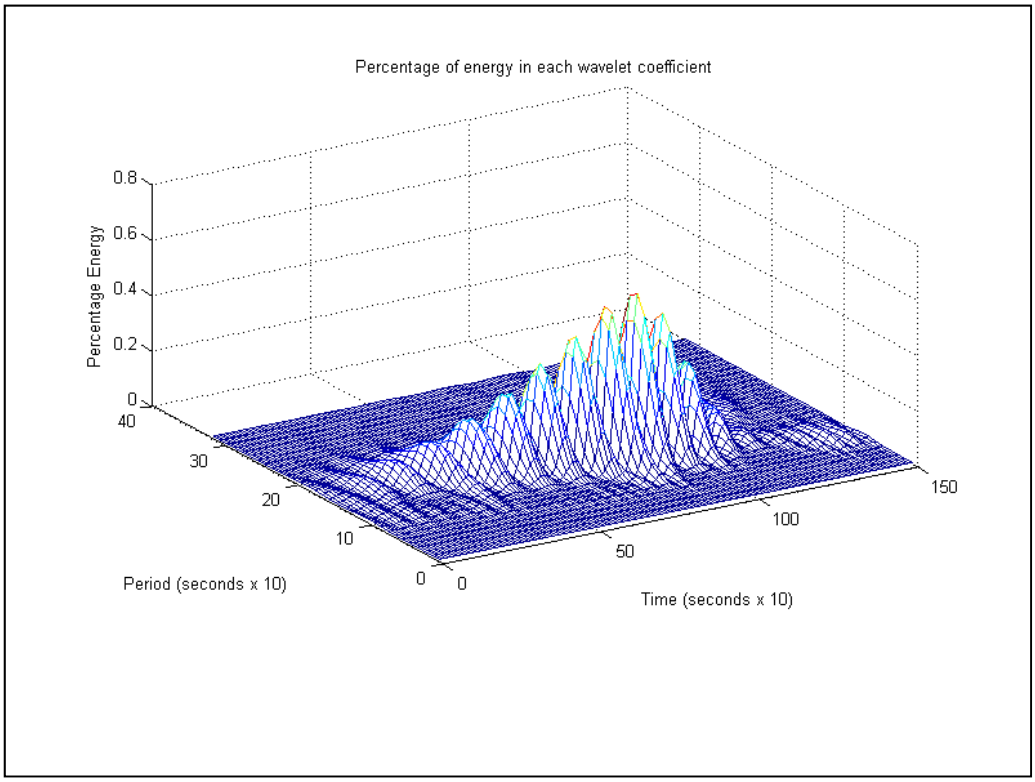

Figure 34: Mesh plot of the percentage energy in each wavelet coefficient

The mesh plot in Figure 34 clearly illustrates the benefits of CWT analysis from the point of view of being able to obtain the varying distribution of spectral energy in a series with time.

A contour plot of the percentage energy in each wavelet coefficient of the time series in Figure 33 has been shown in Figure 35.

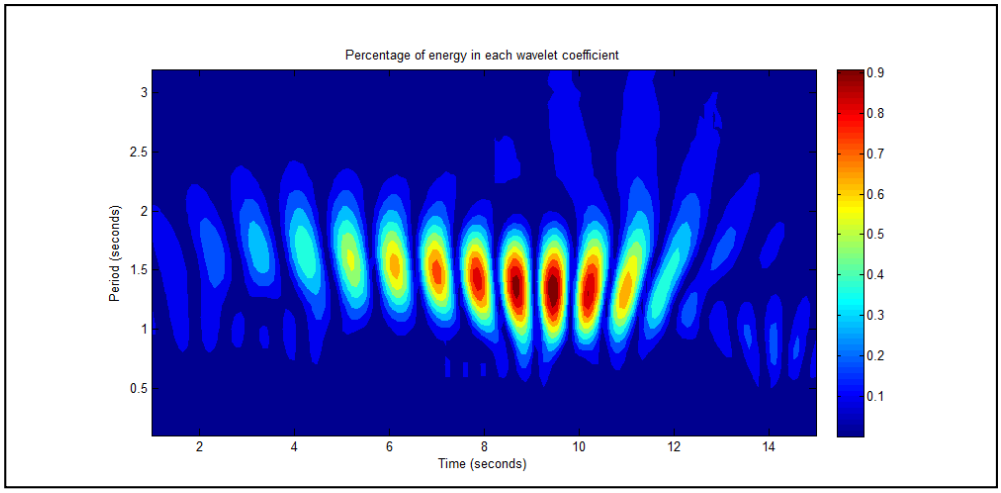

Figure 35: Contour plot of percentage energy in each wavelet coefficient

The contour plot of the CWT displays the absolute value of the energy distribution in the time series, as a function of period on the y-axis, at times along the series on the x-axis.

3.5.5 Wavelet scaling method

The scaling of time series data can be analysed in both the frequency domain by using the PSD method, as described in section 3.5.3, as well as in the time/frequency domain by means of the continuous wavelet transform method (Zaourar et al. 2013).

As has been demonstrated above a scaling characteristic of a time series can be identified by a straight-line plot at a particular slope, $-\beta$, over a range of the frequencies in the log-log plot of the power density spectrum. The same trend in a time series can be identified by means of the wavelet scaling method, where the time

series is analysed in the time/frequency domain, and any trend is identified in the log-dyadic[6] frequency plot of power spectrum derived from the transform plot.

Two typical time series have been analysed by the wavelet scaling method and the PSD functions in the wavelet domain have been shown together with the average $^{1}/_{\beta}$ slope in Figure 36.

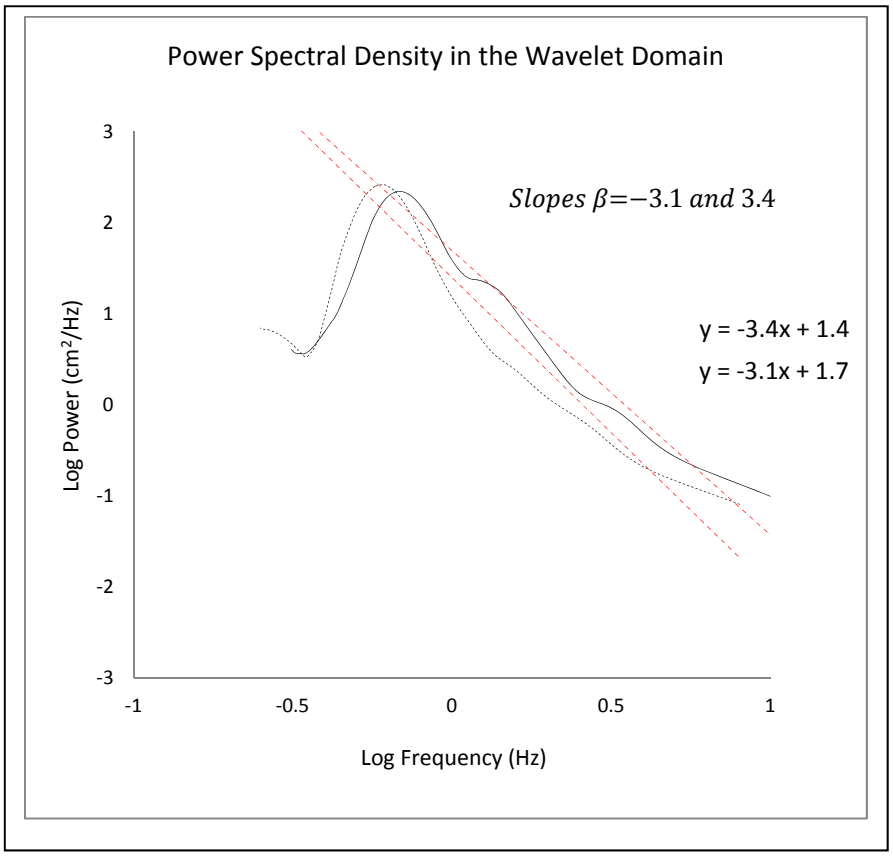

Figure 36: Typical power spectral density plots in the wavelet domain with average scaling exponents.

[6] Scale changes by a factor of 2

3.5.6 Wavelet Transform Modulus Maxima (WTMM) method

The Continuous Wavelet Transform is highly redundant as there is a large overlap between successive wavelets as they are continuously translated through a time series. A much less redundant representation of the transform is the Wavelet Transform Modulus Maxima (WTMM). Mallat introduced this representation in the early 1990s for the analysis of non-stationary multifractal series. It is based on the identification and linking of local maxima values in the CWT transform, and it retains the benefits of the translation-shift characteristic of the CWT (Struzik and Siebes, 1999).

The scaling behaviour of a multifractal time series is closely related to the distributions of local singularities in a series. The number of singularities varies at different scales in a hierarchical manner (Struzik, 1999) and this can clearly be observed in the peaks of a CWT and its modulus maxima tree, as shown in Figure 37. The maxima lines follow the peaks in the transform and each one of them converges towards a singularity in the time series. The same feature of a range of singularities in a time series is shown in the Singularity Spectrum where the range of roughness is represented by local Holder exponent values.

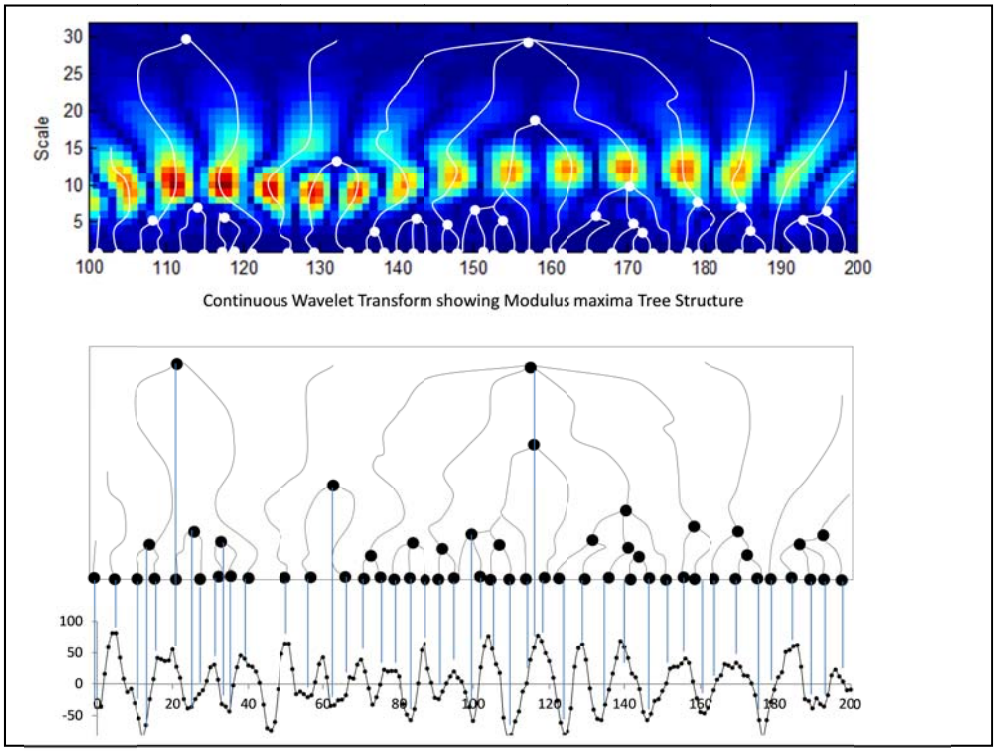

Figure 37: Schematic detail of the wavelet modulus maxima line configuration.

The Modulus Maxima Tree structure provides a visual means of interpreting the non-linear fractal geometry of a series enabling characteristics to be identified and compared.

3.5.7 Singularity power spectrum

Given the fact that the more significant singularities in a time series as represented by the local Holder exponents, are correlated with the crests and troughs of the series, the envelope of the these values can be used to represent the temporal power distribution of the series in a similar way to the SIWEH. A significant difference between the Singularity Power Spectrum (SPS) and the SIWEH is that the former spectrum identifies the temporal energy distribution as a function of wave period.

SPS envelopes for wave periods of 5, 10, 15 and 20 seconds have been shown for a typical time series in Figure 38. The SPS envelopes have been shown together with the time series and the wavelet transform from which they have been derived.

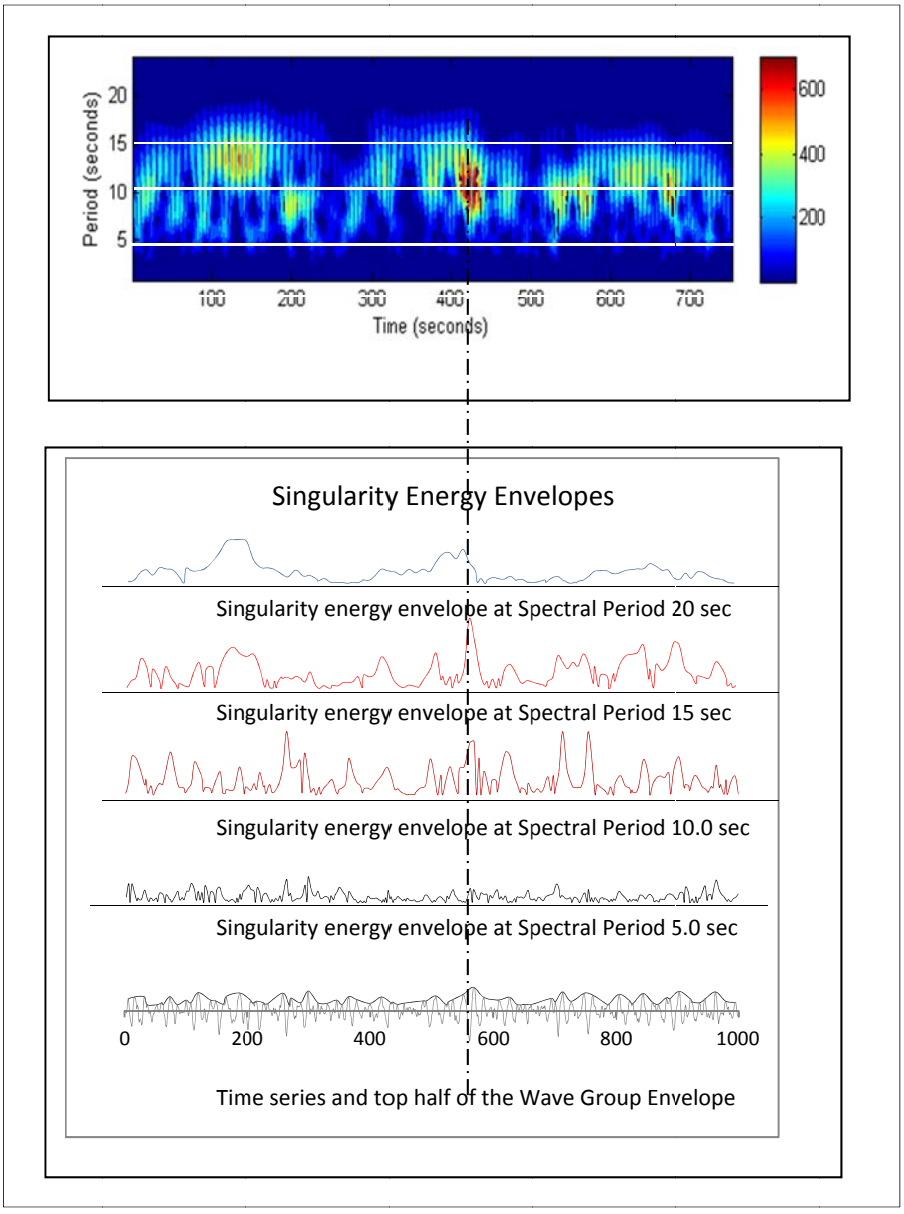

Figure 38: Singularity power spectrum envelopes of typical time series.

Period averaged SPS can be derived for a range of wave periods by averaging the sum of the wavelet coefficients over the selected range of wave periods.

3.6 Summary of Chapter 3

Chapter 3 sets out a summary of the literature relating to the theory of fractal structures and dimensions and it describes the different dimensions that have been used in the research.

The chapter goes on to give details of the different methods of fractal analysis that have been used in the research in both the times and frequency domains.

The concept of Singularity Power Spectrum envelopes is introduced and their overall similarity to the SIWEH is discussed.

4. DATA SELECTION

The objective of analysing the data in this research is to firstly investigate whether or not ordinary sea states and sea states incorporating bound long waves are multifractal systems. Secondly, in the event that the sea states are found to be multifractal systems, then the research will go on to determine whether or not these seas states can be characterised by their multifractal dimension or indices. Finally, the research will be directed towards the identification of longer term singularity distributions and infragravity wave characteristics.

The first of the above objectives will be investigated by using fractal anlysis methods to analyse the following data :

- Time series collected from an open lake water wave field, and
- Time series derived mathematically from a simplifed JONSWAP spectrum

The time series data representing the open lake water wave field comprises 150 records collected at a rate of 10 Hz over a15 second duration, and the mathematically derived time series data comprises 3600 records collected at a rate of 2 Hz over a 30 minute duration.

The last two objectives will be investigated by using fractal analysis methods to analyse time series data collected from the open sea at Saldanha Bay and Ngura harbours. These time series will be comprised of both 1000 and 2304 records collected at rates of 1.33 Hz over durations of 12.5 minutes and 30 minutes respectively.

4.1 Length of series

This research has been based on the fractal analysis of sea surface displacements associated with infragravity wave systems to identify whether or not these systems can be characterised by a set of fractal indices. The periods of the waves generally

associated with the restraining wave groups in bound infragravity waves systems are in the order of 4 to 25 seconds (Okihiro et al. 1992).

In 2003 Katsev and L'Heureux investigated the use of short time series for the determination of meaningful Hurst exponent values. He analysed a series with a known average Hurst exponent value of .5 and found that the standard deviation of exponents derived from short series with lengths ranging from 100 to 700 data varied from .18 to .12, respectively. The full range of standard deviations and coefficients of variation are recorded in Table 13.

Table 13: Standard deviation of Hurst exponents derived from short series.

Length of Data set	Standard deviation σ	Coefficient of Variation (Relative Standard deviation) = $\frac{\sigma}{(Average = .5)}$
100	.18	36 %
150	.17	34 %
200	.15	30 %
250	.14	28 %
500	.12	24 %
700	.11	22 %

[Ref: Katsev and L'Heureux et al. 2003]

In 2006 Delignieres carried out research to evaluate the performances of typically used methods of fractal analysis with short periods. These methods included Rescaled Range, Power Spectral Density and Detrended Fluctuation Analysis techniques (Delignieres et al. 2006). The aforementioned methods were tested against a simulated exact fractal series.

Delignieres used noted that series with lengths of 2^9 or 2^{10} records were considered to be an acceptable compromise between shorter series, with length of 2^6 or 2^7 (64 to 128) records, and longer ones with a length of 2^{12} (4 096) records for the purposes of fractal analysis (Delignieres et al. 2006).

Delignieres found that the Power Spectral Density method of fractal analysis 'works quite well' for the analysis of fGn series, although there is an underestimation of Hurst exponent values H < .4 and a slight overestimation for Hurst exponent values H > .7. He also found that the length of series did not have a significant influence on the magnitude of the aforementioned biases, except in the case of the shortest series with a length of 64 records. Further, Delignieres found that the Detrended Fluctuation Analysis method for fGn series did not have any bias for negative effects due to the length of series (Delignieres et al. 2006).

4.2 Data used in analysis

The following data has been selected for analysis:

- Time series derived from sequential video images of a fully dimensioned Open Lake Water wave field,
- Mathematically generated bound long wave time series
- Time series data collected before and during the occurrence of hazardous bound long wave sea states at Saldanha Bay , and Ngqura Harbours.

The time series derived from the video imagery has been selected for analysis because it represents a section of an ordinary wave train and provides the ability to compare derived fractal dimension sets with spatial images of the water surface that they represent.

The mathematically generated bound long wave time series was selected for analysis in order to validate the fractal analysis techniques used for the characterisation of open water bound long wave sea sates

The time series data collected from the open sea at Saldanha Bay and Ngqura harbours was selected in order to be able to compare the fractal dimensions and distributions of two sea different sea states in order to characterise then quantitavly.

4.3 Sequential video images of a fully dimensioned open lake water wave field

4.3.1 Recording of spatial wave field images.

Close range photogrammetric processes in open lake water in Lake Michigan, USA, recorded open water spatial wave field images. This was undertaken in accordance the Automated Triangular Stereoscopic Imaging System (ATSIS) process (MacHutchon et al. 2009) and includes the following activities**:**

- The planning of the camera cluster
- The calibration of the camera cluster
- The carrying out of fieldwork
- Post processing
- The combining of individual Digital Sea Surface Model (DSSM) frames
- The development of selected DSSM Profiles
- The integration of sequential DSSM Profiles into a time series for analysis.

4.3.1.1 Description of Data

The wave field data analysed was comprised of a 3 Dimensional (x, y and z), sequence of digital video imagery recorded at a rate of 10 Hz for 15 seconds. The Department of Civil and Environmental Engineering at the University of Wisconsin-Madison recorded the imagery in open lake water on the Great Lakes in the USA. They also processed to imagery under the direction of Professor Chin Wu to obtain a dimensioned digital model of the lake surface. The dimensions of the recorded portion of water were 4.5 m x 2.5 m and the surface resolution of the images was 1 cm/pixel.

4.3.1.2 Camera Cluster Details

The ATSIS consists of three IEEE-1394 video cameras mounted to adjustable pan/tilt tripod head as shown in Figure 39. The cameras are capable of capturing 100 frames per second at resolution of 640 x 480 or more. It is a portable system that can be easily managed in the field. An image photogrammetry processing technique, including area-feature hybrid matching, was developed to accurately quantify the area

of images taken from oblique angles. The ATSIS has been found to be able to achieve 1 mm resolution in wave height measurement.

Figure 39: Typical camera set-up for capturing of stereoscopic video imagery

Each camera is fitted with a 16mm lense with a field of view of 22^{o} x 160^{o} in the horizontal and vertical directions respectively with a resolution of 640 x 480 pixels. These three cameras are synchronized and captured images are directly recorded to a hard disk drive on a personal computer through IEEE 1394 cables.

4.3.1.3 Calibration of camera cluster

Camera calibration plays a major role in stereo imaging and a two-step procedure incorporating a laboratory calibration, for the purpose of correcting lens distortion and finding the location of the principle point was adopted; this is prior to field deployment and field calibration to obtain the orientation and position of the site set-up.

4.3.1.4 Post-Processing

Post-processing operations comprise the matching of a point on one image to a corresponding point on another image. This process is essential to obtain a three-dimensional object coordinate and two methods were used for the matching. The first method resolves specular reflection, and the second method matches a triplet of image points. The first method allows any two images to establish a match; but the object point depth is usually calculated using the left and right cameras whose base distance is the largest, thus maximizing depth resolution. The second method starts with the formation of a square window around pixel (x_{iL},y_{iL}) in the left image, and incorporates a one–dimensional search along an epipolar line in the centre image to identify the corresponding pixel. A normalised cross-correlation (NCC) of intensity values in the search and stationery window is used to measure the likelihood of a match. The centre pixel of the search window where the highest NCC value occurs is stored for subsequent sub-pixel matching if the NCC exceeds 0.7. If the highest NCC value does not exceed this value, it is regarded as a no-match. Once the corresponding point on the centre image is determined, the third point on the right image can readily be identified through the intersection of two epipolar lines. Once the coordinates on the pixel in the right image (x_{iR},y_{iR}) have been determined, the three-dimensional coordinates of the identified pixel can be derived.

4.3.2 Analysis of open lake water spatial data frames

Three dimensional wave features can be derived and examined for selected wave-field footprints, as illustrated in Figure 40 where six sequential scenes, each 1.0 second apart, are shown.

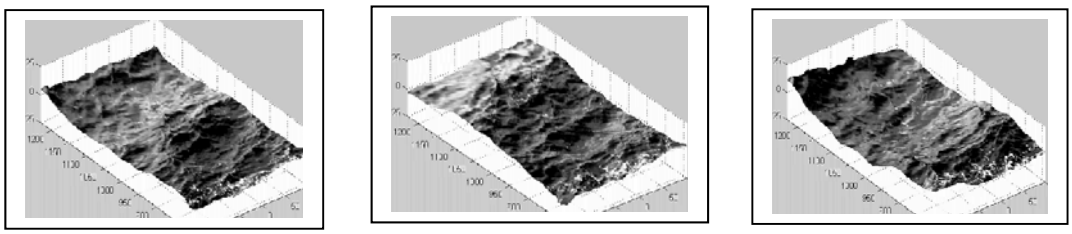

(a) (b) (c)

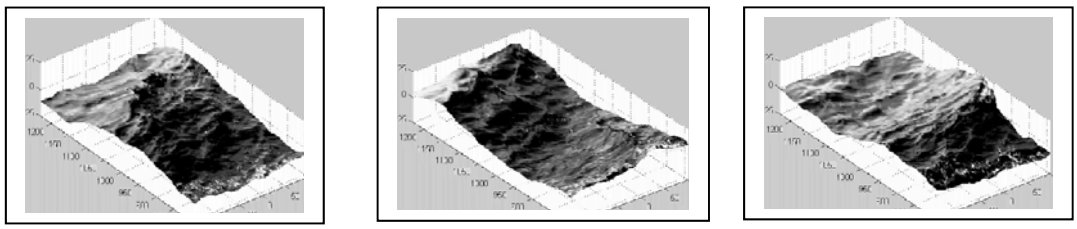

(d) (e) (f)

Figure 40: (a), (b), (c), (d), (e) and (f): Typical sequential series of digital sea surface Model scenes.

The images in Figure 41 show a three-dimensional breaking wave with a short and well-defined crest length. The shape of the breaking wave can clearly be determined from the topographic map and its height and length can be calculated from the contour plot. Another advantage of the ATSIS output is that wave steepness trends, along the wave crest, can also be quantified and analysed.

The water surface displacements of the Digital Sea Surface Model have been validated with a wire wave gauge and an excellent correlation was found between the surface displacements measured by the different means.

ATSIS not only provides a record of direct visual observations, but also provides quantitative information on three-dimensional wave breaking characteristics in the open ocean, which can be measured and displayed as shown in Figure 41.

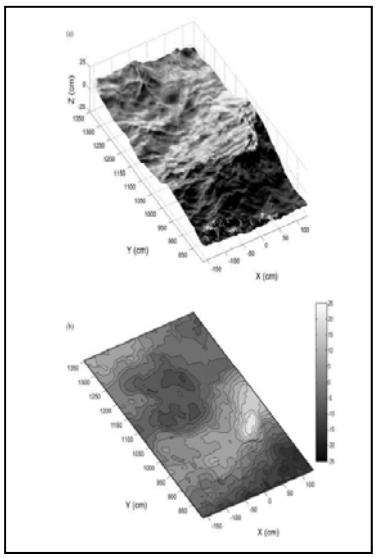

Figure 41: Three-dimensional topographic and contour maps of the sea surface, showing breaking wave conditions

Individual single point time series data sets were derived from the sequence of video images by linking consecutive surface displacements of a single point in the spatial data into a time series, as shown diagrammatically in Figure 42.

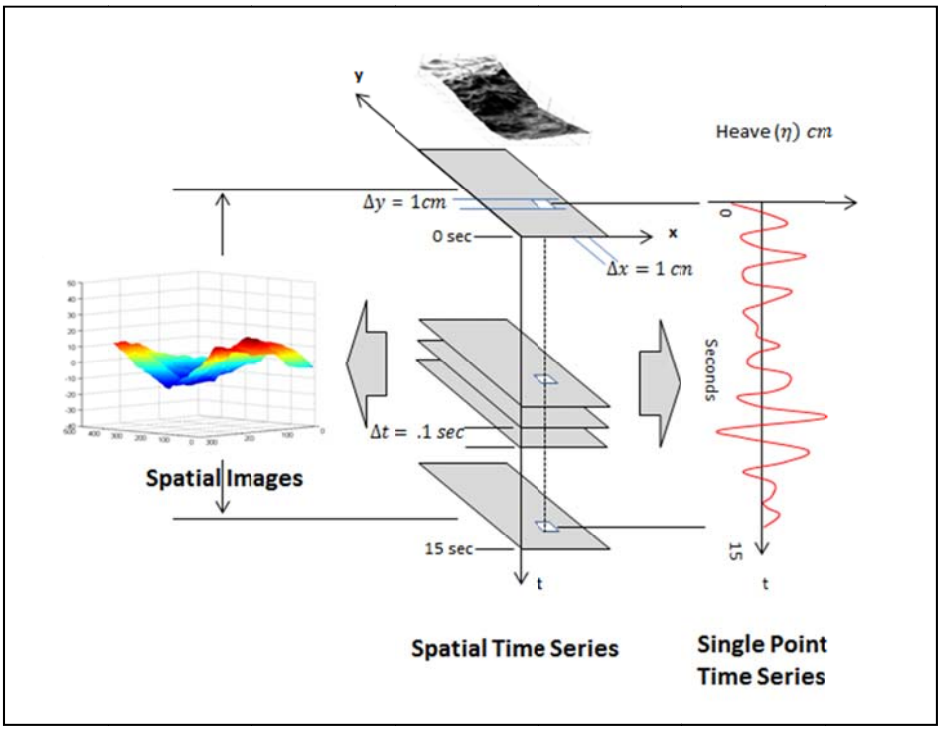

Figure 42: Diagram showing how spatial images and time series data can be derived from the stereoscopic video record of the breaking wave sequence

4.4 Mathematically generated bound long wave time series

Three synthetic bound long wave time series 12sec(Series1), 12 sec(Series2) and 18sec(Series1), derived by Diedericks and Terblanche at the University of Stellenbosch, were made available for this research. The series were constructed by creating a simplified JONSWAP spectrum and calculating a number of short wave components from it. The bound long wave components were then calculated from interacting short wave components.

The parameters of the series are shown in table 14.

Table 14: Mathematically generated time series parameters

Series Name	Significant wave height (Hs)	Peak Period (Tp)	Peakedness factor (γ)
12sec(Series1)	2.0 m	12.0 seconds	2.0
12 sec(Series2)	2.0 m	12.0 seconds	2.0
18 sec(Series1)	2.0 m	18.0 seconds	5.0

The time series 12sec(Series1) and 12sec(Series2) are very similar with the only difference being that different pairs of short wave frequencies have been combined to generate the different series. The time series 18sec(Series1) is very different from the others in that the peak period is longer and the peakedness factor is increased from 2 to 5.

The peakedness factor is a measure of spectral shape which is closely related to the degree of wave grouping in the time series as follows. The larger the peakedness factor, the narrower the wave spectrum and the greater the wave grouping in the series.

4.5 Saldanha Bay Harbour time series data

Raw single point time series data, recorded by the waverider buoy at the Saldanha Bay harbour by the CSIR on 26 and 28 September 2013 were made available for this research by the CSIR with approval from Transnet National Ports Authority.

The days, times and number of records used in this research are detailed in Table 15

Table 15: Saldanha Bay Harbour data record details

Time	Number of records (recorded on the hour at 0.78 second intervals)							
	26 September 2013		26 September 2013		22 June 2013	25 June 2013	13 August 2013	18 August 2013
	No. of records	No. of records	No. of records	No. of records	No. of records	No. of records	No. of records	No. of records
06:00	Data sets of 1000 records with duration of 13.0 minutes	Data sets of 2304 records with duration of 30.0 minutes	Data sets of 1000 records with duration of 13.0 minutes	Data sets of 2304 records with duration of 30.0 minutes	Data sets of 2304 records with duration of 30.0 minutes	Data sets of 2304 records with duration of 30.0 minutes	Data sets of 2304 records with duration of 30.0 minutes	Data sets of 2304 records with duration of 30.0 minutes
09:00								
12:00								
15:00								
18:00								
21:00								

All of the data that was collected on the 26th and 28th September 2013 was typically carried out on sets of data comprising 1000 records with durations of 13.0 minutes. In addition, sets of 2304 records with durations of 30 minutes, was also carried out for these periods using MDFA and Wavelet Transform analysis methods.

The data that was collected on the days and times during June and August 2013 was analysed on the basis of data sets with 2304 records, and durations of 30 minutes, using MDFA and Wavelet Transform methods

4.6 Ngqura Harbour time series data

As in the case for the Saldanha Bay harbour, two independent sets of six single point time series data, recorded on the 6th and 7th as well as on the 8 August 2012, were made available for this research by the CSIR. The days, times and number of records used in this research are detailed in Table 16:

Table 16: Ngqura Harbour data record details

<table>
<tr><th colspan="2">6 and 7 August 2012

Number of records (recorded on the hour at 0.78 second intervals)</th><th colspan="3">8 August 2012

Number of records (recorded on the hour at 0.78 second intervals)</th></tr>
<tr><td></td><td>Number of Records</td><td></td><td colspan="2">Number of Records</td></tr>
<tr><td>19:00</td><td>864 records with duration of 11.23 minutes</td><td>05:00</td><td rowspan="6">Data sets of 1000 records with duration of 13.0 minutes</td><td rowspan="6">Data set of 2304 records with duration of 30.0 minutes at 21:00 hrs. only</td></tr>
<tr><td>21:00</td><td rowspan="5">Data sets of 1000 records with duration of 13.0 minutes</td><td>10:30</td></tr>
<tr><td>23:00</td><td>15:00</td></tr>
<tr><td>01:00</td><td>17:00</td></tr>
<tr><td>03:00</td><td>19:00</td></tr>
<tr><td>05:00</td><td>21:00</td></tr>
</table>

4.7 Summary of Chapter 4

Chapter 3 provides comments on the lengths of the time series that were analysed with a view to evaluate the validity for their selection and to determine to what degree they would affect the significance of the results obtained.

Details of the sources of the different data samples are given together with the methods that were used to collect them.

5. ANALYSIS OF MEASUREMENT DATA

The measured data collected from the open lake water wave field and from the open sea will be analysed by means of the following methods:

- The R/S method in the time domain
- The MDFA method in the time domain
- The Spectral exponent method in the Fourier and wavelet domains, and
- The Wavelet Transform method in the Time-Frequency domain

The first three methods will be used for the processing of the 150 data series from the open lake water wave field. All four methods will be used for the processing of the 1000 data series from the open sea at Saldanha bay and Ngqura harbours, and the last two methods will also be used for the processing of the 2304 data series from the open sea at the harbours

5.1 Analysis software

The analysis of the data was carried out in EXCEL by means of standard product routines and spreadsheet models, and in MATLAB it was undertaken using standard product routines, public domain toolboxes available on the Internet and MATLAB script files specifically written for the purposes of this research.

5.1.1 Spreadsheet models

Spreadsheet models were developed and used as part of the research for certain of the very repetitive processes including the implementation of the Rescaled Range analysis method.

5.1.2 MATLAB toolboxes and script files

A public domain MATLAB Toolbox (Ihlen. 2012) was used for the Multifractal Detrended Fluctuation Analysis (MFDA) of the various time series.

Ihlen wrote the MDFA toolbox in 2012 and it is distributed for public use in terms of the Creative Commons Attribution Non-Commercial License, which permits non-commercial use, distribution and reproduction in other forums provided that the original authors of the source are credited. EAF Ihlen works in the Department of Neuroscience at the Norwegian University of Science and Technology, Trondheim, Norway.

MATLAB script files for the integration of standard MALAB and other repetitive analysis processes were developed and used as part of the normal analysis process.

5.2 Open lake water spatial wave field time series

5.2.1 General

The surface layout of the open lake water spatial wave field was divided up into a grid layout as shown in Figure 43 and single point time series surface displacements were determined from the dimensioned images for the eight grid points shown as squares in the figure. The grid references of the points are recorded in in Table 17. The point of white capping on the breaking wave is marked with a circle at the (Row, Column) coordinate of (319,230).

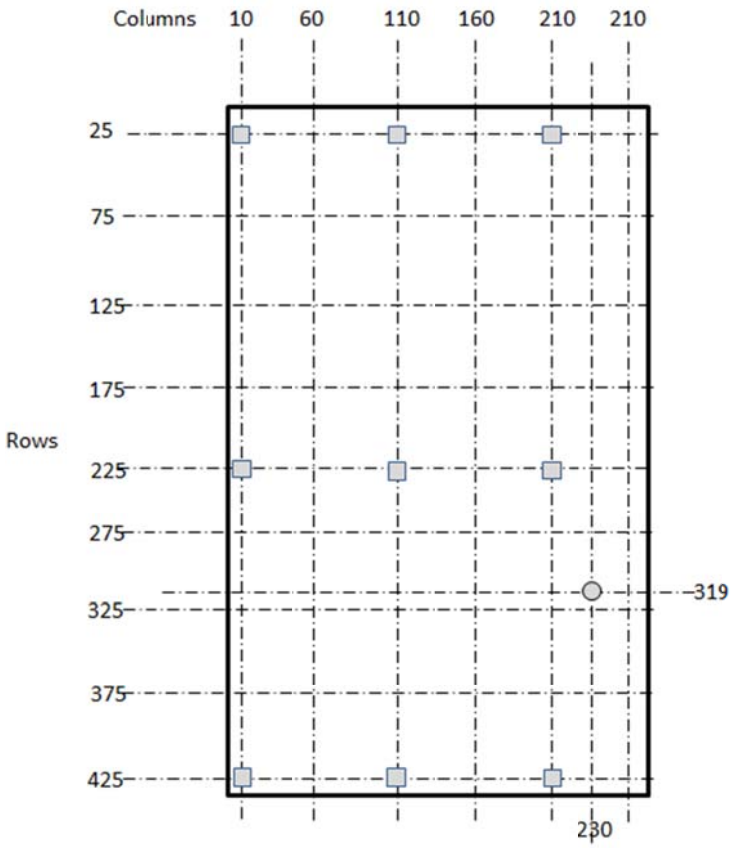

Figure 43: Diagrammatic layout of the analysis grid which was superimposed on the wave field.

Table 17: Coordinates of time series in open lake water wave data

Position	Grid Reference	
	Row	Column
1	25	10
2	As above	110
3	As above	210
4	225	10
5	As above	110
6	As above	210
7	425	10
8	As above	110
9	As above	210

Time series were derived for all the co-ordinates given in Table 16 and the series for co-ordinates (25,10), (25, 110) and (25,110) have been shown in Figure 44 in order to illustrate the consistency and level of detail that can be derived from the dimensioned video imagery.

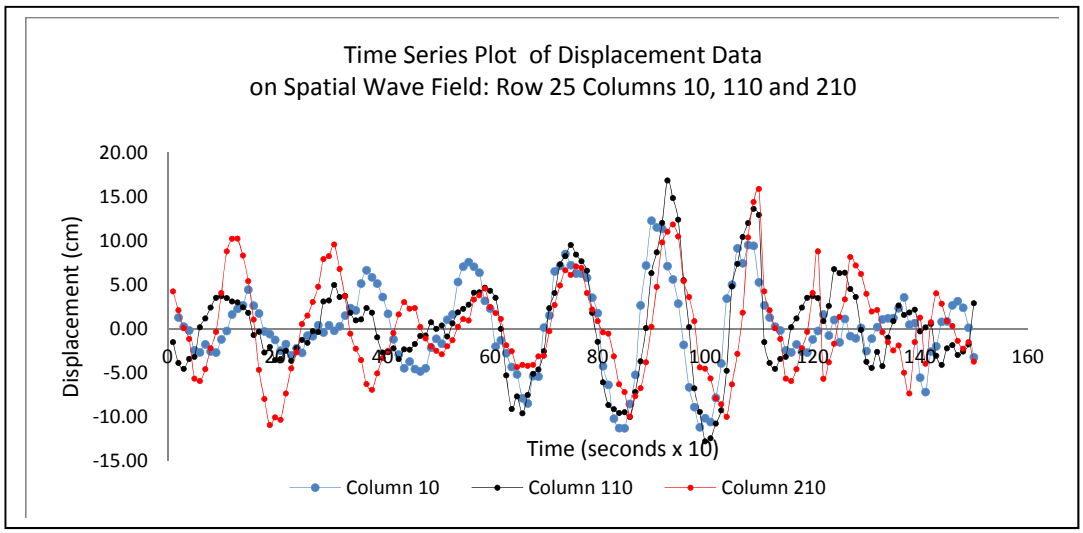

Figure 44: Time Series of surface displacements on grid co-ordinates (25,10), (25,110) and (25, 210)

The time series on grid co-ordinate (225,210) has been shown in Figure 45, together with selected images of the wave field surface at the times of the respective surface displacements, to illustrate the benefit of being able to relate the series to a wave field.

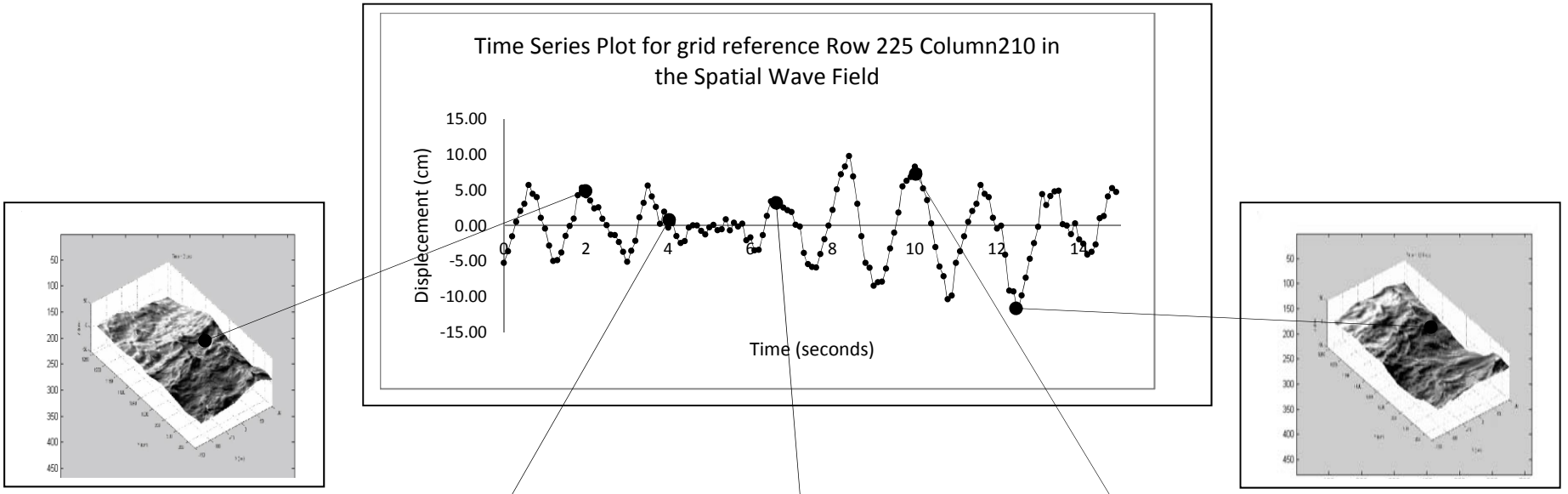

Figure 45: Time series on grid co-ordinate (225,210) with selected wave filed images

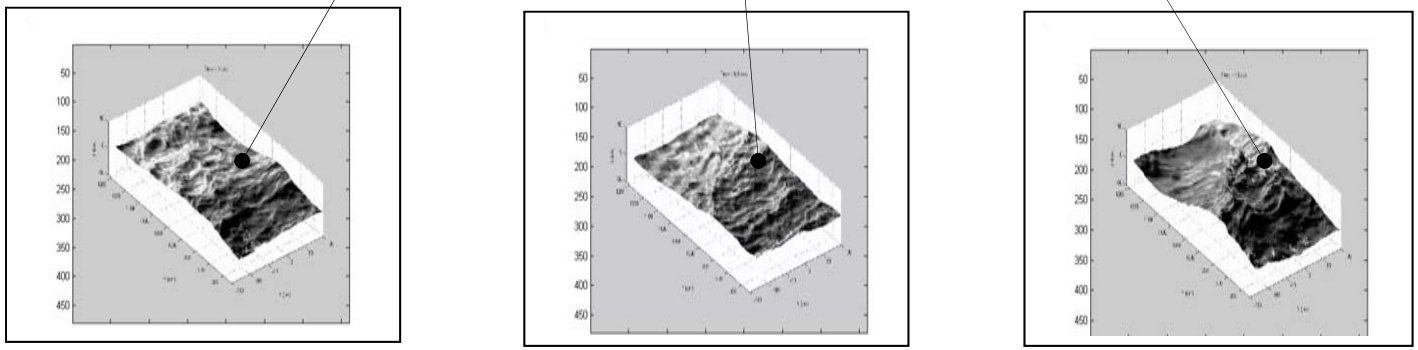

5.2.2 Time Domain analysis

5.2.2.1 Rescaled Range analysis method

Rescaled Range (R/S) Analyses were carried out for the eight time series derived from the spatial wave field data, and a typical scatter plot as well as linear regression trend lines of the results has been shown on the log-log plots in Figures 46.

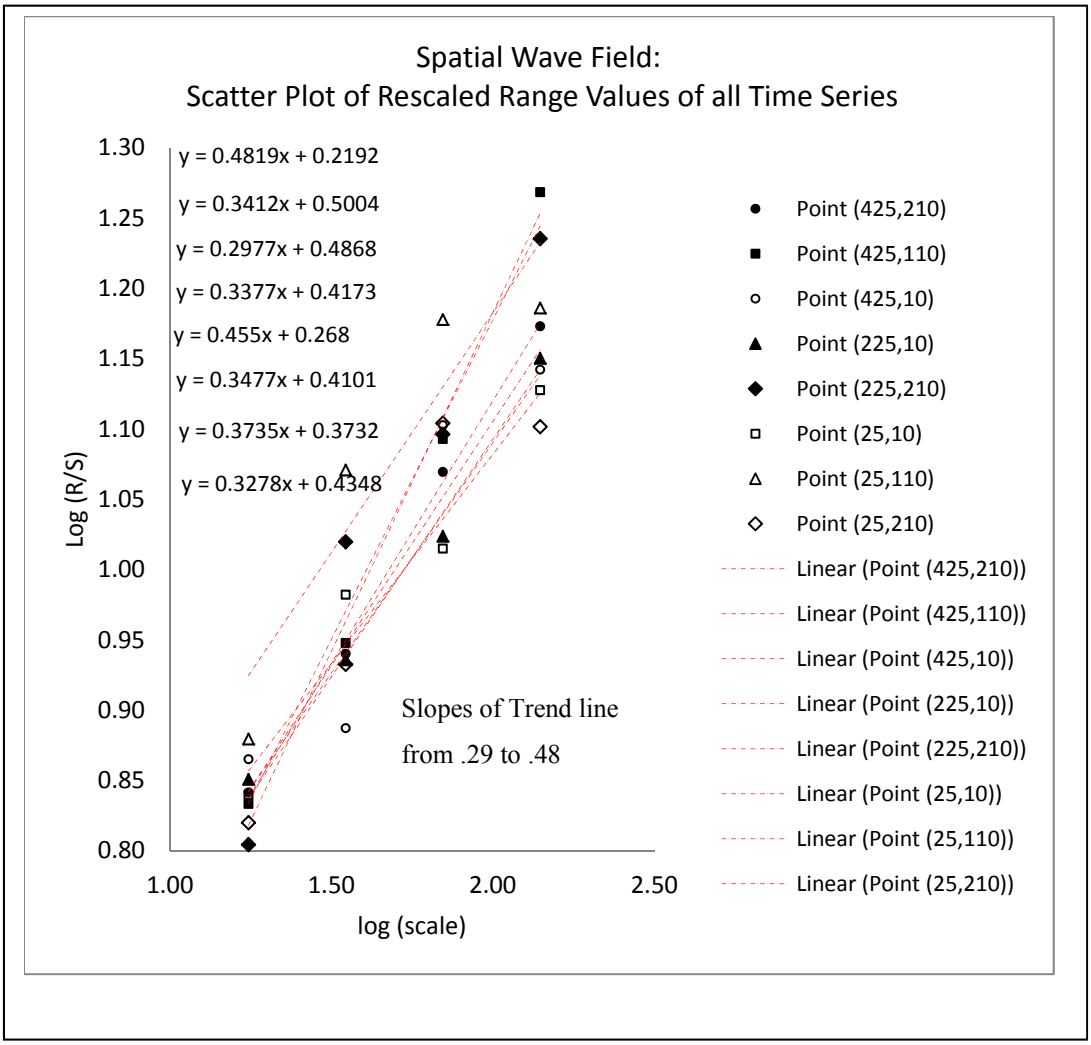

Figure 46: Scatter plot of rescaled range values of open lake water wave field data

As can be seen from the plots in Figure 45, the derived Hurst exponent values based on the slope of the trend lines range from 0.29 to 0.48 with an average value of 0.39. The standard deviation of the exponent values .065 and the coefficient of variation

(CoV) is [0.065/.39] x 100 = 16 %. Katsev and L'Heureux (2003) found that short time series with 150 records could have a (CoV) of 34 per cent and therefore the exponent values as considered to be statistically significant.

5.2.2.2 Multifractal Detrended Fluctuation Analysis (MDFA) method

Representative Singularity spectra, for the single point time series on grid coordinates (25,110), (225 110) and (425 110), have been shown in Figure 47.

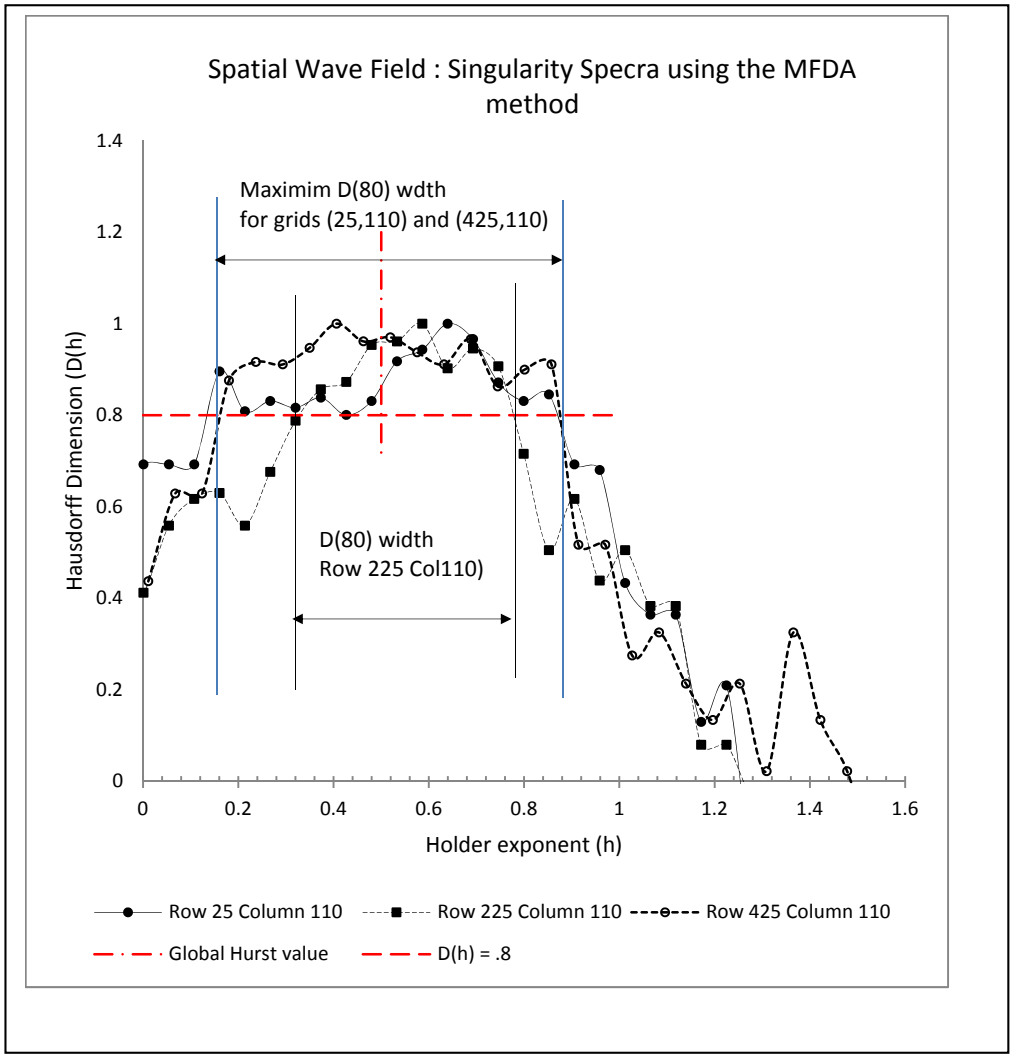

Figure 47: Singularity spectra for the single point time series on grid coordinates (25,110), (225 110) and (425 110)

The time series on grid (425,110) has a peak Holder exponent value, h(p), or local Hurst value, of 0.4. This value is similar to the average global Hurst value of 0.39, which was derived in section 5.2.2.1. The h(p) values for the other two series is higher with values of 0.59 and 0.6, and these values are comparable with the maximum Hurst exponent value of 0.48 that was derived from section 5.2.2.1.

The D(80) width of the series on row 25 and 425 are similar, with a roughness, or fractal width range of 0.7. The D(80) value of the time series on grid point (225,110) is narrower and equal to 0.45, indicating that the surface displacements in the vicinity of this point will be more regular than elsewhere in the wave field.

It is worth noting that the lowest peak Holder exponent value of the three singularity spectra, which indicates the roughest global surface displacements, occurs at grid point (425,110) in the region of the breaking wave crest.

The singularity spectrum for the time series on grid coordinate (225,110) has been shown together with the relative frequencies of occurrence of the different Holder exponents in Figure 48.

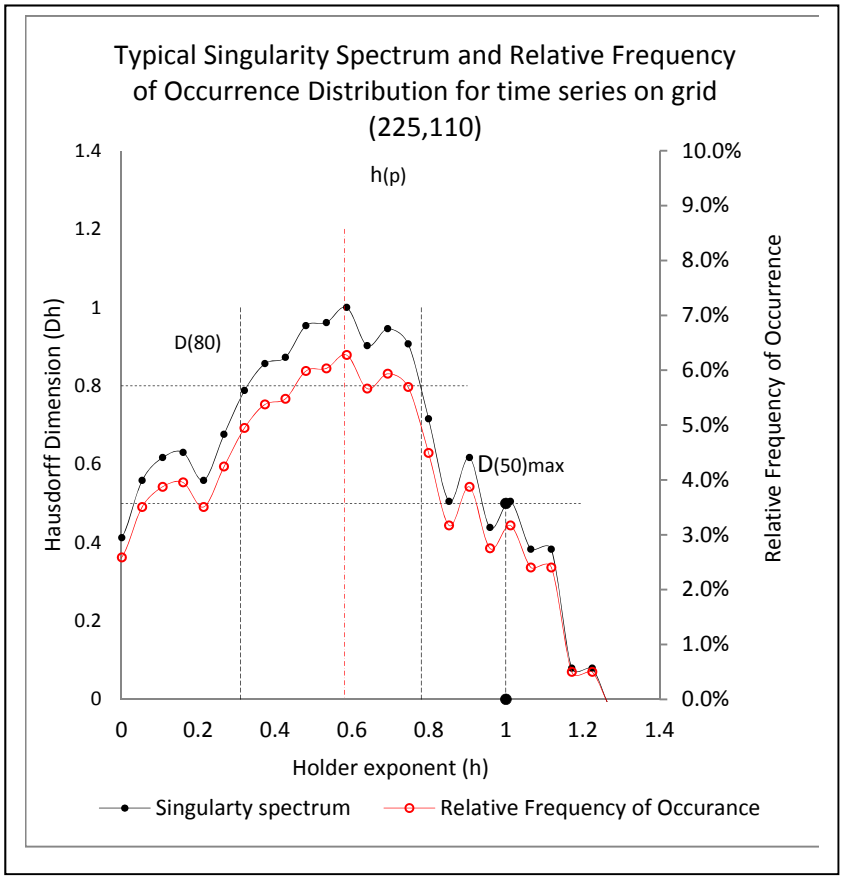

Figure 48: Singularity and relative frequency of occurrence

The relative frequency of occurrence plot in Figure 48 enables one to interpret the overall roughness structure of a time series more clearly. It is interesting to note that the most frequently occurring roughness in the time series on grid (225,110) only occurs for some 6 per cent of the time.

The cumulative frequency, or probability of non-exceedance, plots of the Holder exponents in the three time series have boon shown in Figure 49.

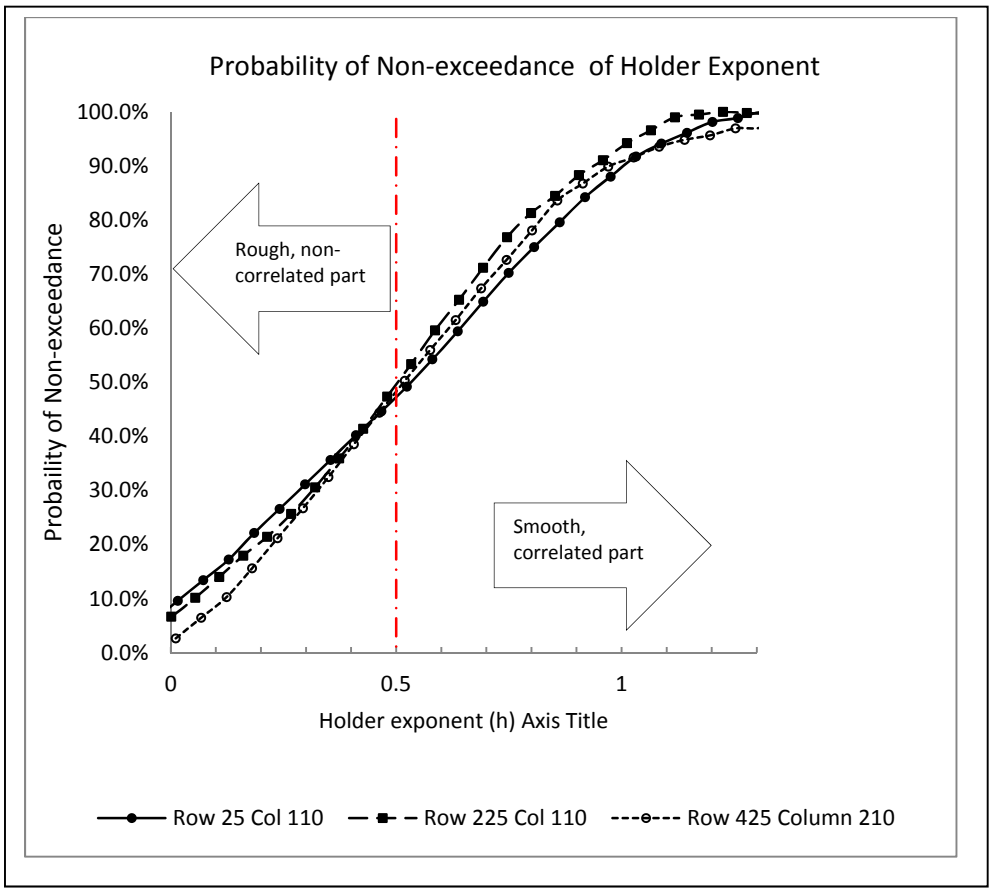

Figure 49: Cumulative frequency or probability of non-exceedance curves

The three probability curves in Figure 48 are very similar with all three series having a close to 50 per cent probability of not exceeding a Holder exponent value of 0.5. They also all have a similar probability of exceeding this exponent value.

5.2.3 Frequency Domain

5.2.3.1 Power Spectral Density Spectrum (PSD) Analysis in the Fourier Domain

Power Spectral density plots for the time series in Figure 43 have been shown in both normal and log-log plots in Figures 50 and 51, respectively. The plots for the other time series on grid co-ordinates (225, 10), (225, 210), (425, 10), 425, 110) and (425,210) are similar.

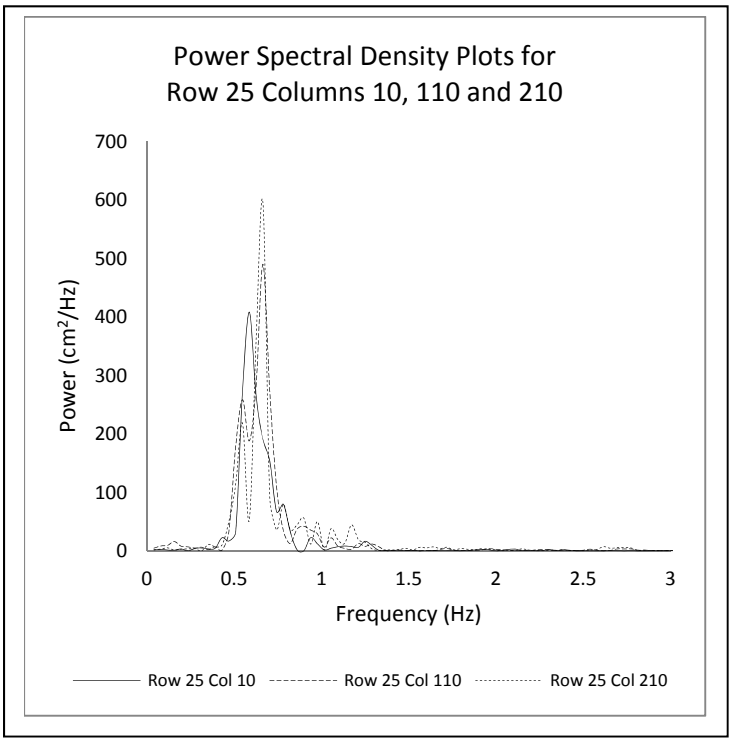

Figure 50: Power spectral density plots of time series.

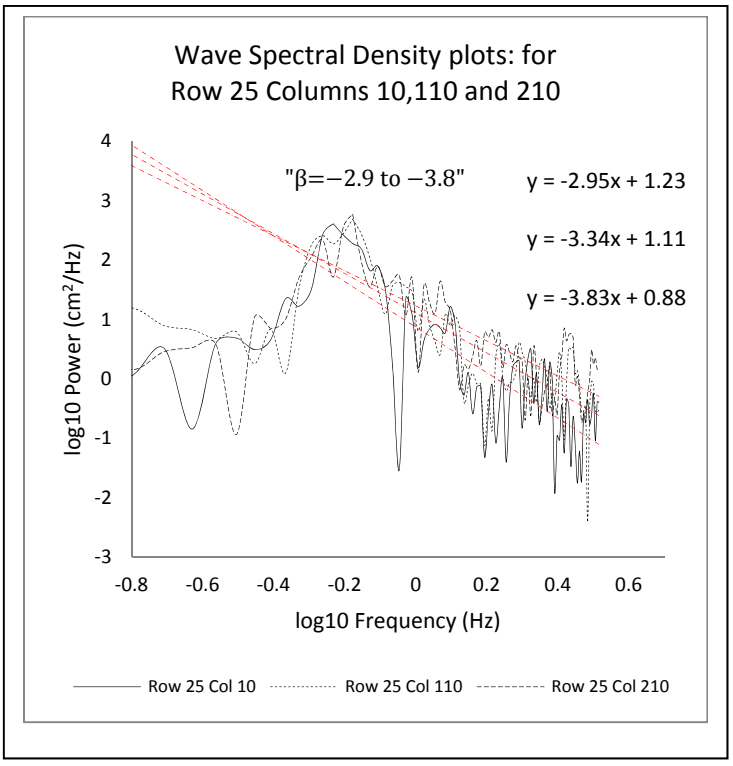

Figure 51: Log-log plot of power spectral density plots.

The peak frequencies of the different time series derived from the spatial wave field range from .6 to .7 Hz with corresponding periods ranging from 1.7 to 1.4 seconds respectively.

The spectral slope β for the different power spectral density functions range from -2.9 to -3.8 indicating the series has a short term correlation, or persistence, characteristic.

5.2.3.2 Power Spectral Density Spectrum (PSD) Analysis in the Wavelet Domain

Spectral scaling exponents in the wavelet domain for the time series shown Figure 43 have been shown in Figure 52. The plots for the other time series on grid co-ordinates (225,10), (225,210), (425,10), 425,110) and (425,210) are similar.

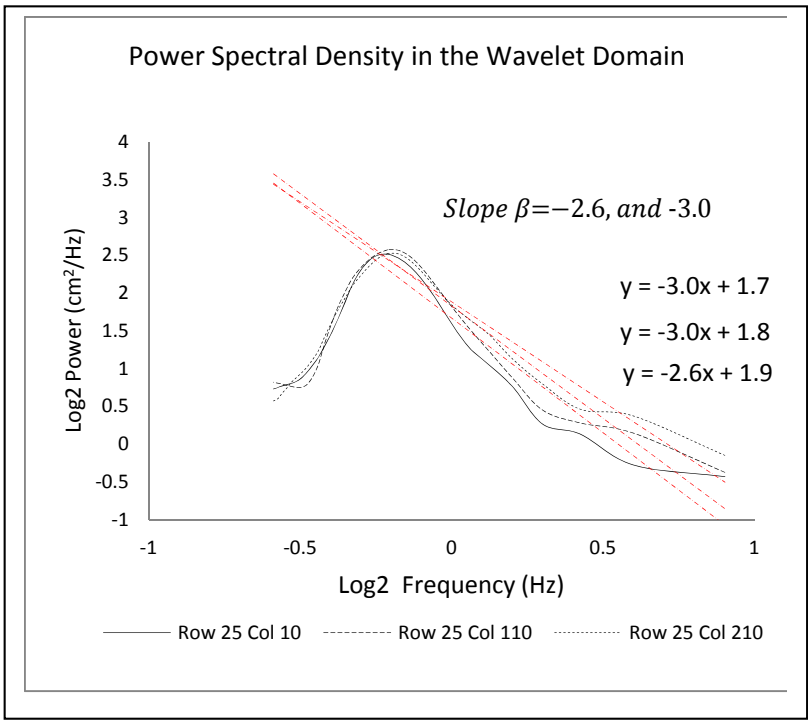

Figure 52: Spectral exponent in the wavelet domain

The scaling exponents calculated in Sections 5.2.3.1 and 5.2.3.2 above have been summarised in terms of the different methods of analysis in Table 18.

Table 18: **Comparison of spectral scaling exponents**

Location of Time Series		**Method of Analysis and Scaling exponent**	
Row	Columns	Fourier Domain PSD Method	Wavelet Domain PSD Method
25	10, 110 and 210	-2.9 to -3.8	-2.6 to -3.0

The exponents for the Fourier domain are nominally generally greater than those for the Wavelet domain and this is probably due the fact that the former values are based on the assumption of a stationary series, while the latter takes variations in the series into account.

The lower slopes are associated with less short-term and more long-term correlation.

5.3 Analysis of mathematically generated time series

5.3.1 General

The mathematically generated bound long wave time series that have been used in this research are shown in figures 53 to 55 below

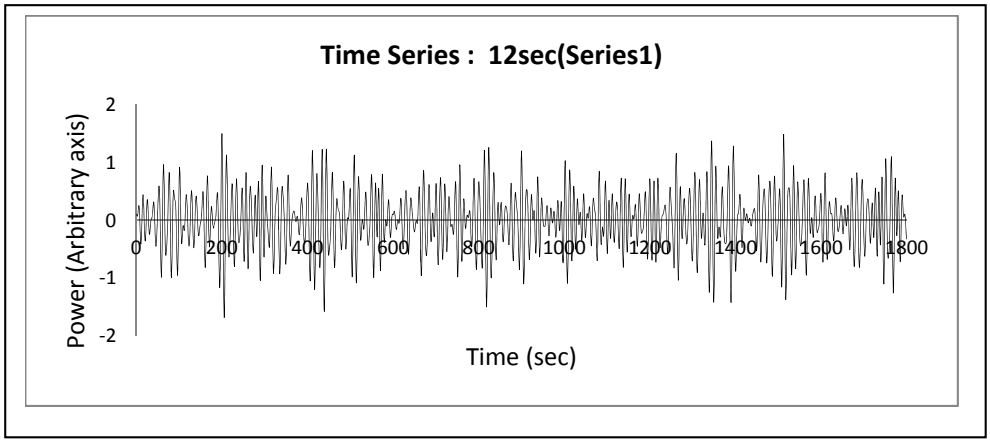

Figure 53: Time series plot of 12sec(Series1)

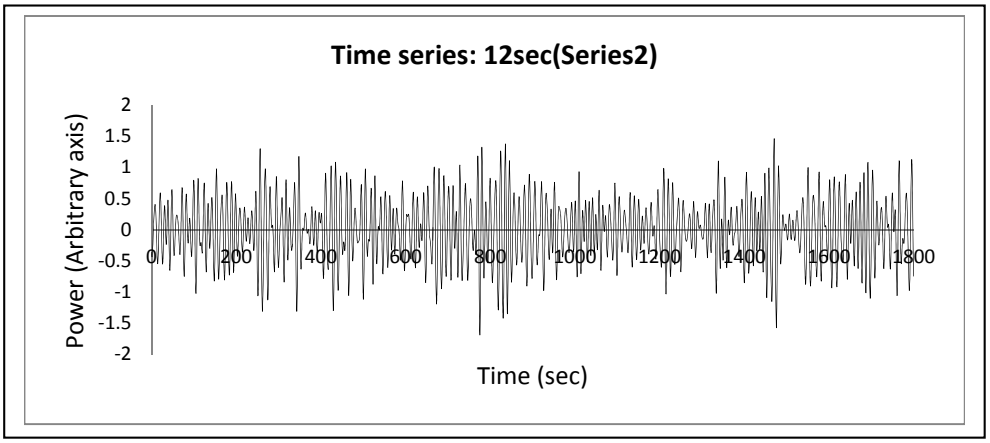

Figure 54: Time series plot of 12sec(Series1)

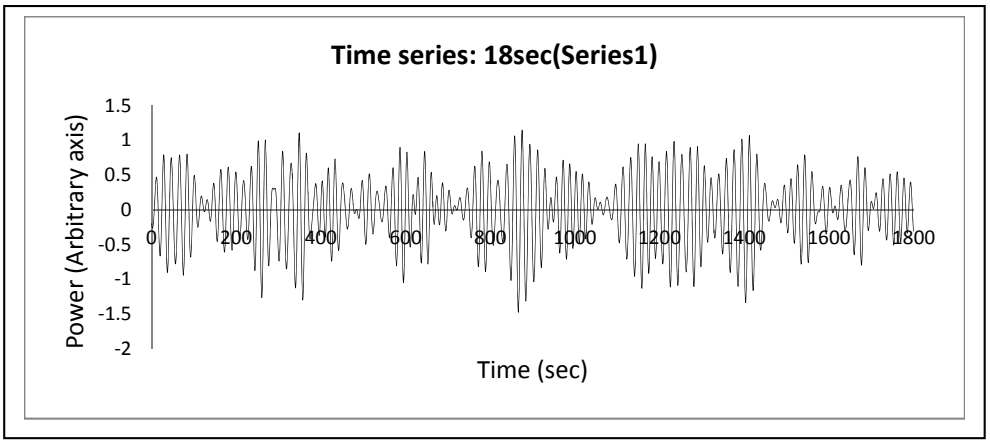

Figure 55: Time series plot of 18sec(Series1)

5.3.2 Time Domain Analysis

5.3.2.1 Multifractal Detrended Fluctuation Analysis (MDFA) analysis

The singularity spectra for time series 12sec(Series1), 12sec(Series2) and 18sec(Series1) have been shown in figure 56.

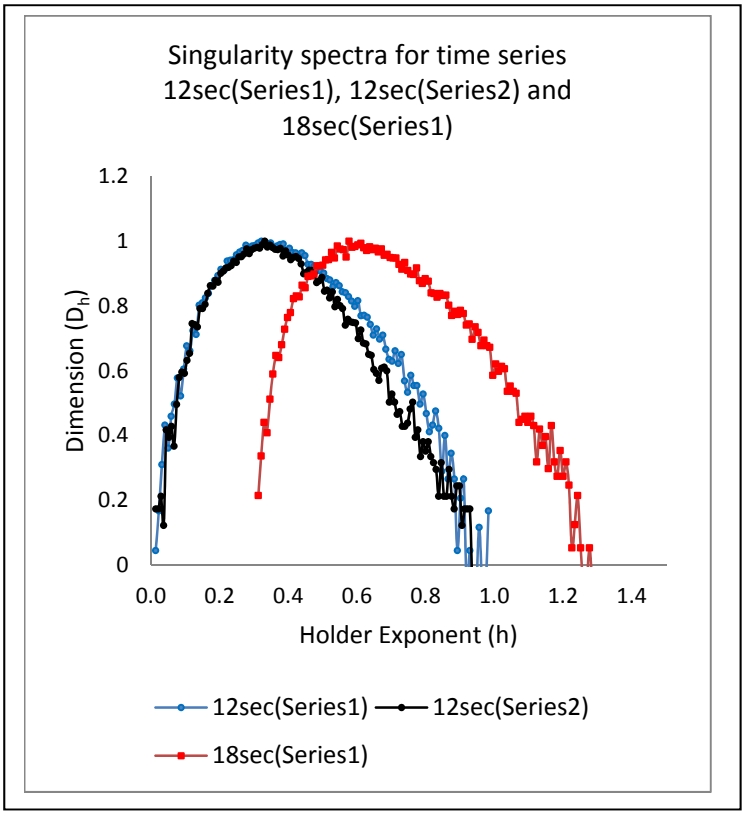

Figure 56: Singularity spectra for time series 12sec(Series1), 12sec(Series2) and 18sec(Series1)

The similarity between the spectra for series 12sec(Series1) and 12sec(Series2) can clearly be seen in figure 56. The figure also clearly shows that the spectrum for series 18sec(Series1) has shifted to higher holder exponent values indication a generally smoother and more regular shape to the series. This change in series shape with respect to the first mentioned series is also clearly evident from the plots in figures 53 to 55 inclusive, and it is line with what one would expect from a series with higher peak period and peakedness parameters.

The benefit obtained from the fractal analysis of the different series is that one can now characterise them by means of quantifiable dimensions, in accordance with their peak holder exponent values and different singularity distributions.

5.3.3 Frequency Domain analysis

5.3.3.1 Continuous Wavelet Transform Modulus Maxima (WTMM) method of analysis

Continuous Wavelet Transform spectra of time series 12sec(Series1), 12sec(Series2) and 18sec(Series1) have been shown in figures 57 to 59 inclusive.

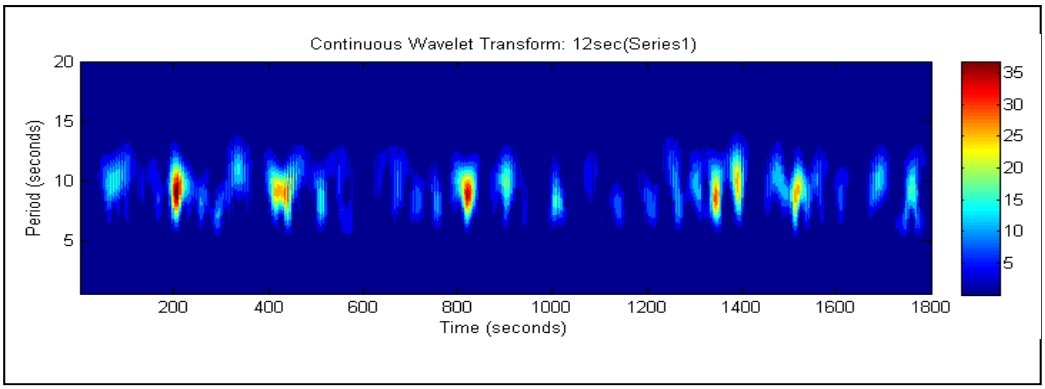

Figure 57: Continuous wavelet Transform of 12sec(Series1) time series

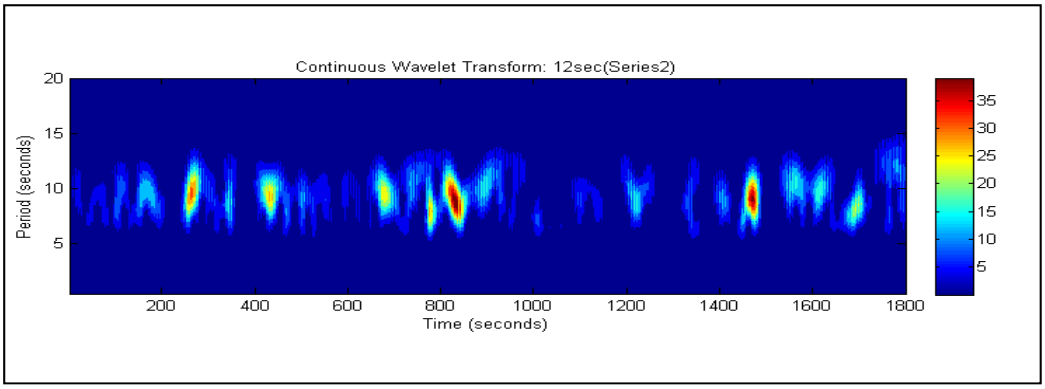

Figure 58: Continuous wavelet Transform of 12sec(Series2) time series

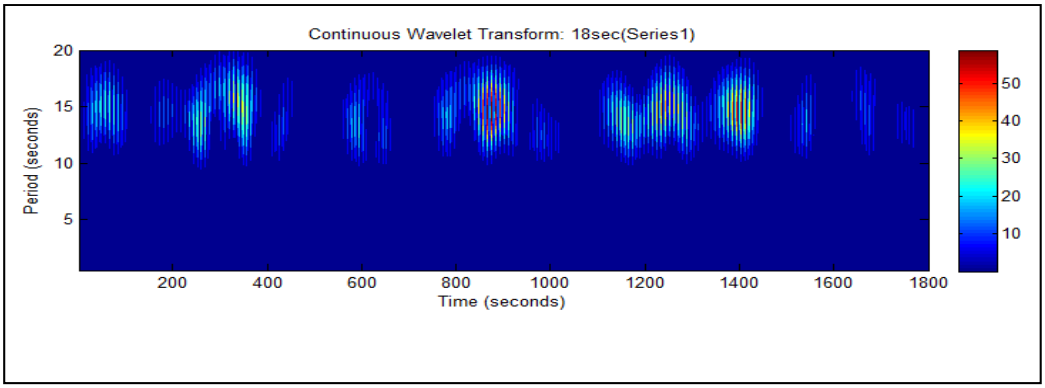

Figure 59: Continuous wavelet transform plots of 18sec(Series1) time series

A comparison of the above plots indicates that the peak energy levels from the 12sec(Series1) and 12sec(Series2) data have very similar distributions in both the frequency and temporal domains. This is to be expected because both series have been derived from the same Power Spectral Density function. However the distributions are very different from those of the 18sec(Series1) data. Again, this is to be expected because the 18sec(Series1) data is derived from a different Power Spectral Density function with a peak period of 18 seconds and a peakedness factor of 5

5.4 Analysis of Saldanha Bay time series

5.4.1 Wave data on the 26th and 28th September 2013

Typical Time Series plots of the surface displacements at Saldanha Bay on the 26 and 28 September 2013 at 09:00 h have been shown in Figures 60 and 61 respectively.

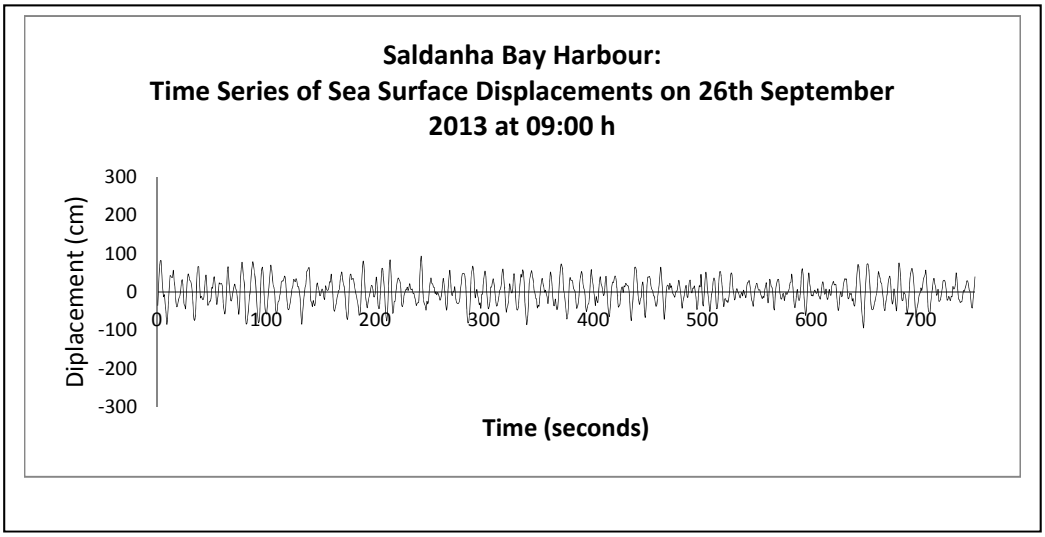

Figure 60: Time series plot at Saldanha Bay on 26th September 2013 at 09:00

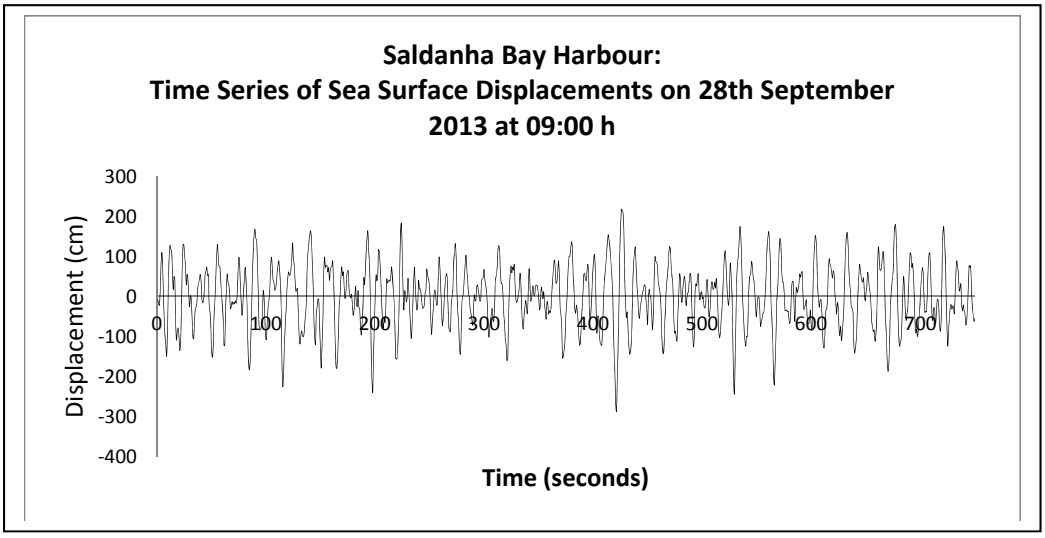

Figure 61: Time series plot at Saldanha Bay on 28 September 2013 at 09:00

The significant wave heights and the peak frequencies (periods) of the sea states existing on the 26 and 28 September 2013 are as detailed in Table 19.

Table 19: Significant wave heights (Hm0) and Peak frequencies (fp)

Saldanha Bay				
Time	26 September 2013		28 September 2013	
	Significant Wave Height (Hm0) m	Peak Frequency (fp) Hz	Significant Wave Height (Hm0) m	Peak Frequency (fp) Hz
06:00 h	1.25	.09	3.02	.07
09:00 h	1.32	.10	3.08	.06
12:00 h	1.26	.09	3.08	.06
15:00 h	1.46	.08	3.0	.09
18:00 h	1.52	.08	3.1	.06
21:00 h	1.62	.08	2.77	.07
Average values	1.40 m	.09	3.01 m	.07
Average Period (sec)		11.1 sec		14.3 sec

The analysis has been based on a 13 minute record of surface displacements.

5.4.2 Time Domain analysis

5.4.2.1 Rescaled Range (R/S) Analysis method

Hurst exponent values for each of the time series records collected from Saldanha Bay harbour at 3 hourly intervals from 06:00h to 21:00h on the 26 September 2013 were determined on the basis of a data sample size of 840 records, made up of 3 segments of 280 records each. The Rescaled Range (R/S) method of analysis was used and a scatter plot of log (R/S) – log (scale) values for a typical segment of data, has been shown in Figure 62.

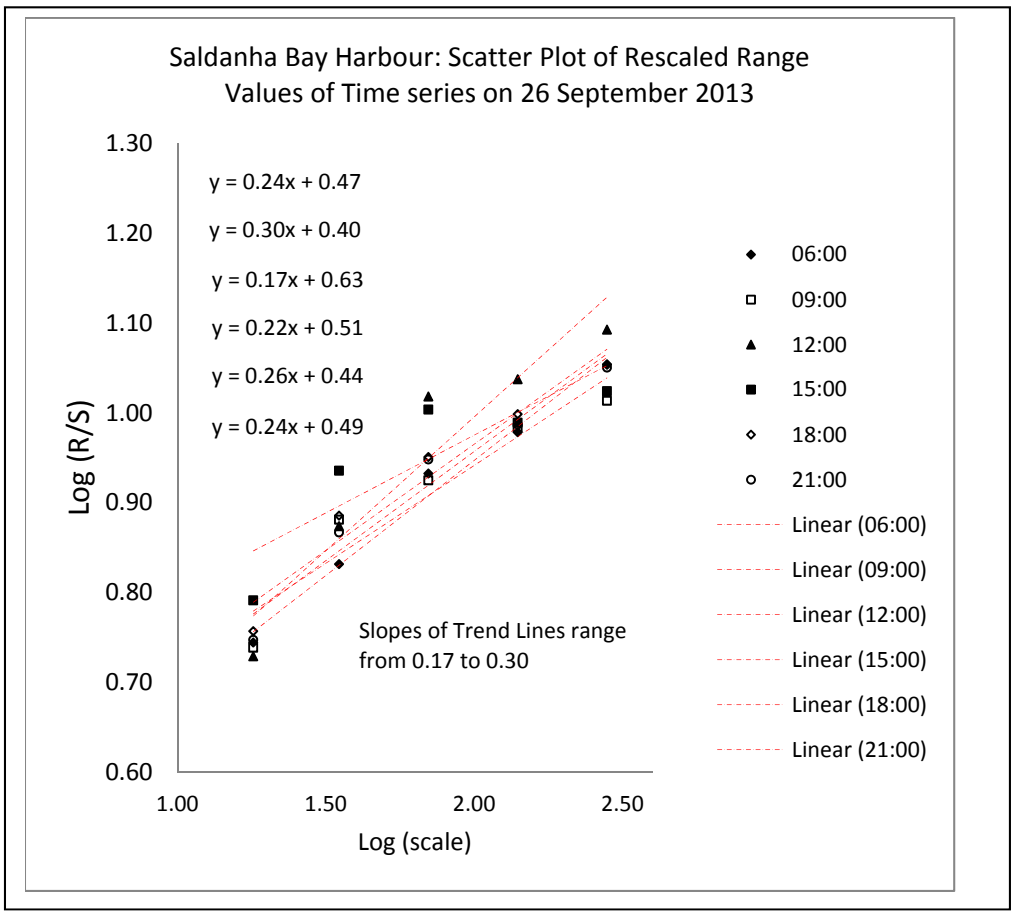

Figure 62**:** Rescaled range values for 280 data segment of data on the 26 September 2013.

As can be seen from the plots in Figure 56, the derived Hurst exponent values based on the slope of the trend lines range from 0.17 to 0.30 with an average value of 0.24. The standard deviation of the exponent values .043 and the coefficient of variation (CoV) is [0.043/.24] x 100 = 16 %. Katsev and L'Heureux (2003) found that short time series with 250 records could be expected to have a (CoV) of 27 per cent. On the basis of this finding one can conclude that the dispersion of exponent values falls within the expected range.

A similar process, to that described above was carried out for the data recorded on the 28 September 2013 and the corresponding scatter plot has been shown in Figure 63.

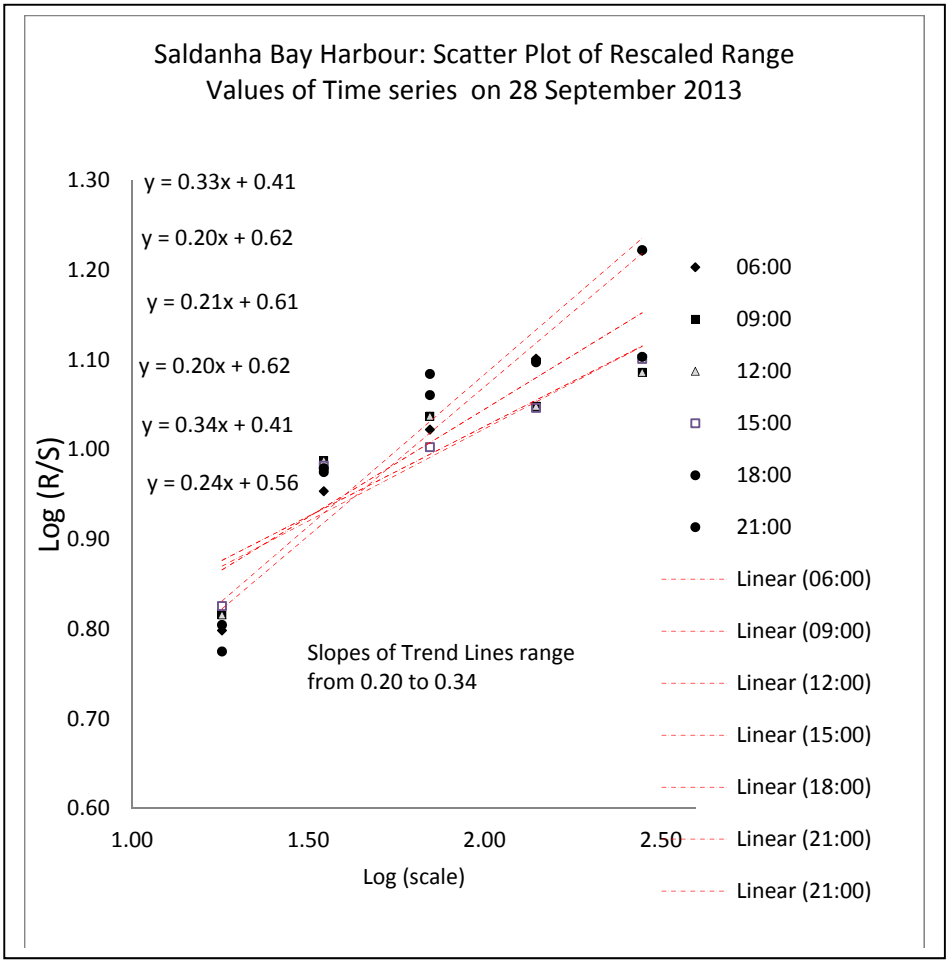

Figure 63: Scatter plot of rescaled range values of 280 data

The derived Hurst exponent values based on the slopes of the trend lines range from 0.20 to 0.34 with an average value of 0.25. The standard deviation of the exponent values .065 and the coefficient of variation (CoV) is [0.065/.25] x 100 = 26 %. The spread of exponent values around the mean is greater on the 28 September than on the 26 September. This could mean that the sea state varied significantly during the period analysis and changed from a globally rougher surface to a generally smoother surface, or vice versa.

The average Hurst exponent value for the 28 September is .29, and while this indicates a 20 per cent shift towards a smoother surface displacement on that day; it must be noted that the sample size of 280 data is relatively small.

The different Hurst exponent values for larger samples comprising 840 records have been shown together with their respective average values in Figure 64, for comparison purposes.

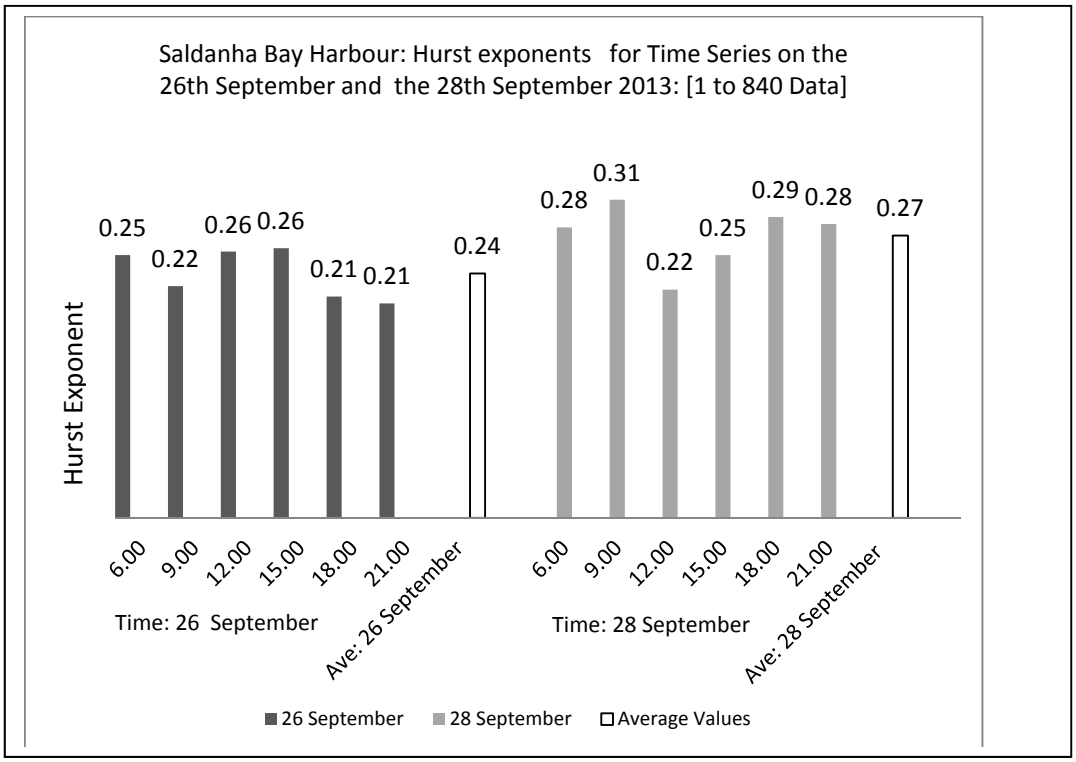

Figure 64: Comparative rescaled range (R/S) values for the Hurst exponent for 26 and 28 September 2013.

The average Hurst exponent values on the 26th and 28th are 0.24 and 0.27, respectively and their coefficients of variation are 10.34 per cent and 11.74 per cent respectively. This indicates that the spread of spread of results are similar, but an analysis indicates that there is no significant difference in the average values of the exponents on the two days. On this basis one can conclude that Hurst exponents derived by the Rescaled Range method of analysis cannot be used to differentiate between non-hazardous and hazardous bound infragravity wave sea states at Saldanha Bay.

The equivalent Fractal Dimension values, D, for the sea surface displacements on the 26 and 28 September are D = 2 - .24 ~ 1.76 and D = 2 - .27 ~1.73, respectively.

5.4.2.2 Multifractal Detrended Fluctuation Analysis (MDFA) method

Two sets of six time series, which represent a 15 hour period of time on the 26 and 28 September 2013 at Saldanha Bay were analysed using the MDFA method. Average singularity spectra, together with the relative frequencies of occurrence of Holder exponents, have been shown in Figure 65.

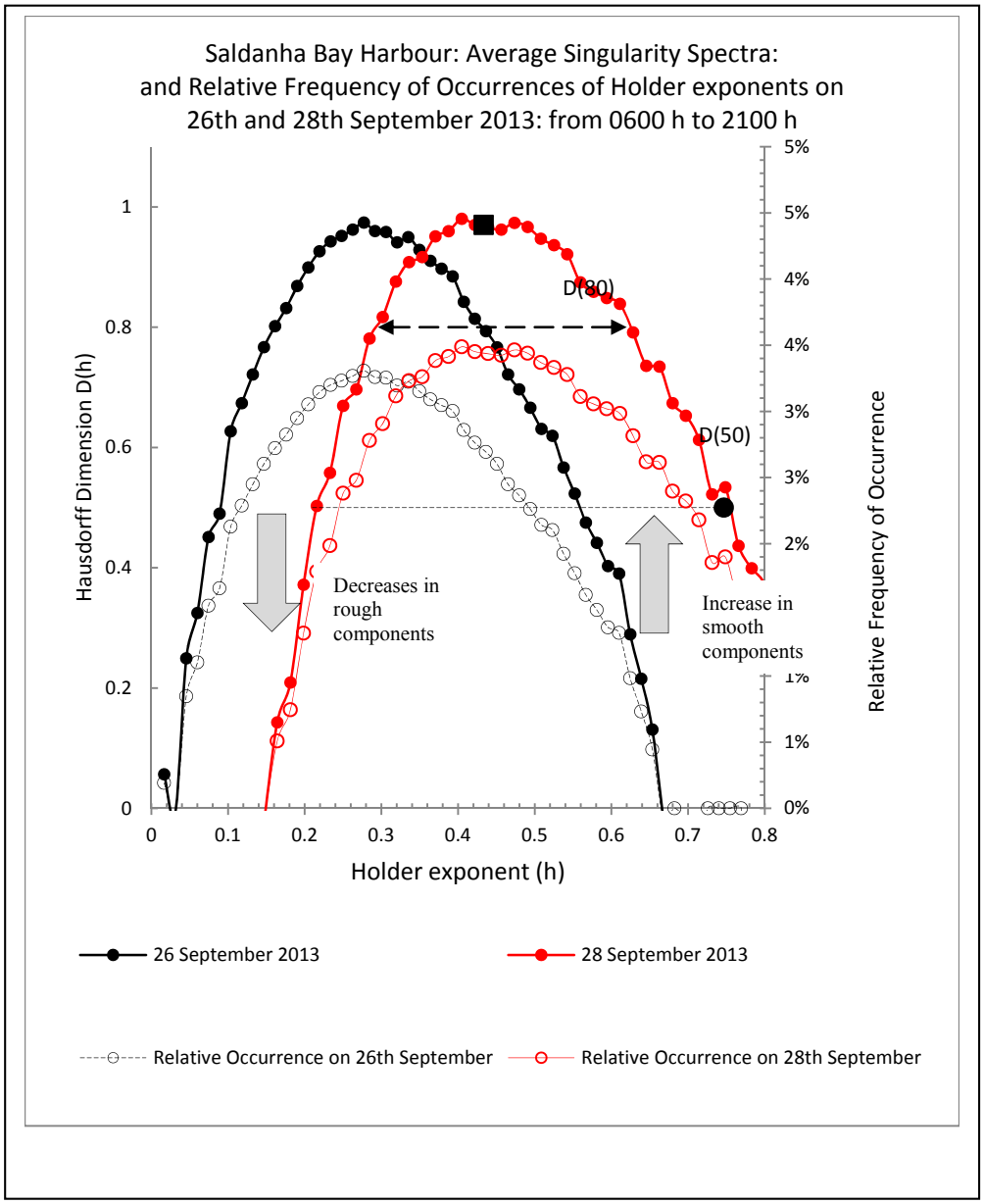

Figure 65: Comparative singularity spectra plots for the 26 and 28 September 2013

The shift in the spectrum representing the sea surface displacements on the 28 September towards higher Holder exponent values can clearly be seen in Figure 61. This shift represents a significant increase in the smoother component of the surface displacements in the time series. The choppier, more irregular, sea surface displacements will of course still be present at this time but the overall sea surface will be some 20 per cent less irregular than what it was on the 26 September due to the increased presence of dominant smoother surface motions.

The maximum Holder exponent value, with a frequency of occurrence of 50 per cent, D(50), has moved from .56 to .76 This represents a significant increase in the smoothness of the series on the 28 September.

The fractal indices that can be determined for the above singularity spectra SS have been set out in Table 20.

Table 20: Summary of fractal indices for singularity spectra on the 26 and 28 September 2013

Fractal Index	26 September 2013	28 September 2013	Remarks
h(p)	0.27	0.44	Smoother, more regular surface geometry on the 28th
D(80)	0.43 - .16 = 0.27	0.62 – 0.30 = 0.32	Wider range of singularities on the 28th
D(50)max.	0.56	0.76	Smoother, more regular surface geometry on the 28th

The shift of the fractal indices, h(p) and D(50) max, to larger values indicates smoother surface displacements on the 28 September.

Holder exponent probability of non-exceedance curves for the two days have been shown in Figure 66.

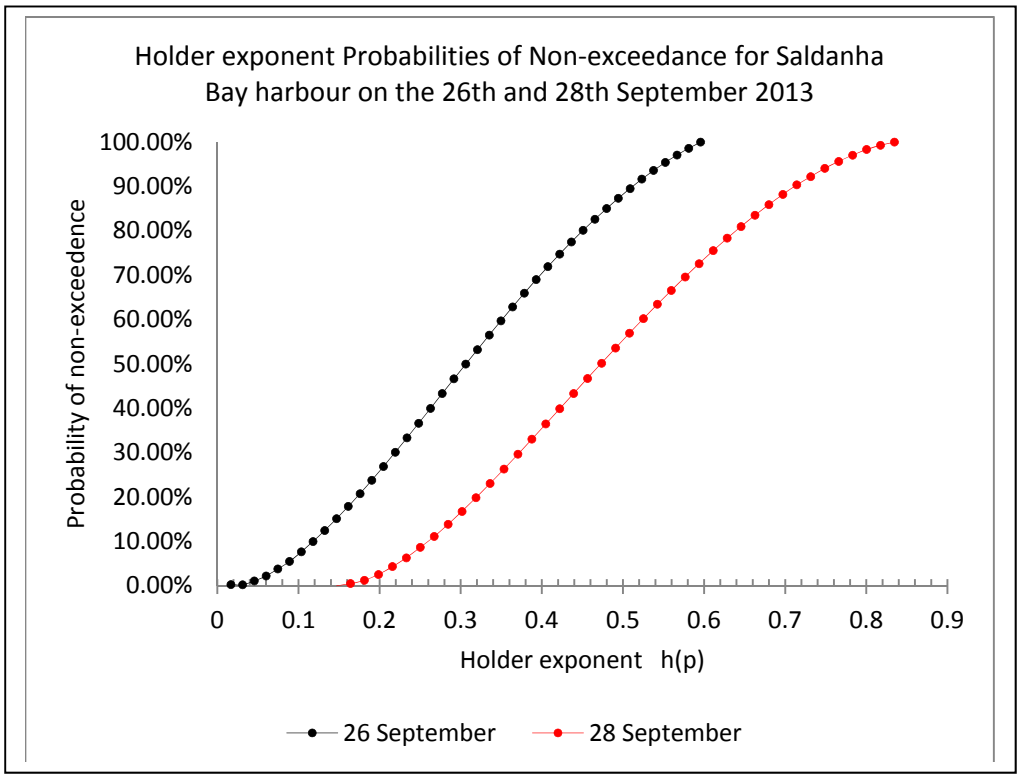

Figure 66: Holder exponent probabilities of non-exceedance for Saldanha Bay on the 26 and 28 September 2013.

5.4.3 Frequency Domain analysis

5.4.3.1 Power Spectral Density (PSD) Analysis in the Fourier domain

Envelope plots of the PSD spectra at Saldanha bay for the period between 06:00h and 21:00h on the 26 and 28 September 2013 have been shown in Figure 67.

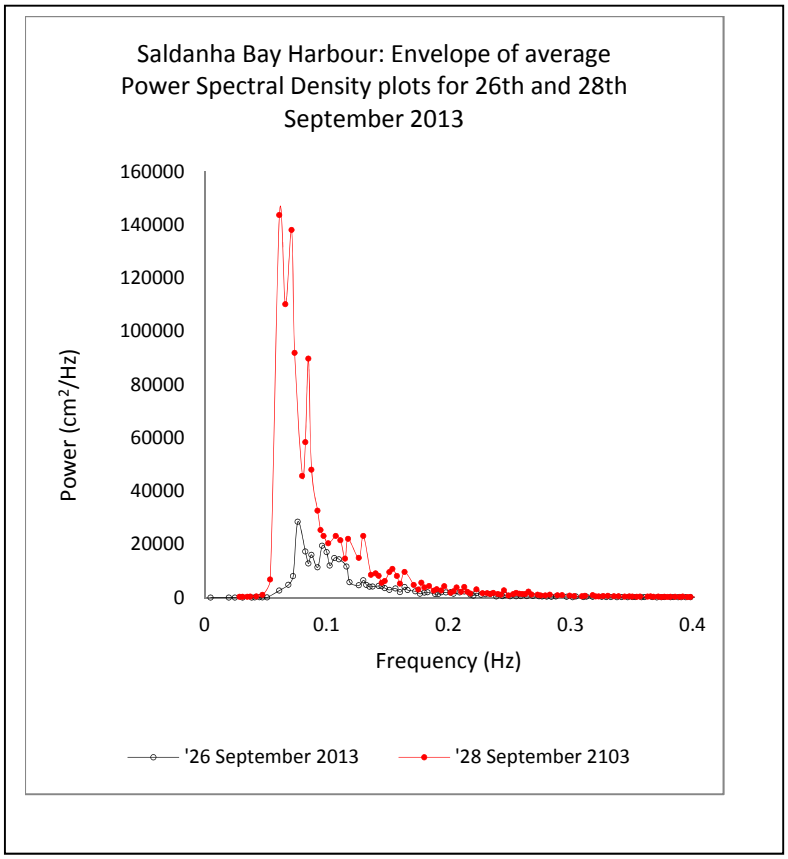

Figure 67: Power spectral density envelopes in the Fourier domain for time series of 26 and 28 September 2013.

A shift in the spectral envelopes can clearly be seen in Figure 60. The power is significantly increased, and the peak frequency is significantly reduced on the 28th, during hazardous BIW conditions. The shift in peak period is in line with the observed changes in fractal geometry.

Logarithmic plots of the PSD spectrum of the time series recorded at Saldanha Bay at 9:00h on the 26 and 28 September 2013 have been shown in Figure 68, together with a plot of the $1/f^{\beta}$ functions.

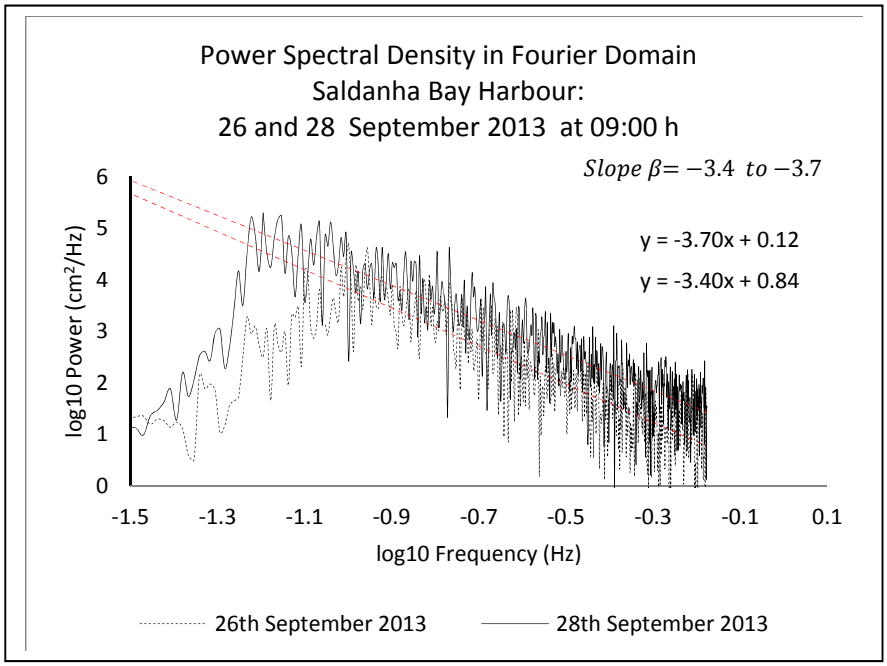

Figure 68: Log-log plot of power spectral density plots for time series of 26 and 28 September 2013

The slope of the $^{1}/_{f^{\beta}}$ plot on the two days is similar, with a slope value of

$\beta = 3.4\ to\ 3.7$ indicating the same degree of short-term correlation.

5.4.3.2 PSD analysis in the Wavelet Domain.

PSD functions in the wavelet domain for the same time series referred to in 4.3.1 have been shown in Figure 69.

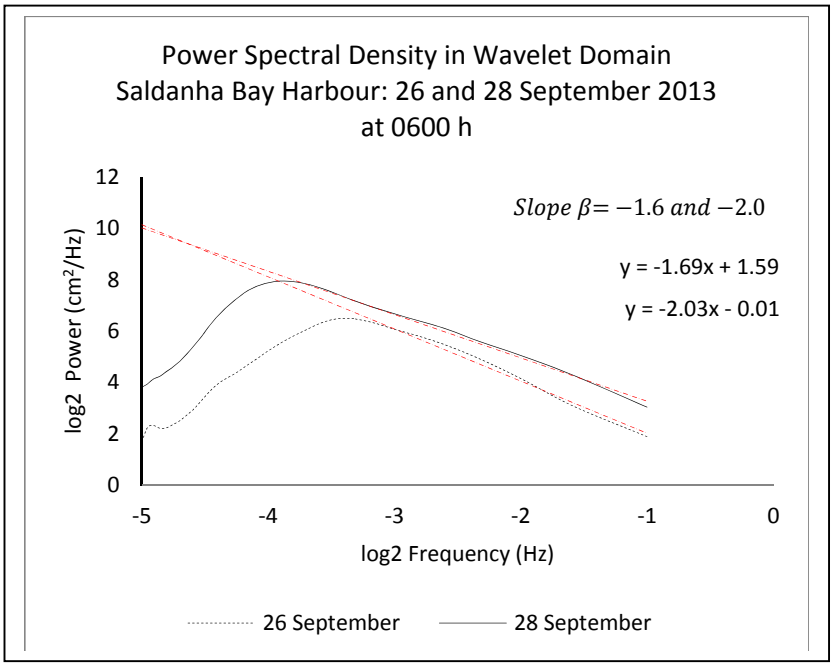

Figure 69: PSD plots of the time series in the wavelet domain.

The $1/f^{\beta}$ functions for both PSD's are similar with lower values of β = -1.6 and –2.0 in the Wavelet Domain, indicating a higher degree of correlation. These lower values could be due to either the fact that the wavelet analysis is based on local and not overall characteristics in the time series, or else possible differences in the Fourier and wavelet transform coefficients.

5.4.3.3 Wavelet Transform Modulus Maxima (WTMM) analysis of time series

Continuous Wavelet Transform (CWT) plots of the time series at Saldanha Bay on the 26 and 28 September 2013 at 06:00, 09:00, 12:00, 15:00, 16:00, 18:00 and 21:00 hrs are shown in Figures 70 and 71, together with corresponding with Modulus Maxima plots.

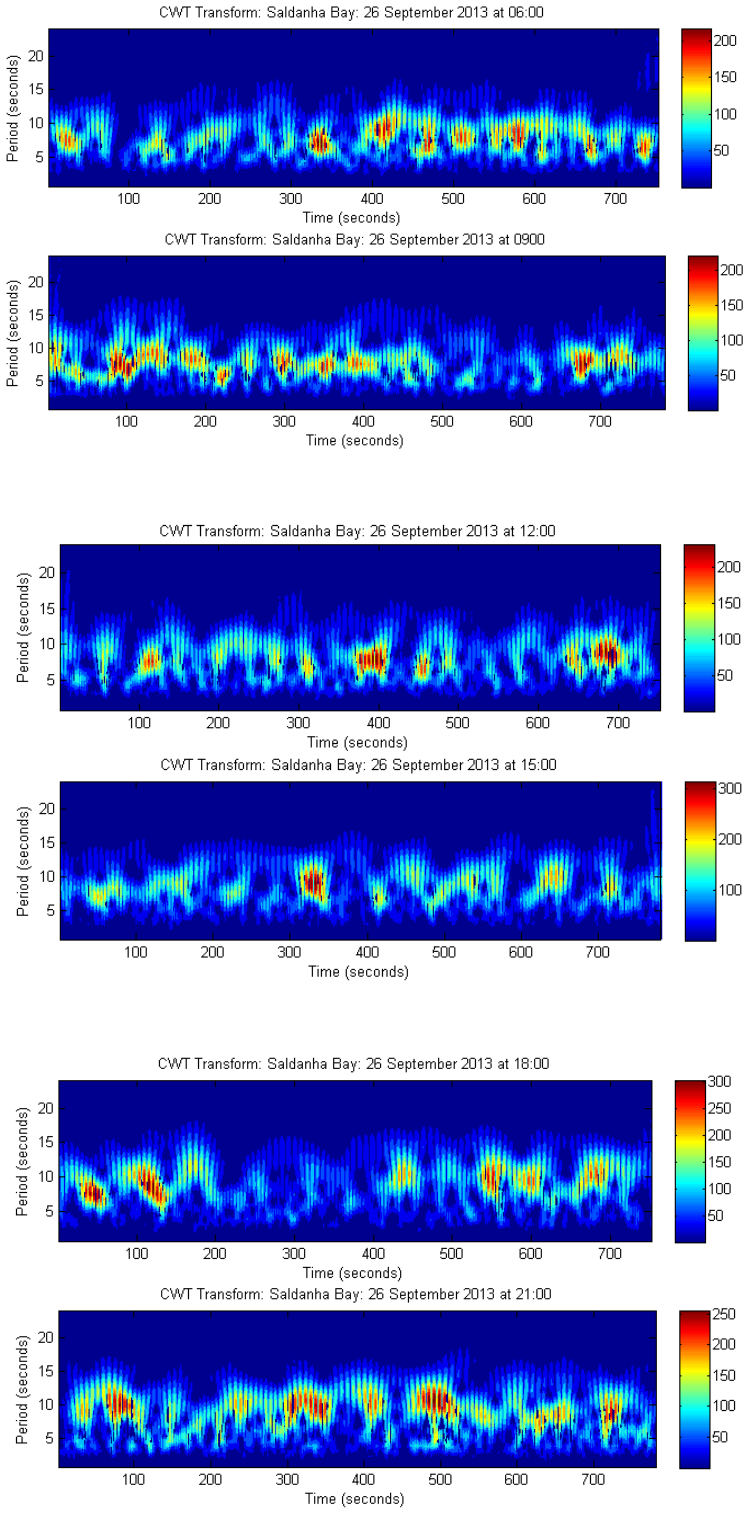

Figure 70: Continuous wavelet transform plots of time series on the 26 September 2013

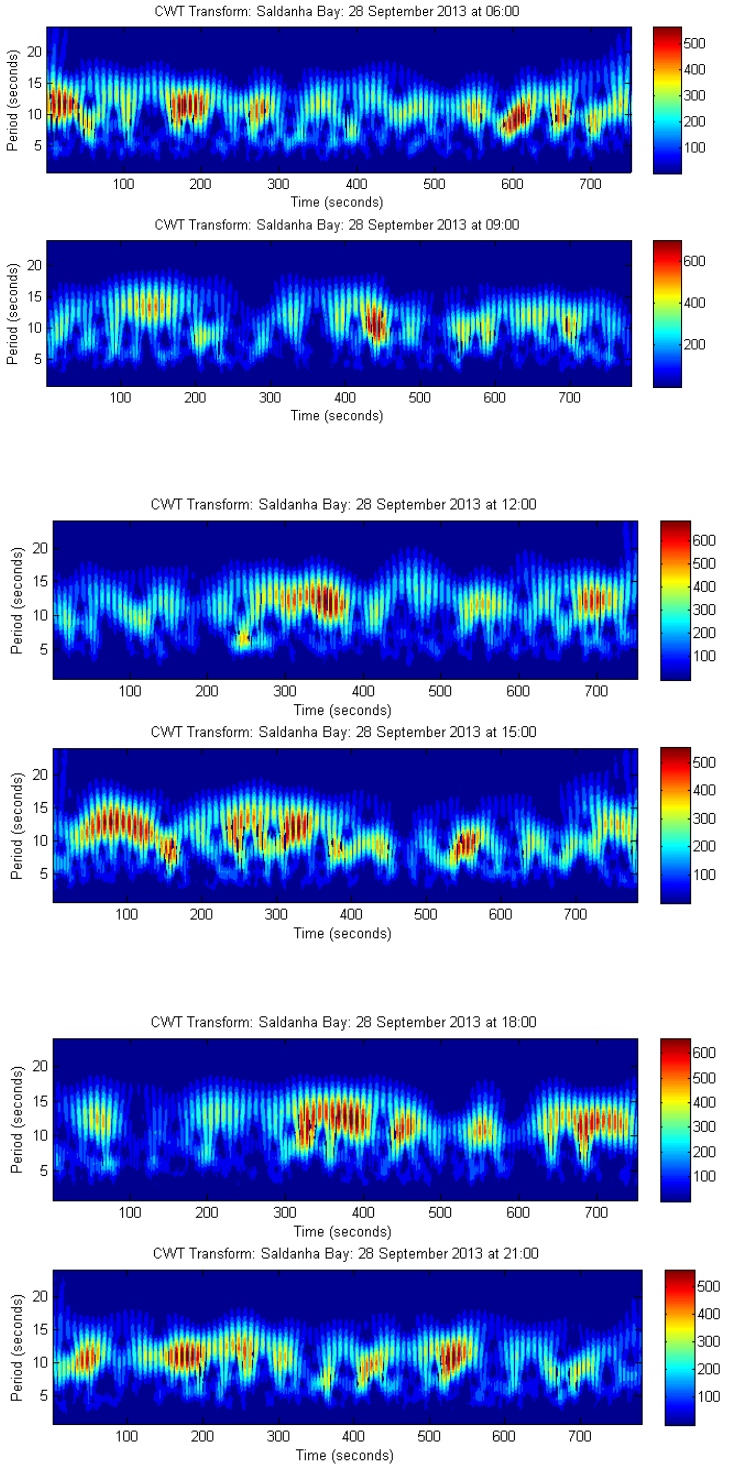

Figure 71: Continuous wavelet transform plots of time series on the 26 September 2013

Continuous Wavelet Transform (CWT) plots of the time series at Saldanha Bay at 09:00 hrs on the 26 and 28 September 2013 have been shown in Figures 65 and 66, together with corresponding with Modulus Maxima plots.

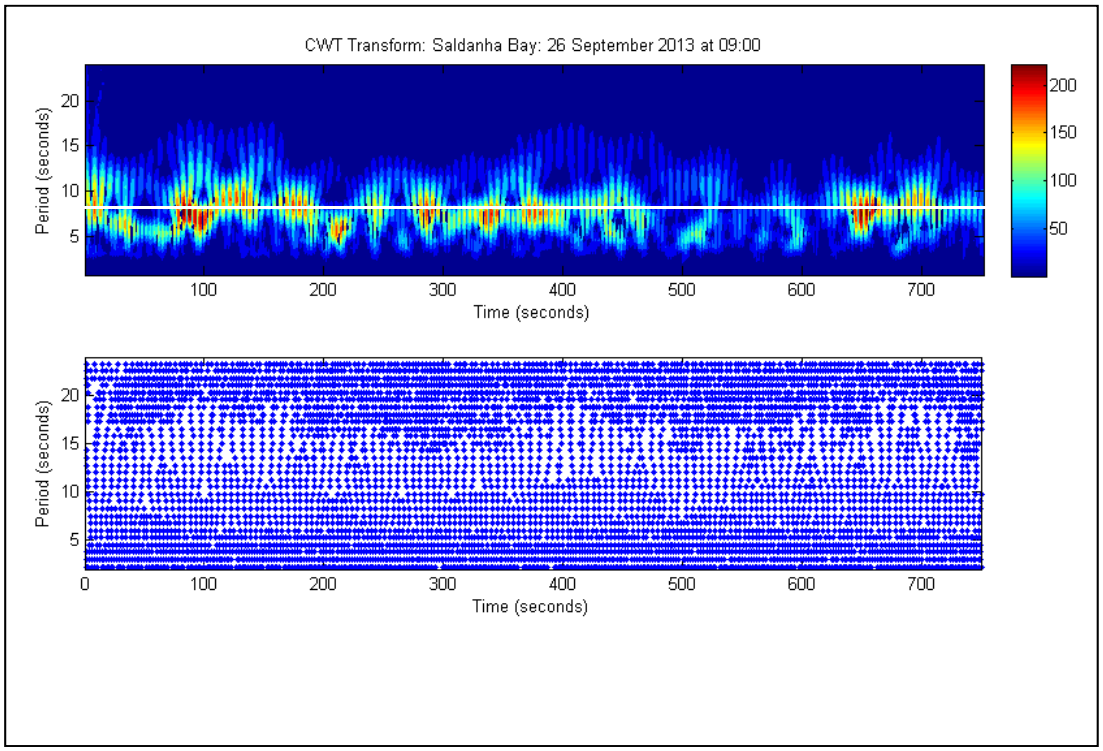

Figure 72: Continuous wavelet transform and modulus maxima chains for time series recorded at 09:00 on the 26 September 2013

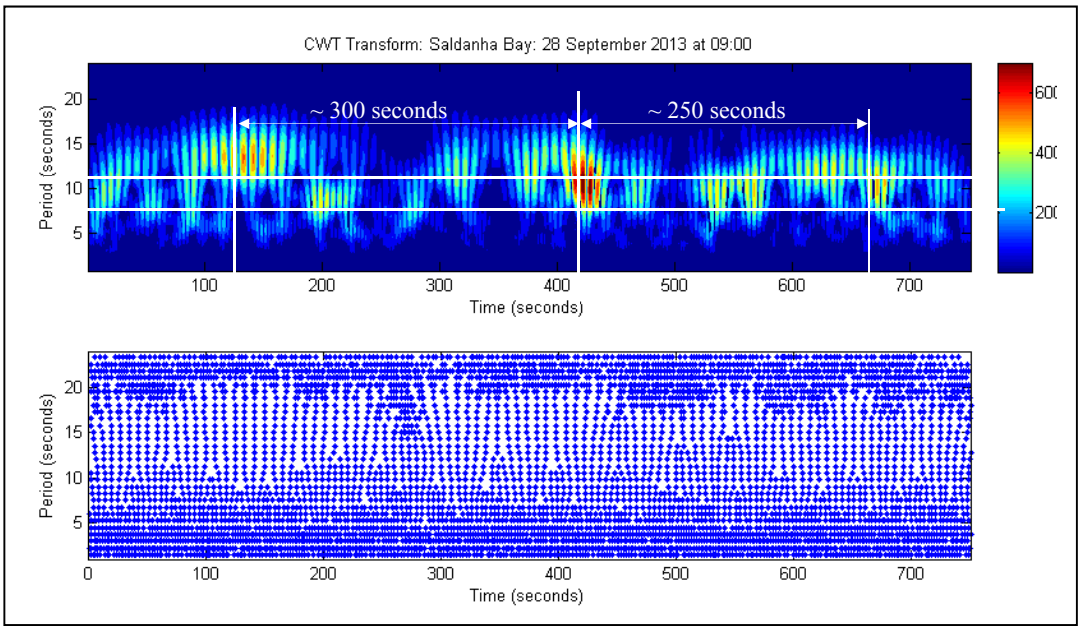

Figure 73: Continuous wavelet transform and modulus maxima chains for time series recorded at 09:00 on the 28 September 2013.

A comparison of the above two CWT plots, clearly shows that:

- The peak energies in the time series on the 26th (shown marked with a horizontal white line in figure 65) occur at periods in the region of 8 seconds, with an equivalent frequency of 0.13 Hz

- The peak energies in the time series on the 28th (shown marked with horizontal white lines in figure 66) occur at periods of 10 to 14 seconds, with equivalent frequencies of 0.1 and.07 Hz, respectively)

- The peak wave energies on the 26th are more numerous and more closely spaced that those on the 28th. [Note that the peak energy periods on the two days are very different. This difference can clearly be seen on the envelope plot of PSD's in Figure 60.]
- The regular occurrences of peak energy groups in the time series indicates a frequency of occurrence of wave train forcing mechanisms which would

constitute periodic wave loading on moored vessels. Mansard and Pratte (1982) has suggested that irregular wave forcing on moored vessels would vary with the wave envelope, but, as can be seen in the CWT plot of the wave train on the 28 September, the period of peak energy occurrence could be significantly greater than the period of occurrence of wave groups in the same wave train. Typical average temporal periods of energy concentrations in the wave train on the 28th range from 55 seconds to peak values (as shown by vertical white lines on figure 63) in the region of 275 seconds. Similar energy concentrations and peak energy occurrences over longer durations of time as shown in the period average plots in figure 94.

The configuration of the modulus maxima chains in the CWT plots has not been clearly defined in Figures 62 and 63, due to the long lengths of the series (1000 data points). The first section of the CWT plot in Figure 63, comprising 180 seconds, has been redrawn and is shown in Figure 74 so that details of the singularity structure of the wave train can be more clearly seen.

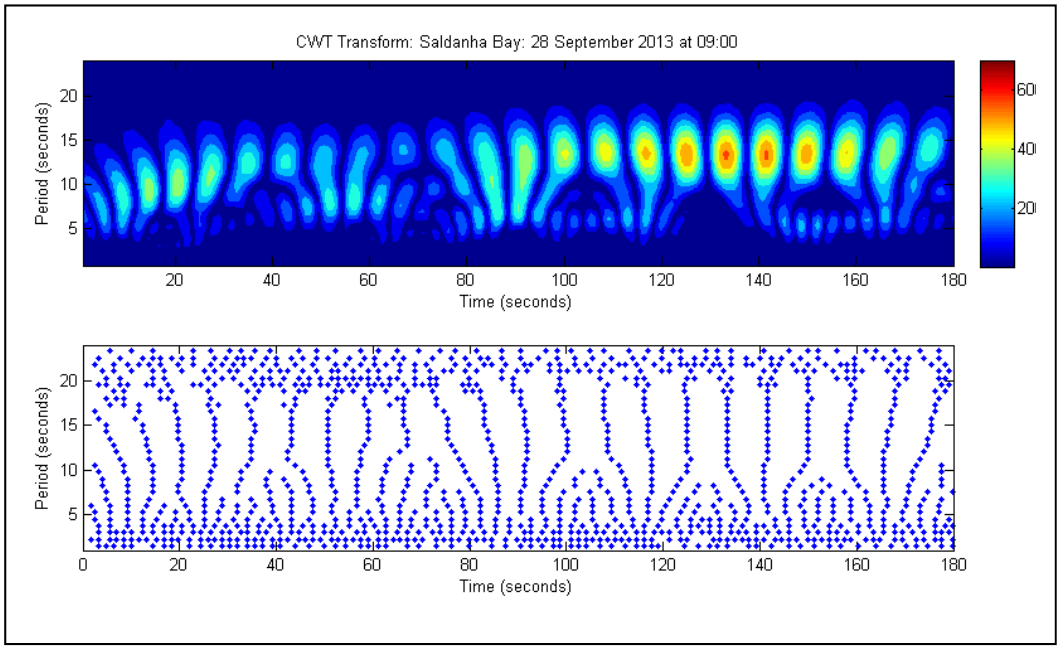

Figure 74: Continuous wavelet transforms and modulus maxima chains for 180 seconds of time series recorded at 9:00 on the 28 September 2013

The above figure clearly shows how the chains merge and become much more concentrated at the lower scales (higher frequencies), indicating the nature of the fractal structure and how the number of peaks, representing local singularities and Holder exponents, varies with scale.

One of the main advantages of the WTMM method of analysis, from the point of view of fractal analysis, is that redundancies, which naturally occur in the continuous wavelet transform, are filtered out by the method. The WTMM process only captures the maximum values of the CWT transform and in this way it defines the layout of the singularities in the time series.

The Singularity Power Spectra envelopes, for wave periods of 5, 10, 15 and 20 seconds, on 28 September at 09:00 hrs have been shown in Figure 68. It can clearly be seen from envelope plots that the temporal periods of peak power range from 50 to 300 seconds.

The spectral envelopes in figure 75 indicate the various energy concentrations occurring in the long waves present in the wave train. The envelope representing short wave periods in the region of 5 seconds is very similar to the time series envelope, but the energy in this spectrum is relatively low. The higher peaks in the long waves occur at short wave periods of 10 to 15 seconds.

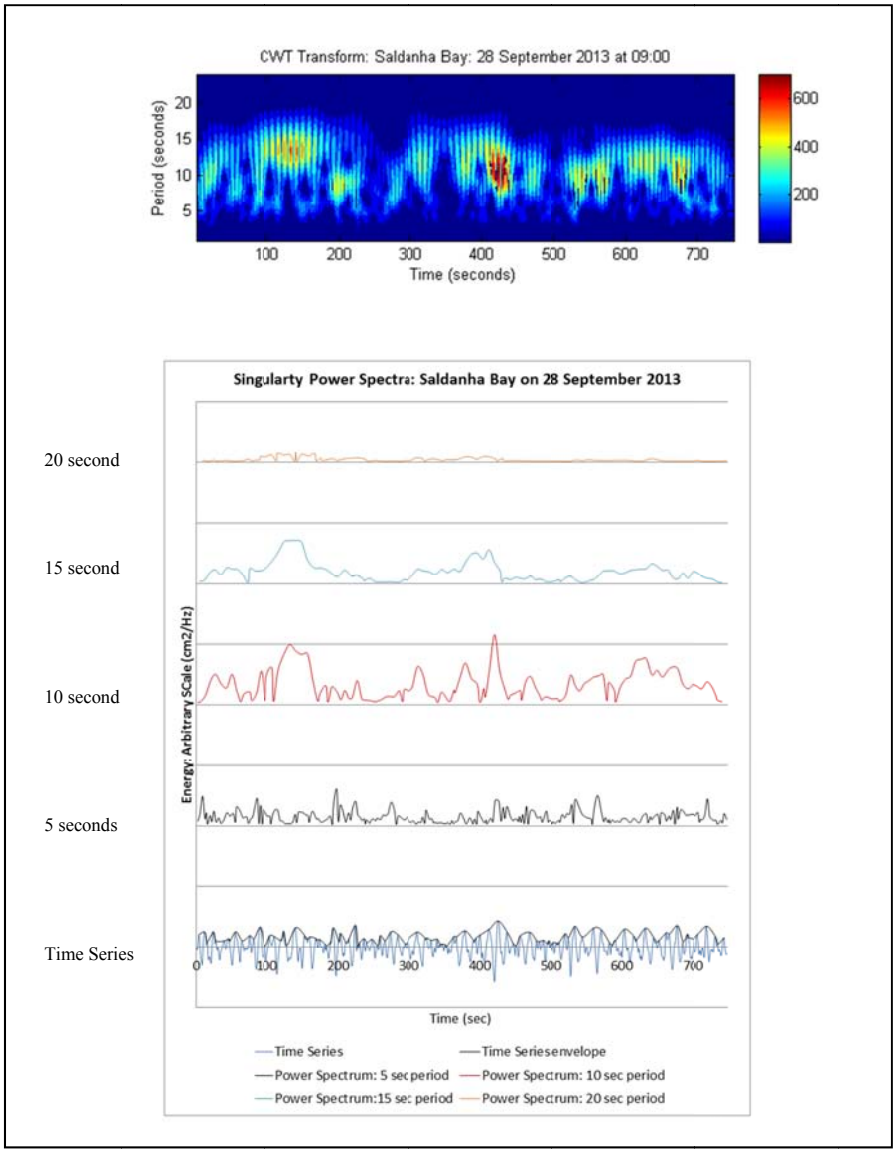

Figure 75: The singularity power spectral envelopes for the time series on 28 September 2013

5.5 Analysis of Ngqura Harbour time series

5.5.1 Wave data on the 6 /7 and 8 August 2012

Typical time Series data recorded by the waverider buoy at Ngqura on the 6/7 and 8 August 2012 have been shown in Figures 76 and 77.

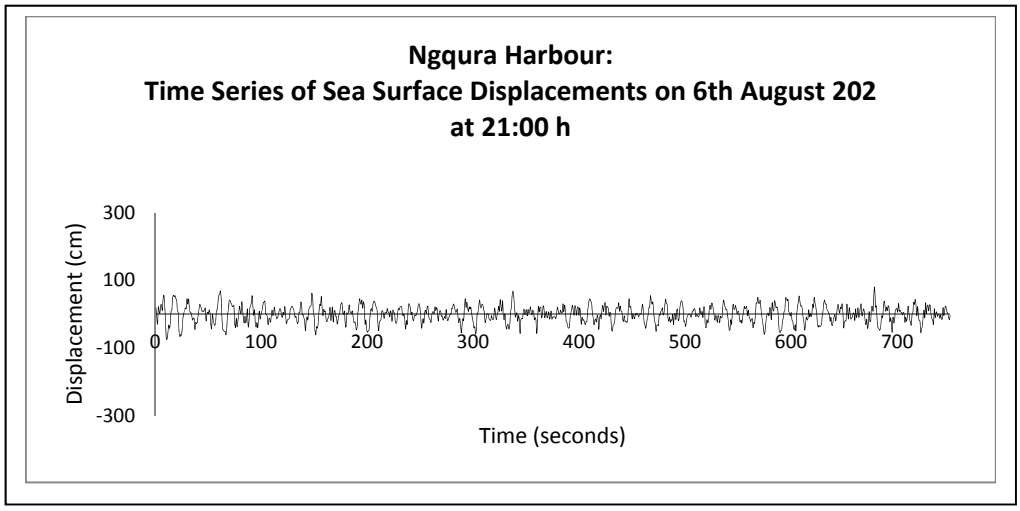

Figure 76: Time series of sea surface displacements at Ngqura Harbour on 6 August 2012 and 10:30 h

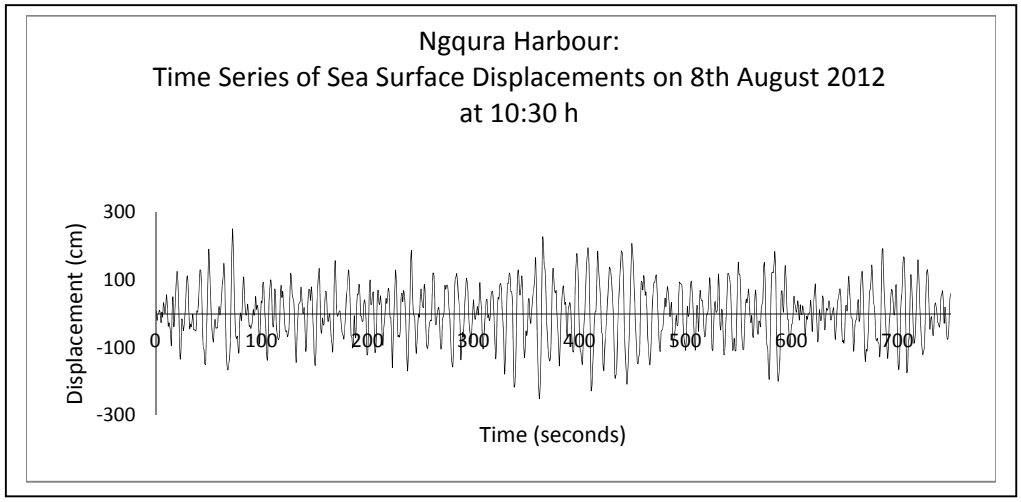

Figure 77: Time series of sea surface displacements at Ngqura Harbour on 8 August 2012 and 10:30 h.

The significant wave heights and the peak frequencies (periods) of the sea states existing on the 6th and 7th as well as the 8 August 2012 are as detailed in Table 21.

Table 21: Significant wave heights (Hm0) and peak frequencies (fp)

Ngqura					
6/7 August 2012			8 August 2012		
Time	**Significant Wave Height (Hmo)** m	**Peak Frequency (fp)** Hz	**Time**	**Significant Wave Height (Hmo)** m	**Peak Frequency (fp)** Hz
1900	1.13	0.08	0500	3.44	.10
2100	0.97	0.07	1030	3.24	.10
2300	1.03	0.07	1500	3.49	.10
0100	1.27	0.08	1700	3.72	.10
0300	1.10	0.09	1900	3.29	.10
0500	1.51	0.07	2100	3.55	.10
Average	1.17	0.08		3.46m	0.10
Average Period (Tp)		12.5 sec			10.0 sec

5.5.2 Time Domain analysis

5.5.2.1 Rescaled Range (R/S) Analysis method

R/S analyses, similar to those which were carried at Saldanha Bay, were carried out for the time series data that was collected at Ngqura harbour on both the 6th and 7th as well as the 8 August 2012.

Scatter and linear regression plots, which were derived from a typical 280 data segment of the analysed time series, during both of the periods the have been shown in Figures 78 and 79.

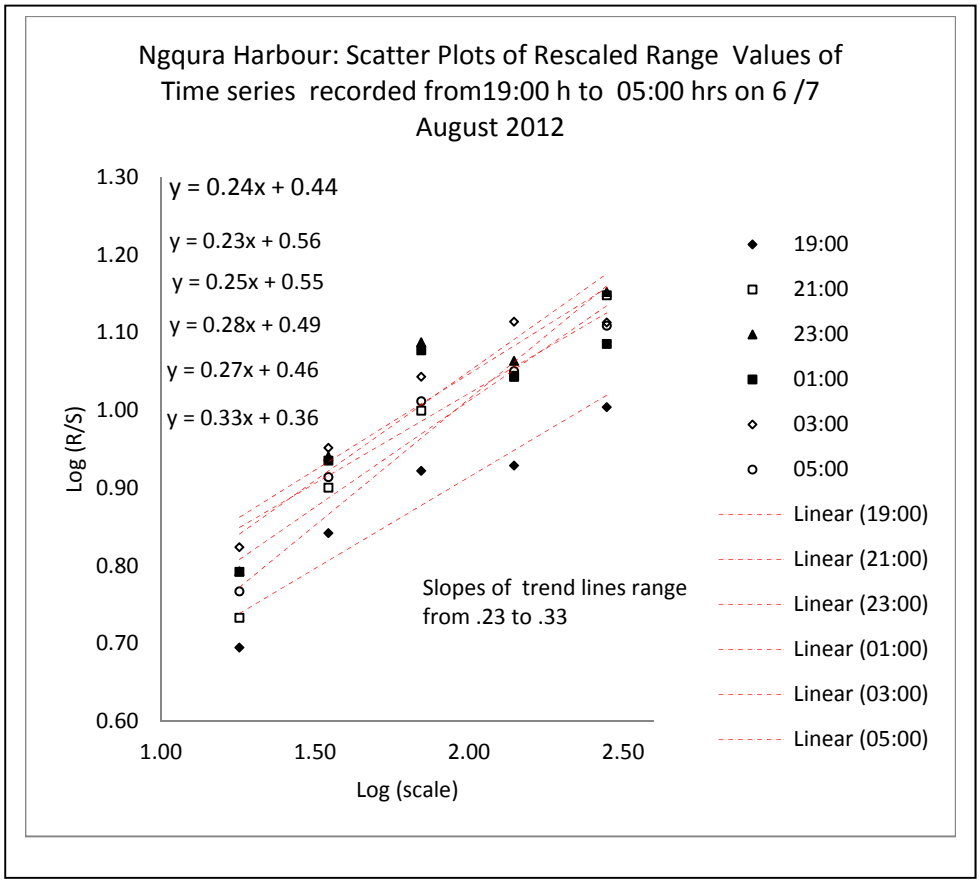

Figure 78: Scatter plot of rescaled range values: 6 and 7 August 2012.

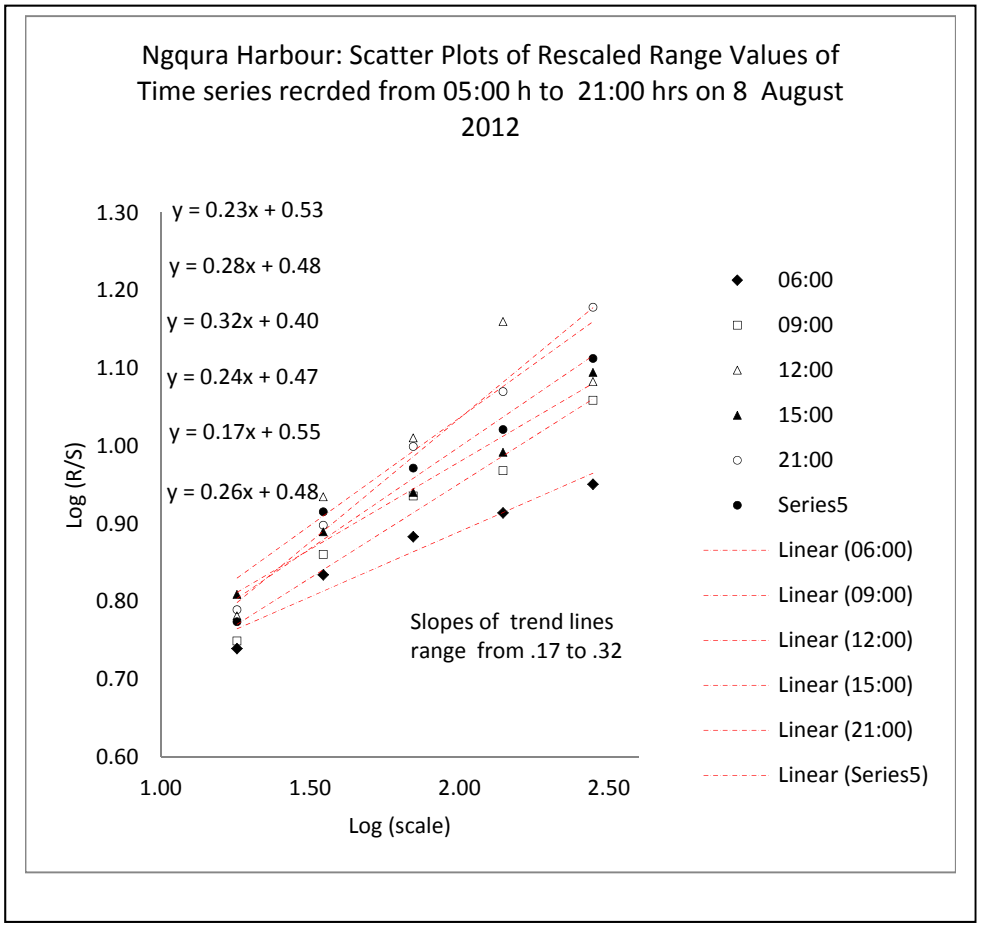

Figure 79: Scatter plot of rescaled range values: 8 August 2012.

The Hurst exponent values for the two periods 6/7th August and 8 August range from .23 to point .33 and from .17 to .32 respectively.

A comparative bar chart plot of the average Hurst exponents of the 840 records selected from the typical time series data recorded of the 6th and 7th as well as the 8 August 2012 has been shown in Figure 80 for comparison purposes.

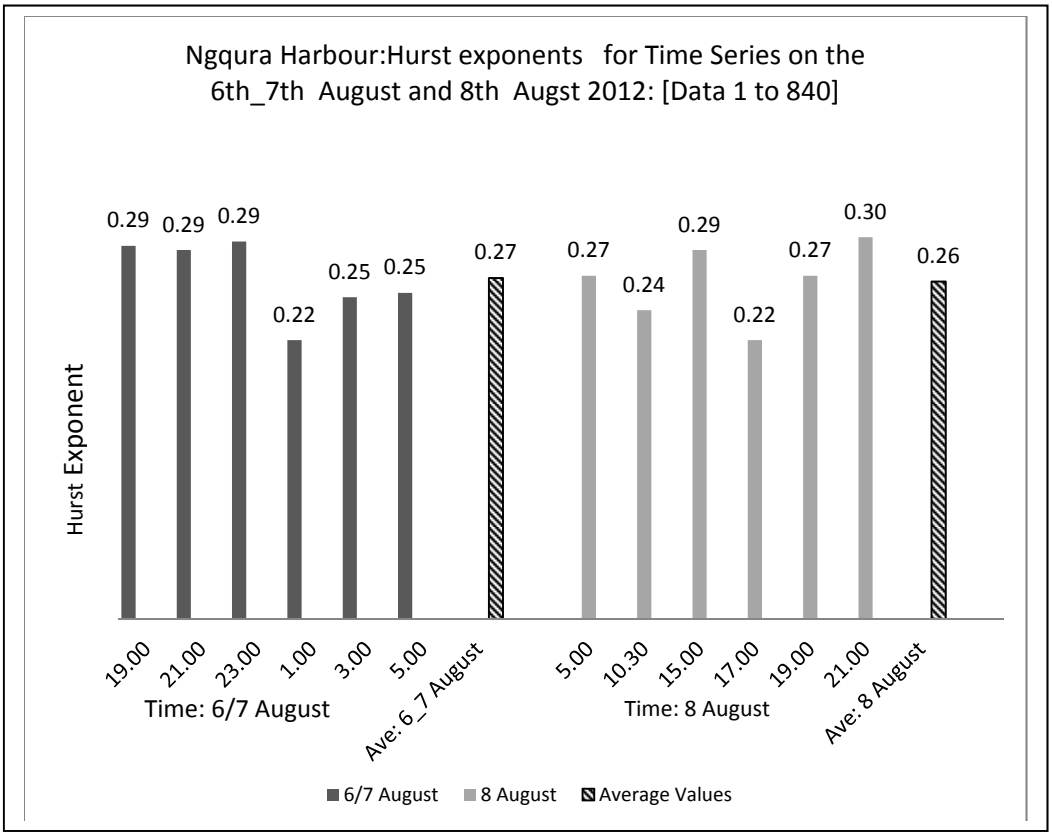

Figure 80: Comparative plots of average R/S values for 6 and 8 August 2012.

The average Holder exponents of the 6/7 and 8 August 212 are 0.27 and 0.26 respectively and the ranges of exponents are 0.22 - 0.29 = .07 and 0.22 to 0.30 = 0.08 respectively. There is no significant difference in the average values of the exponents for the two periods on this basis one can conclude that Hurst exponents derived by the Rescaled Range method of analysis cannot be used to differentiate between non-hazardous and hazardous bound infragravity wave sea states at Ngqura harbour.

5.5.2.2 Multifractal Detrended Fluctuation Analysis method

MDFA analyses, similar to those conducted for Saldanha Bay, were carried out for the time series data that was collected at Ngqura harbour on the 6 /7 August and 8 August 2012.

Singularity Spectra, which were derived from the abovementioned analyses, have been shown together in Figures 81, and the derived fractal indices have been shown in table 22.

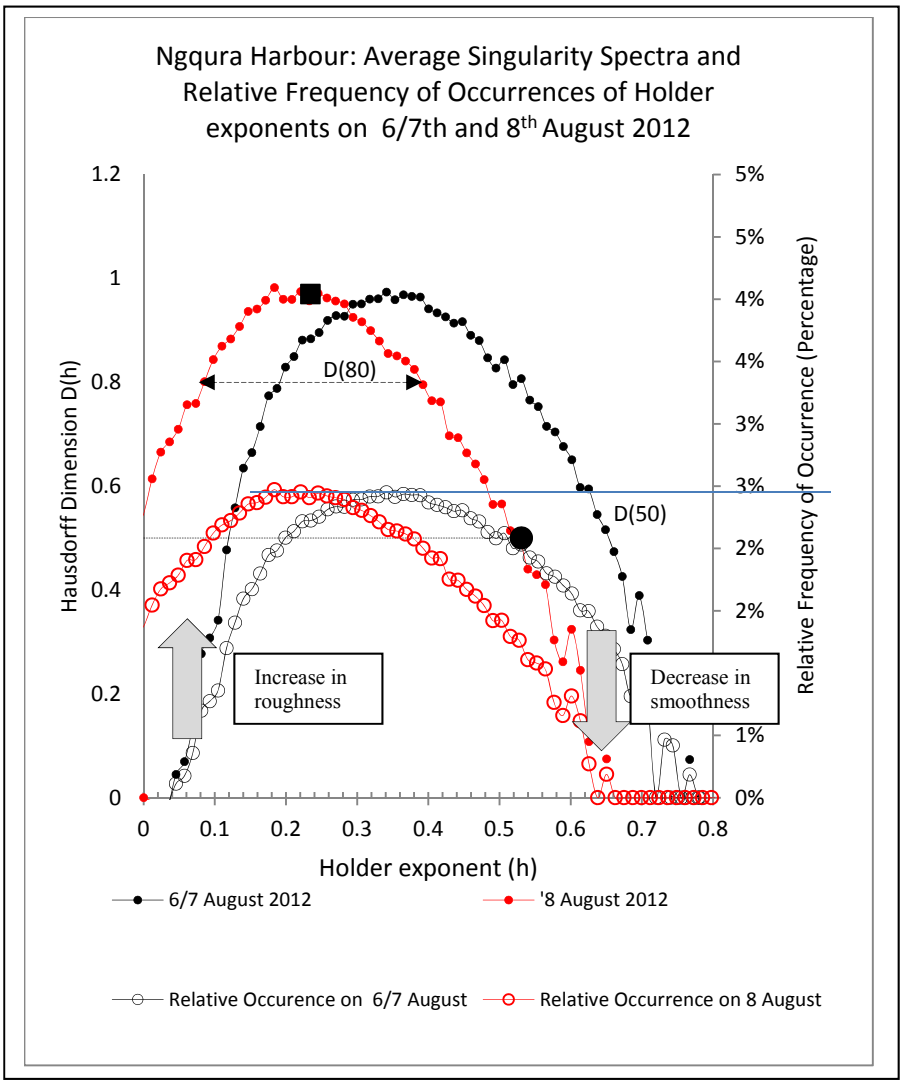

Figure 81: Comparative singularity spectra plots for 6/7 August and 8 August 2012

The peak Holder exponent, or global Hurst exponent, is present in the both of the above series for 2.5 per cent of the time.

The values of the different fractal indices, as derived from the singularity spectrum, are summarised in Table 22.

Table 22: Summary of fractal indices for singularity spectra on the 6 /7 August and the 8 August 2012.

Fractal Index	6 August 2012	8 August 2012	Remarks
h(p)	0.35	0.23	More irregular surface on the 8th
D(80)	.52 - .18 = 0.34	.39 - .07 = .32	Same range of singularities.
D(50)max.	0.65	0.53	More irregular surface on the 8th

The sea surface displacement profile during a hazardous BIW sea state is rougher, or more irregular, than during a non-hazardous sea state.

5.5.3 Frequency Domain analysis

5.5.3.1 Power spectral density (PSD) analyses in the Fourier domain

Spectral analyses of the time series that were recorded at Ngqura harbour on the 6/7 and 8 August 2012 were carried out, and envelope plots of the average spectra have been shown in Figure 82.

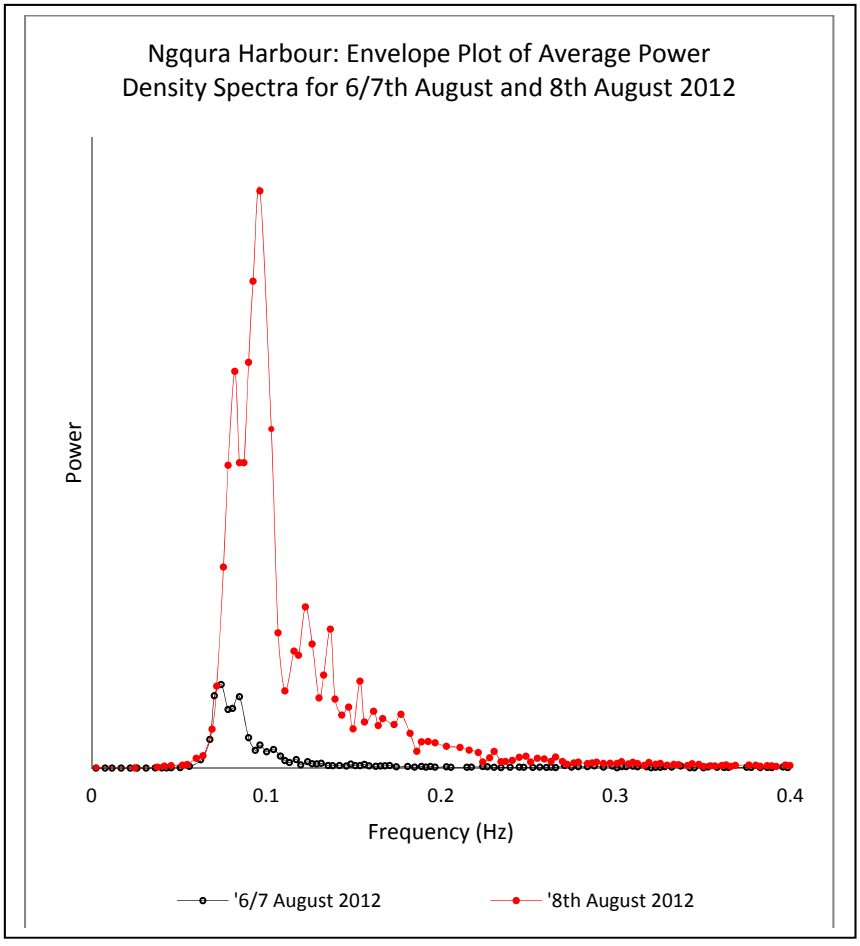

Figure 82: Power spectral density plots for time series of 6/7 and 8 August 2012

A shift in the spectral envelopes can clearly be seen in Figure 70, as both the power and the peak frequency of the wave trains have increased on the 8th, during hazardous BIW conditions.

Logarithmic plots of the PSD spectra of the time series recorded at Ngqura harbour on the 6 and 8 August 2012, at 21:00h have been shown in Figure 83, together with a plot of the $^{1}/_{f^{\beta}}$ function.

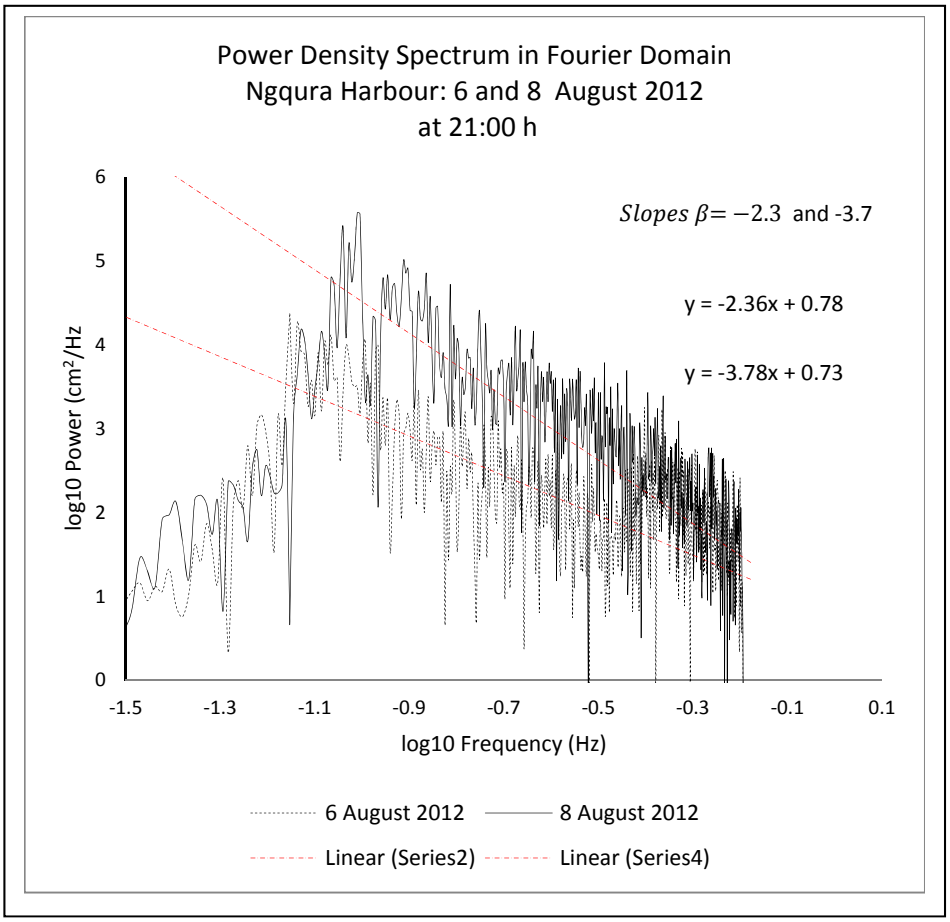

Figure 83: Log-log plot of power spectral density plots for time series of 6 and 8 August 2012

The slope of the $^{1}/_{f^{\beta}}$ plot on the two days is similar, with slopes of $\beta = -2.4\ and -3.0$ during non-hazardous and hazardous sea states, respectively. These spectral exponent values indicate that the persistence or correlation of a hazardous sea state is less than that of a non-hazardous sea state.

5.5.3.2 Power Spectral Density (PSD) Analyses in the wavelet domain

Continuous Wavelet Transform analyses of the time series recorded at Ngqura harbour on the 6 and 8 August 2012, at 21:00h were carried out and their global PSD plots have been shown in Figure 84, together with a plot of the $^{1}/_{f^{\beta}}$ function.

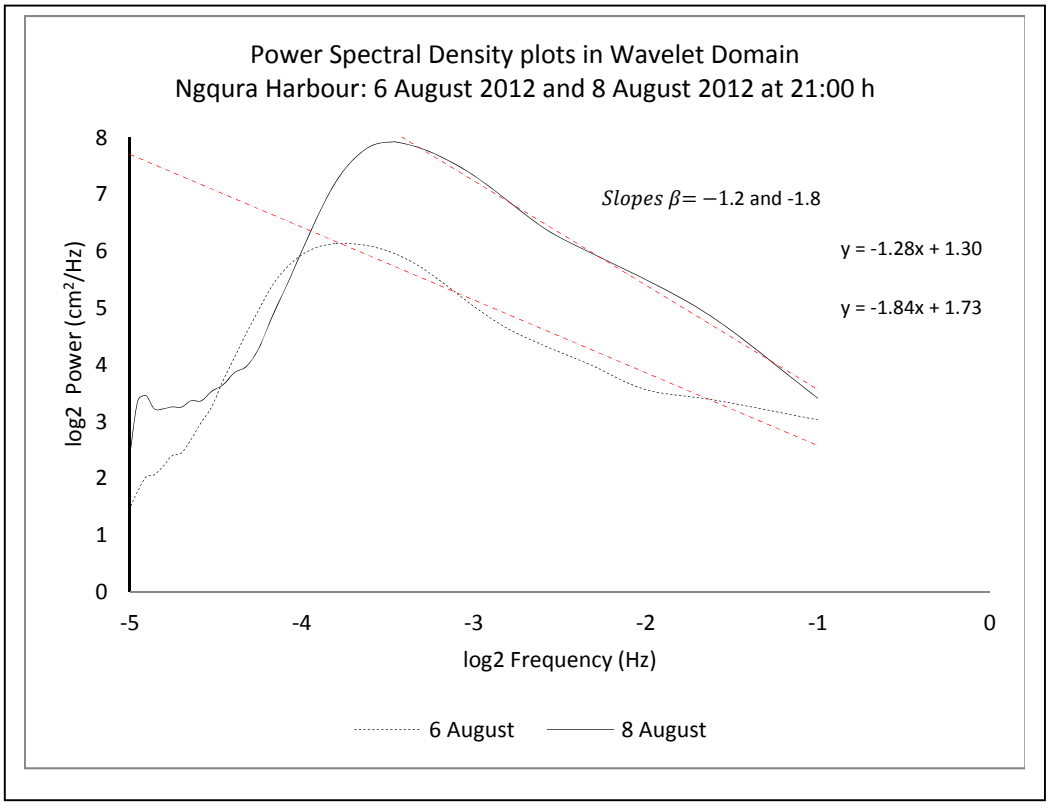

Figure 84: Wavelet scaling exponent

The $^{1}/_{f^{\beta}}$ functions for both PSD's in the wavelet domain are lower than those in Fourier domain. As noted for the Saldanha Bay, the lower values could be due to either the fact that the wavelet analysis is based on local and not overall characteristics in the time series, or else possible differences in the Fourier and wavelet transform coefficients.

5.5.3.3 Wavelet transform modulus maxima (WTMM) analysis

Continuous Wavelet Transform plots of the time series at Ngqura harbour on the 6 August 2012 at 21:00, 23:00, 03:00, and 05:00and the 8 August 2012 at 05:00, 10:30 15:00, 17:00, 19:00 and 21:00h have been shown in Figures 85 and 86 respectively.

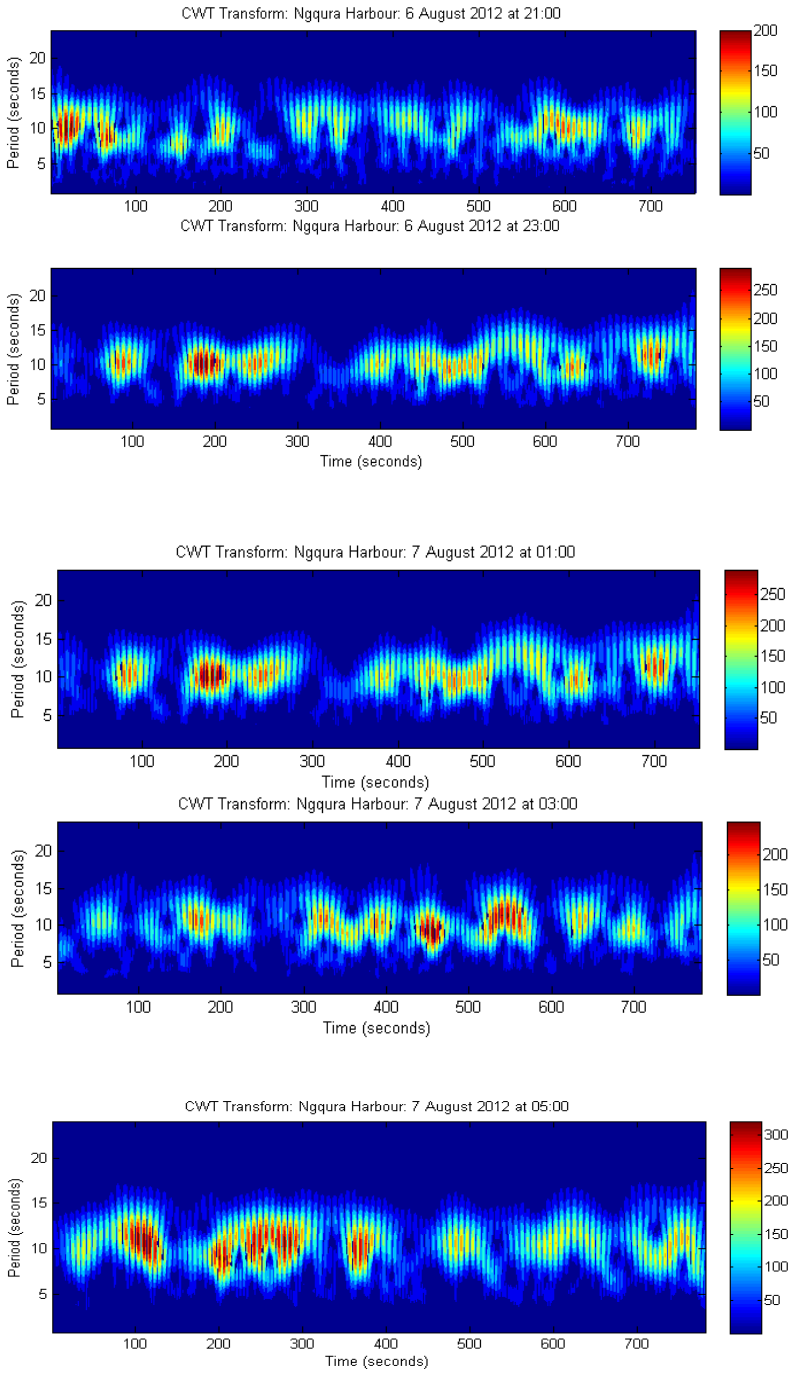

Figure 85: Continuous wavelet transform of time series at Ngqura on 6/7 August 2012.

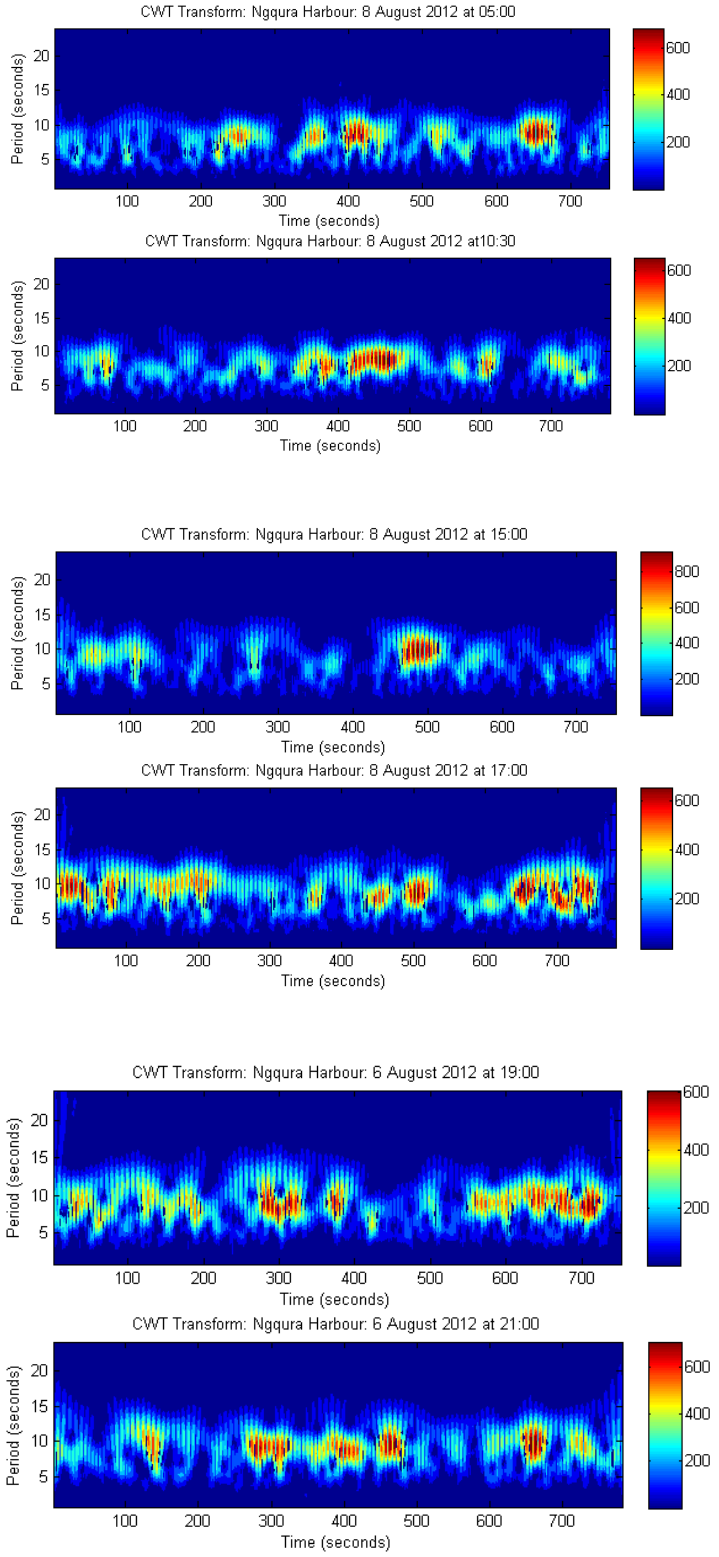

Figure 86: Continuous wavelet transform of time series at Ngqura on 8 August 2012.

Continuous Wavelet Transform plots of the time series at Ngqura harbour on the 6 and the 8 August 2012 at 21:00h have been shown in Figures 87 and 88 respectively, together with plots of their modulus maxima chains. The temporal periods of the energy concentrations in the wave train are clearly evident as was the case for Saldanha Bay

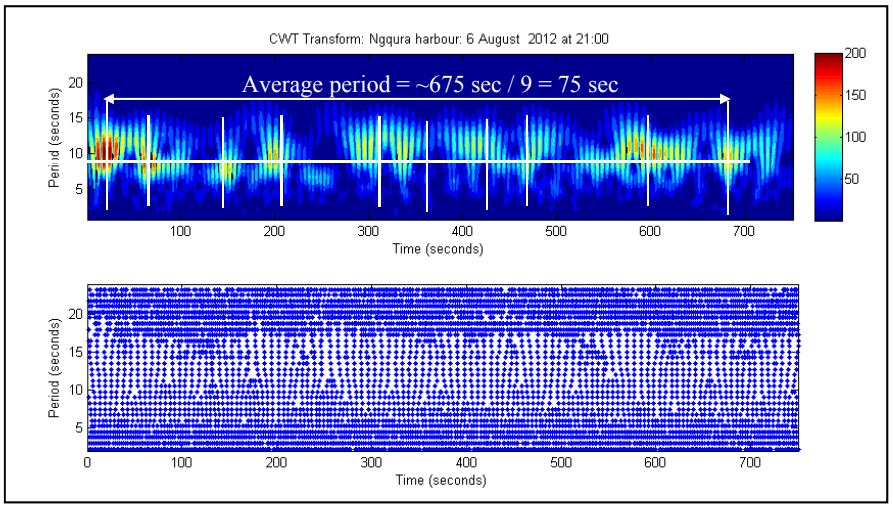

Figure 87: Continuous wavelet transform and modulus maxima chains of time series records at 21:00 on 6 August 2012.

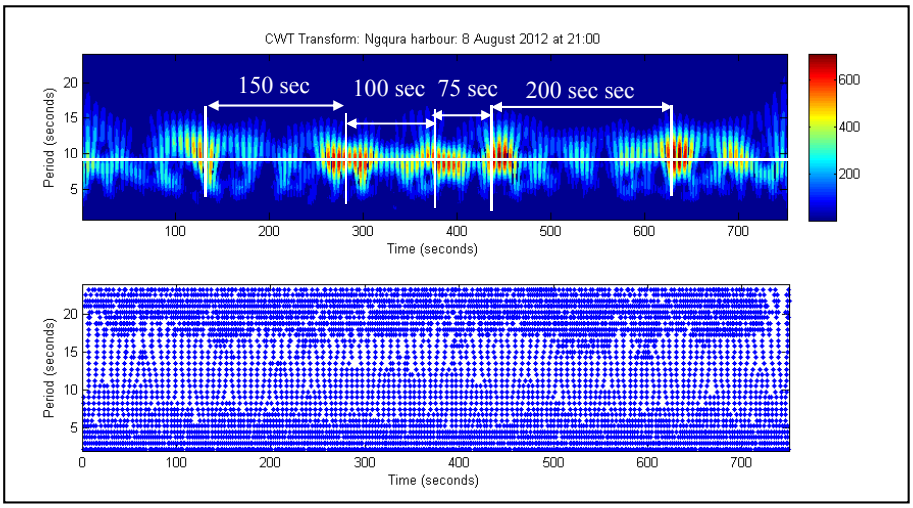

Figure 88: Continuous wavelet transform and modulus maxima chains of time series records at 21:00 on 8 August 2012.

The peak periods for the series on the 6 and 8 August are in the order of 11 and 9 seconds respectively. The corresponding frequencies are 0.09 Hz and 0.11 Hz respectively.

The peak energy distributions of the series of the 6 and the 8 August occur at ~ 75 and ~315 seconds respectively as shown in Figures 74 and 75. In this regard it is interesting to note that long waves with periods of 110 to 230 seconds were recorded at Ngqura harbour on the 1 July 2011, during a time that a vessel in the harbour experienced surges that incurred fender damage (Table 5, Stuart 2013).

The CWT of the first 180 seconds of the time series is shown, together with modulus maxima chains in Figure 89, so that the configuration of the chains can be clearly observed.

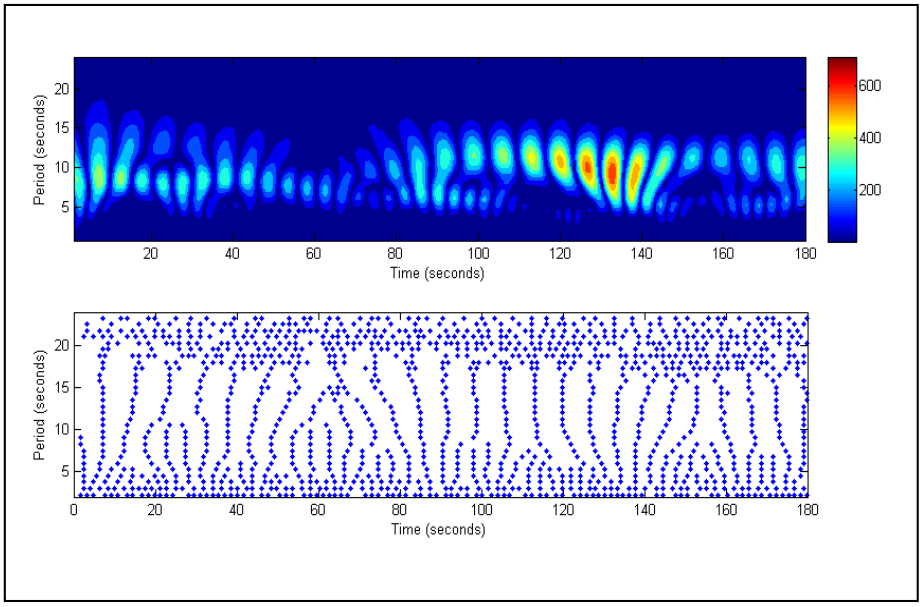

Figure 89: Continuous wavelet transform and modulus maxima chains of 250 time series records at 21:00 on 8 August 2012

As was the case in Saldanha Bay, the figure clearly shows how the chains merge and become much more concentrated at the lower scales (higher frequencies), indicating the nature of the fractal structure of the series.

Singularity Spectral Power envelopes for the time series on 8 August 2012, at four different component wave periods of 5, 10, 15 and 20, have been shown in figure 90.

Again, the envelopes clearly show that peak singularity power groups, occurring at wave periods of 10 seconds, have temporal periods of between 50 and 200 seconds.

These intervals correlate well with infragravity wave periods as well as the resonant periods of ship mooring systems.

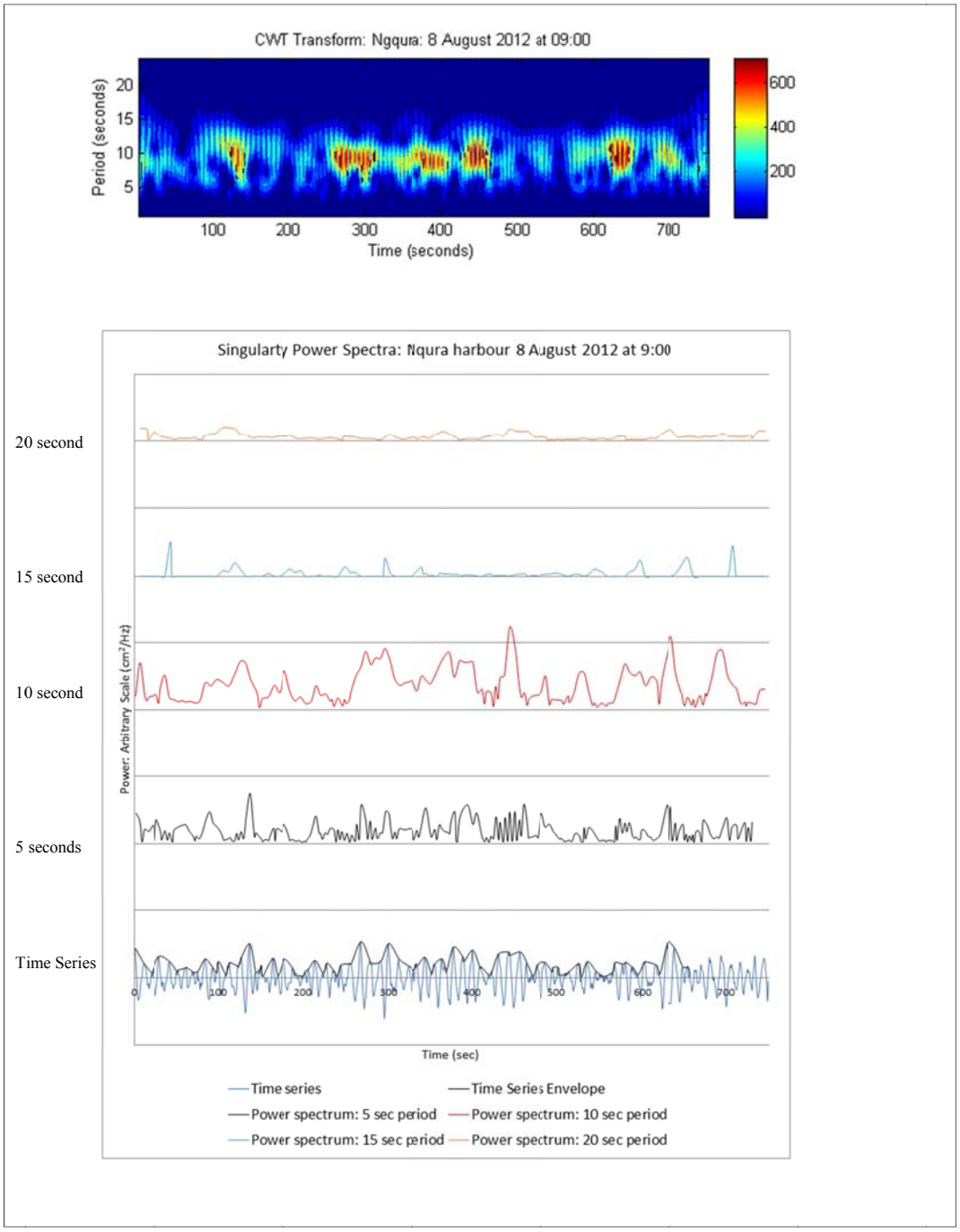

Figure 90: Singularity spectral power envelopes for Ngqura

The relationship between the spectral envelopes and the time series envelope is similar to that discussed for Saldanha Bay.

5.6 Comparison of Wavelet Transform Modulus Maxima configurations for Saldanha Bay Ngqura harbours

Comparative Plots of Singularity and Continuous Wavelet Transform spectra for both non-hazardous and hazardous sea states, at 09:00 hours on the 26 and 28 September 2013 have been shown in Figures 91 and 92, respectively.

The different transforms have been shown together in order to demonstrate the different ways of presenting the same information. The singularity spectra reflect the overall distribution of roughness, or singularities, in the wave train while the wavelet transform spectra reflect the temporal distribution of the singularities and energy in the wave train.

The CWT plots have been shown together with plan, elevation and sectional views of the modulus maxima, in order to be able to observe the following singularity distributions in the wave train:

- The merging of the singularities with respect to scale(period), on the plan view,
- The distribution of the singularities with respect time, and
- The distribution of the power in the singularities with respect to wave period.

On the 26 September (refer to Figure 91), the singularities can be seen to merge at the lower scales, or higher frequencies, in the normal way. The singularities have an irregular distribution with respect to time and they peak at a period of 8 seconds.

On the 28 September (refer to Figure 92), the singularities also merge at the lower scales, but they cluster more regularly with respect to time and they peak at a period of 11 seconds.

The distribution of singularities during the non-hazardous sea state on the 26 September can be seen to be irregular while those during the hazardous sea state on the 28 September can be seen to be more regular.

In a similar way, comparative Plots of Singularity and Continuous Wavelet Transform spectra for both a non-hazardous sea state, at 21:00 hours on the 6 August 2012, and a

hazardous sea state, at 10:30 on the 8 August 2012 have been shown in Figures 93 and 94 respectively.

In this case the singularities of both the non-hazardous and hazardous sea states are seen to have a similar regular distribution, but the variations in intensities are more irregular during the hazardous sea state on the 8 August.

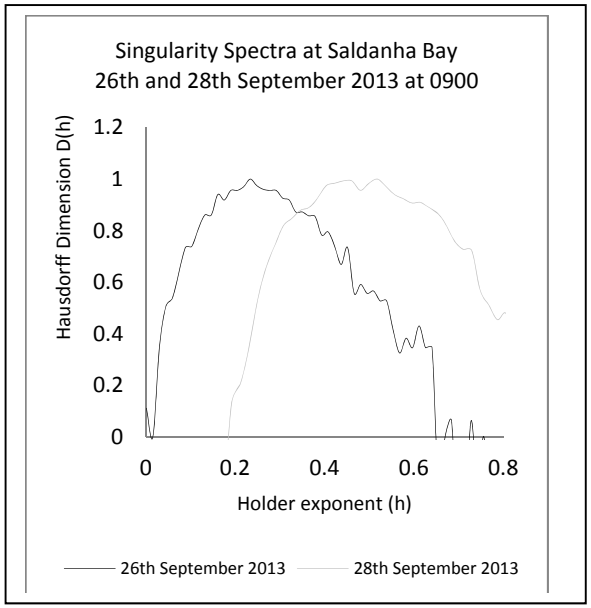

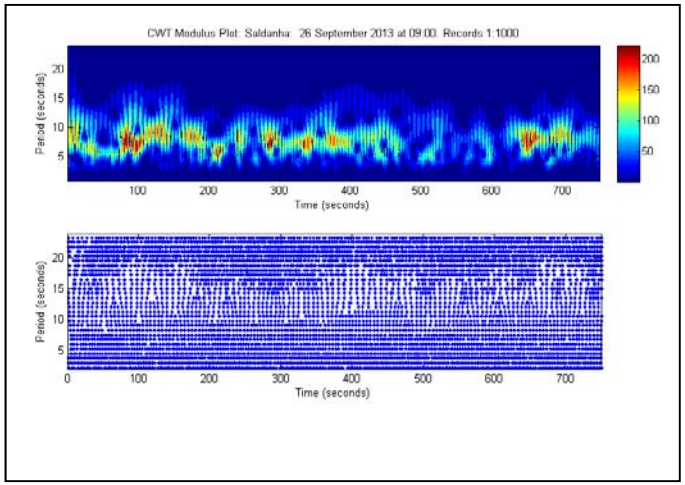

Figure 91: Comparative singularity and wavelet modulus maxima spectra for Saldanha Bay on 26 September 2013

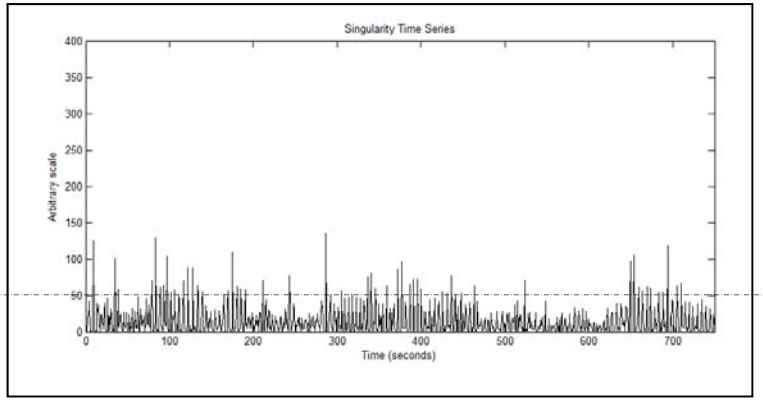

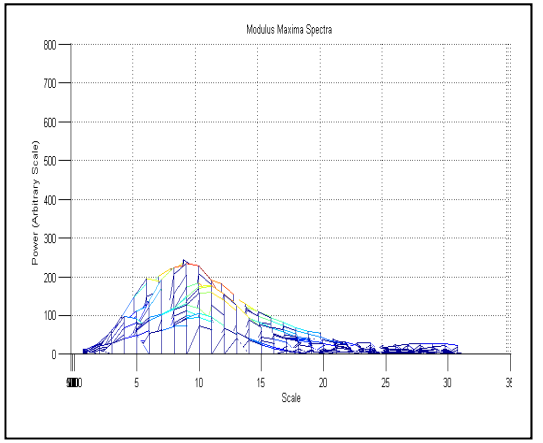

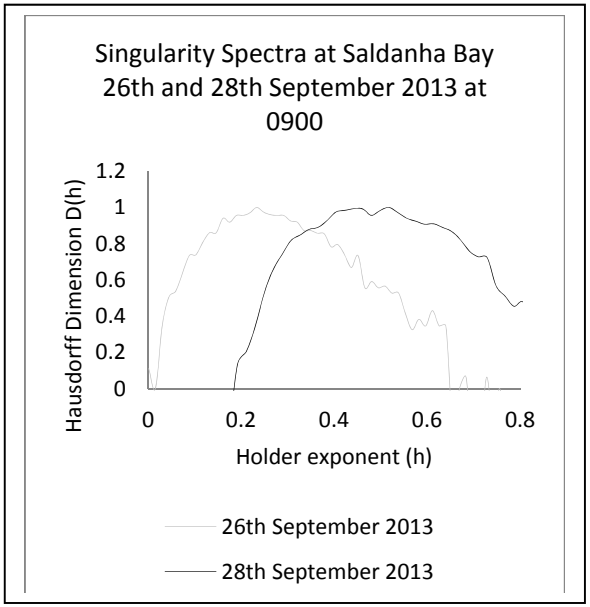

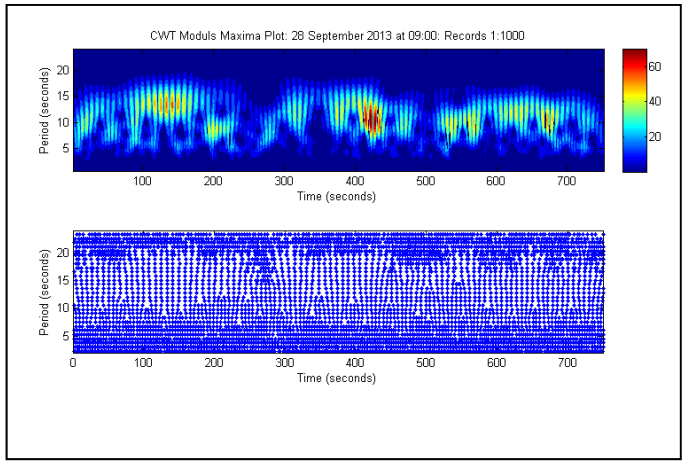

Figure 92: Comparative singularity and wavelet spectra for Saldanha Bay on 28 September

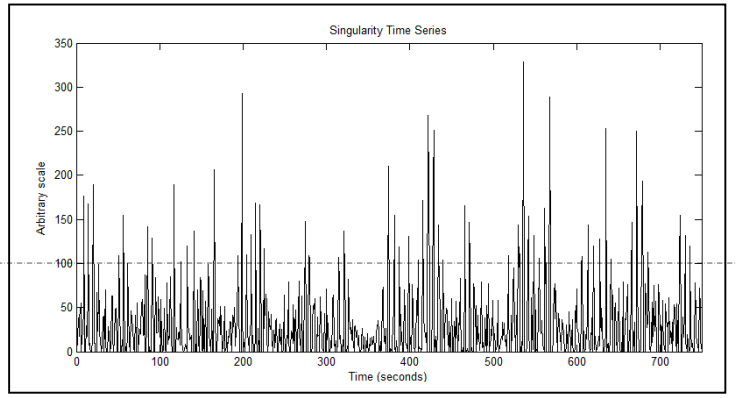

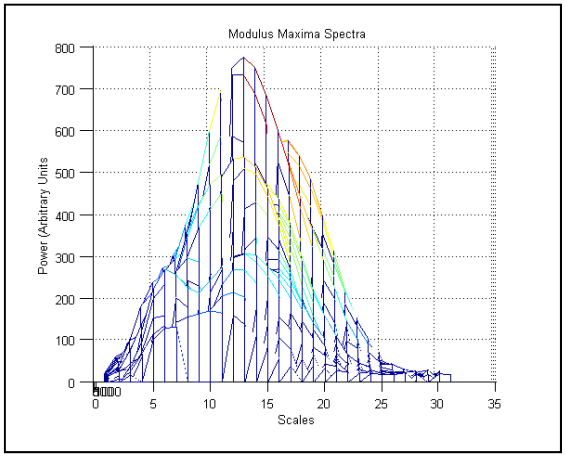

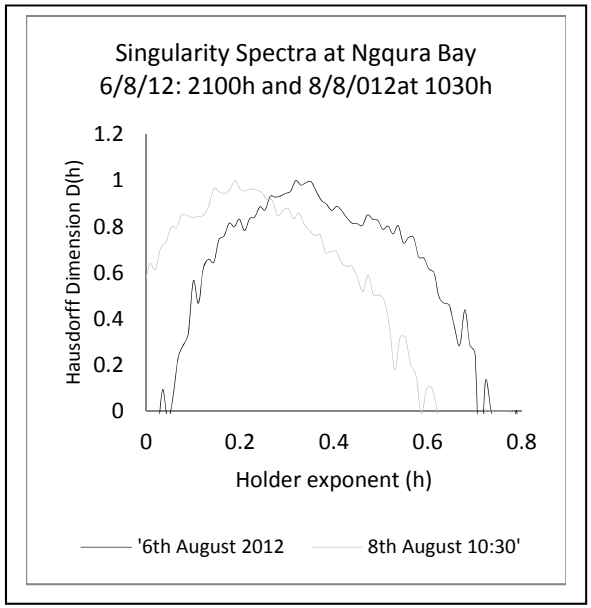

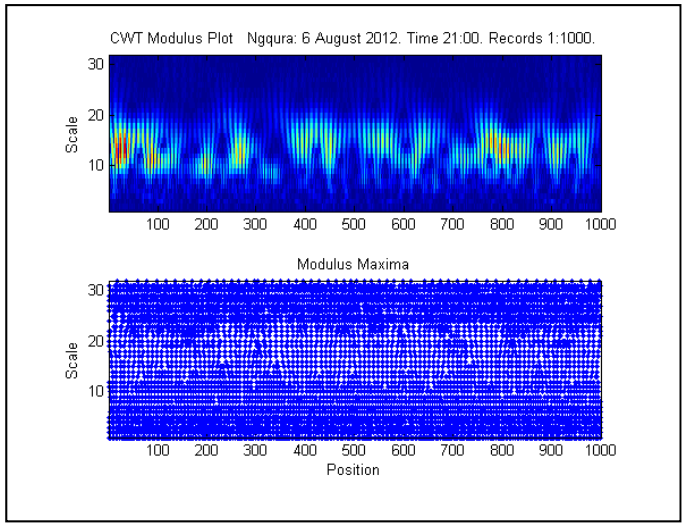

Figure 93: Comparative singularity and wavelet spectra for Ngqura on 6 August 2012

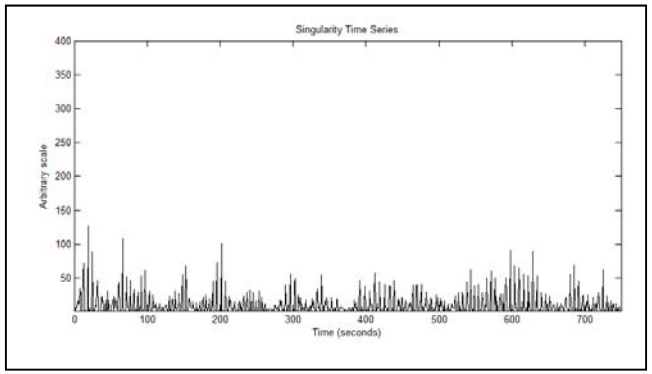

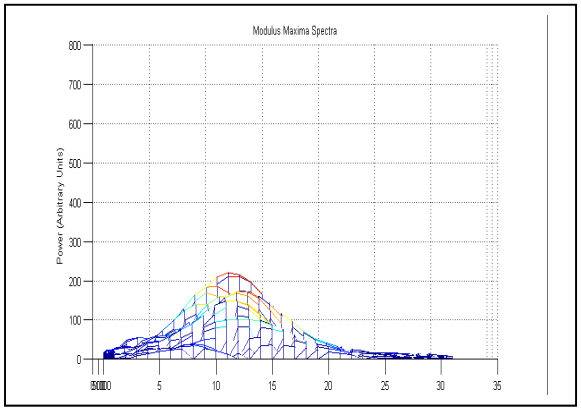

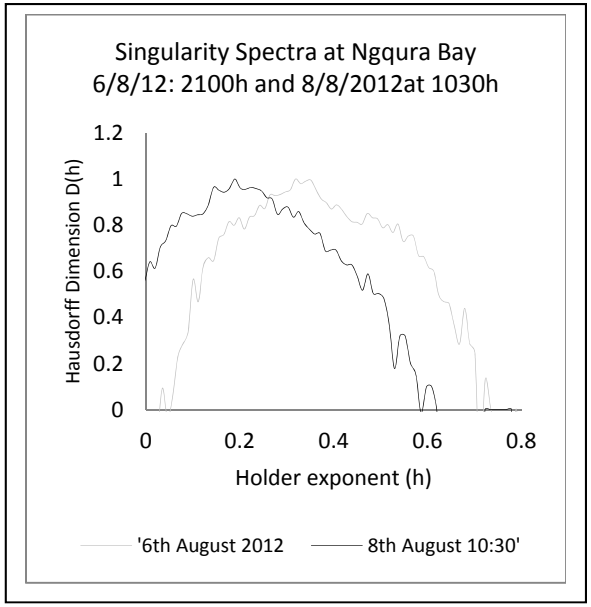

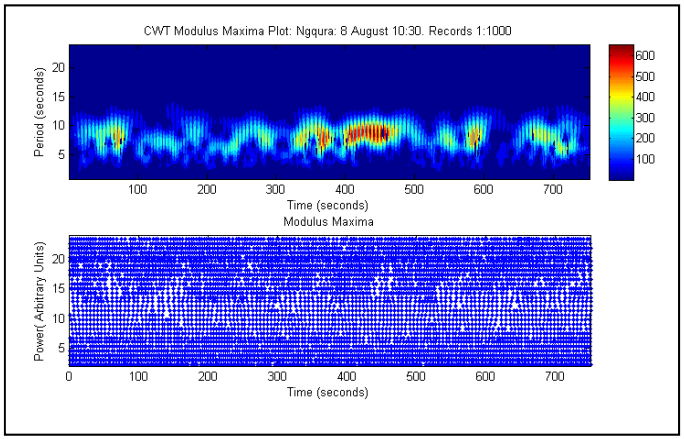

Figure 94: Comparative singularity and wavelet Spectra for Ngqura on 8 August

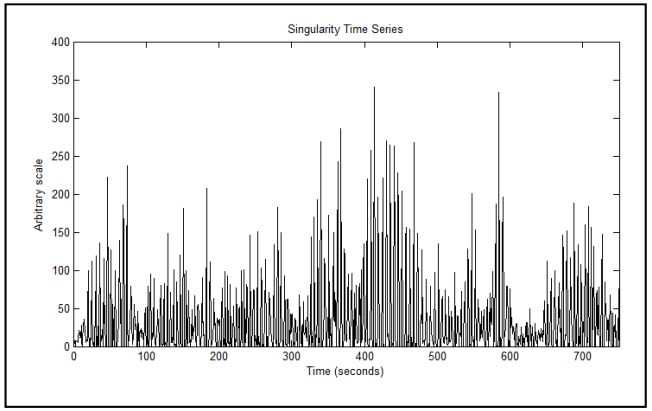

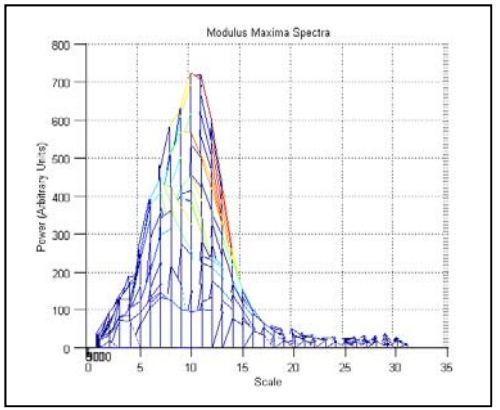

5.7 Multifractal Detrended Fluctuation Analysis (MDFA) of longer term time series

The singularity distributions of longer term time series of 2304 records (30 minutes) at Saldanha Bay harbour on the 22 and 25 June 2013, the 13 and 18 August 2013 and the 26 and 28 September 2013 were analysed by means of the MDFA method. Each of the six sets and data, except the one recorded on the 26 September 2013, as collected during days when moorings had parted due to long wave action in the harbour. The exact times of the incidences are only precisely known for the event on the 28 September 2013.

The singularity spectra of the time series are shown on figure 95.

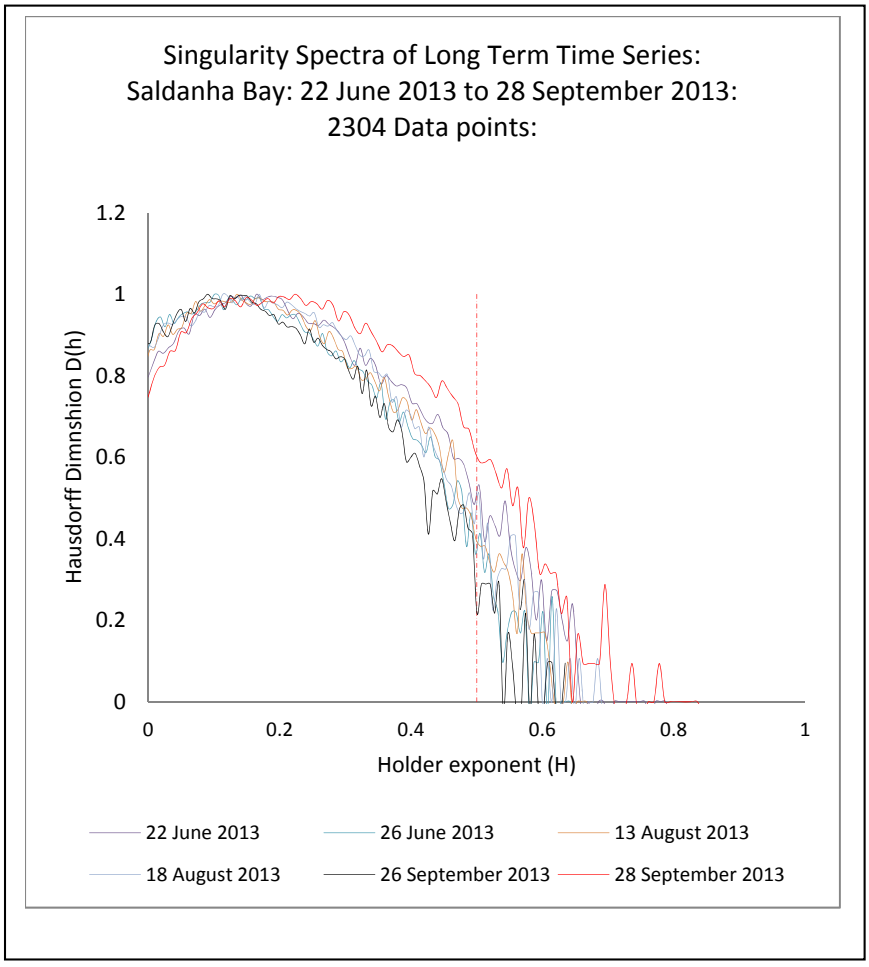

Figure 95: Singularity Spectra of Long Term Time Series

The spectrum representing the 26 September 2013, during the non-hazardous sea state is indicative of the most non-correlated and rough displacements of the set, while the spectrum of the 28 September 2013 is indicative of the most correlated and smooth, displacements of the set. The other spectra fall into an intermediate range of correlation and roughness. The broken mooring incident of 28 September 2013 is the most severe of the different cases and would have coincided with the occurrence of the most dominant wave groups and infragravity wave systems.

5.8 Analysis of period averaged singularity power distribution

Period averaged singularity power spectra for the 30 minute long wave trains recorded during periods of long wave action at Ngqura harbour on the 8 August 2012, and at Saldanha Bay harbour on 22 June and 25 June 2013, the 13 and 18 August 2013 and the 28 September 2013 have been shown in figures 96 to 101.

The spectra have been derived for wave periods ranging from 5 to 15 seconds and the peaks of power can clearly be seen to have typical period s of between 50 and 300 seconds.

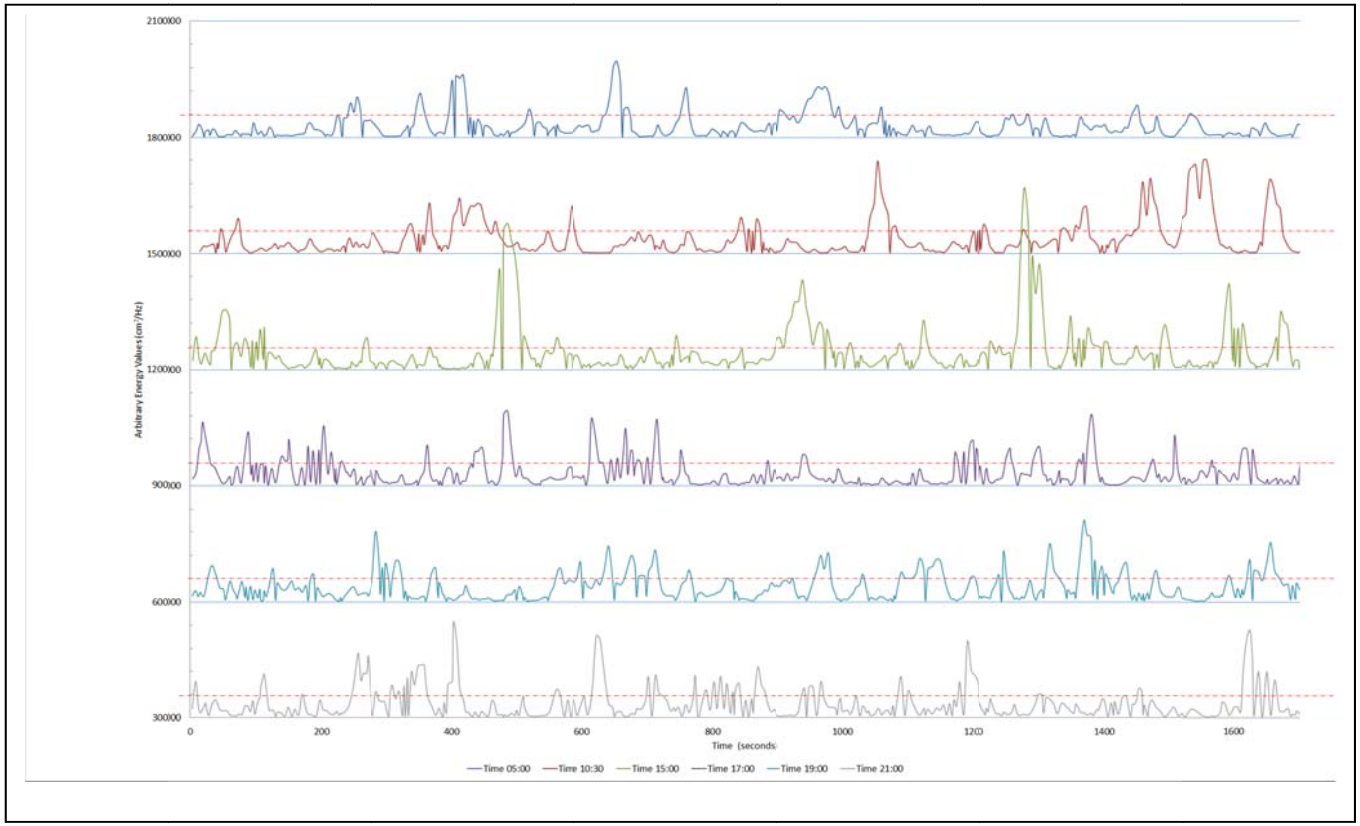

Figure 96**:** Period averaged singularity power spectra (5 to 15 seconds) for Ngqura Harbour on 8 August 2012

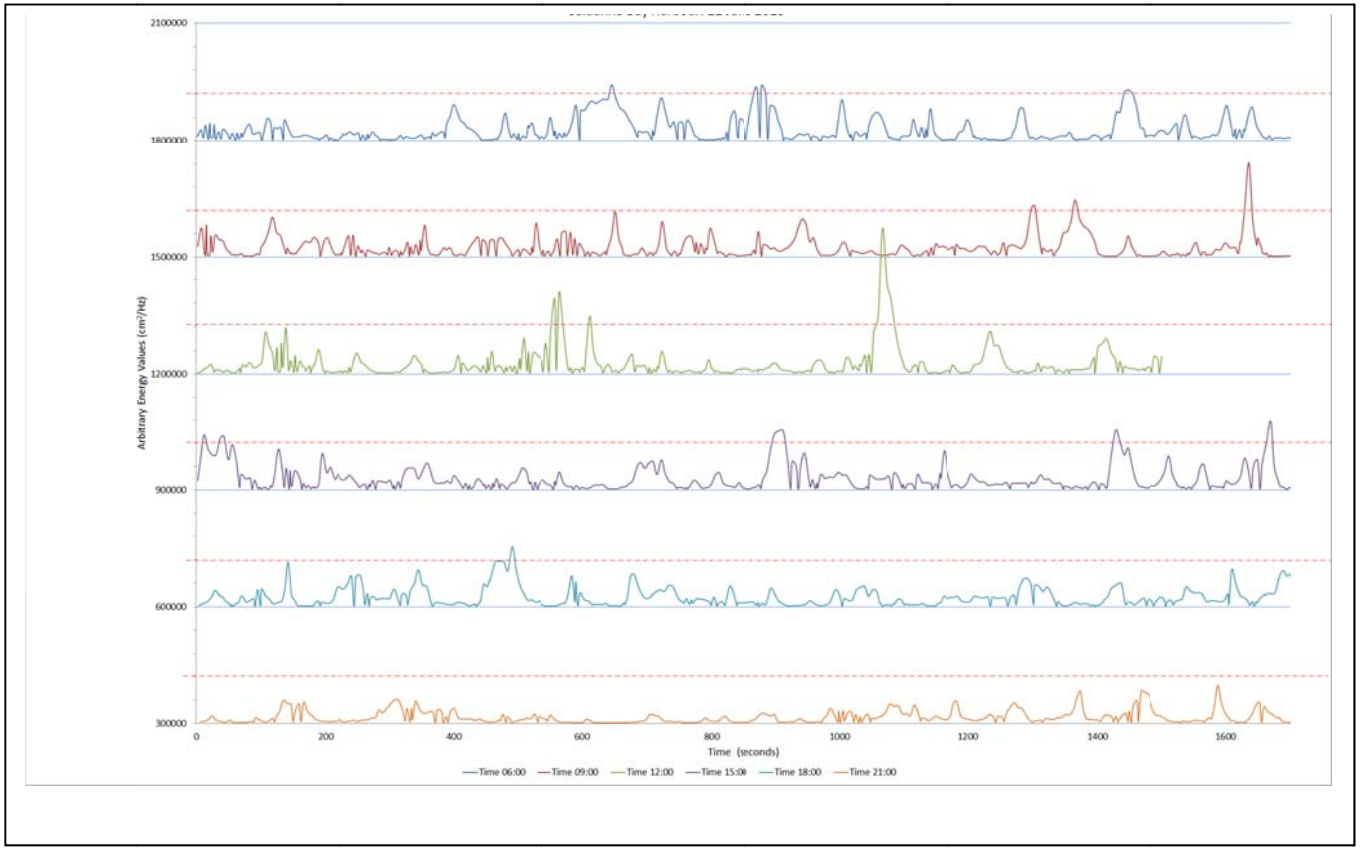

Figure 97: Period averaged singularity power Spectra (5 to 15 seconds) for Saldanha Bay Harbour on 22 June 2013

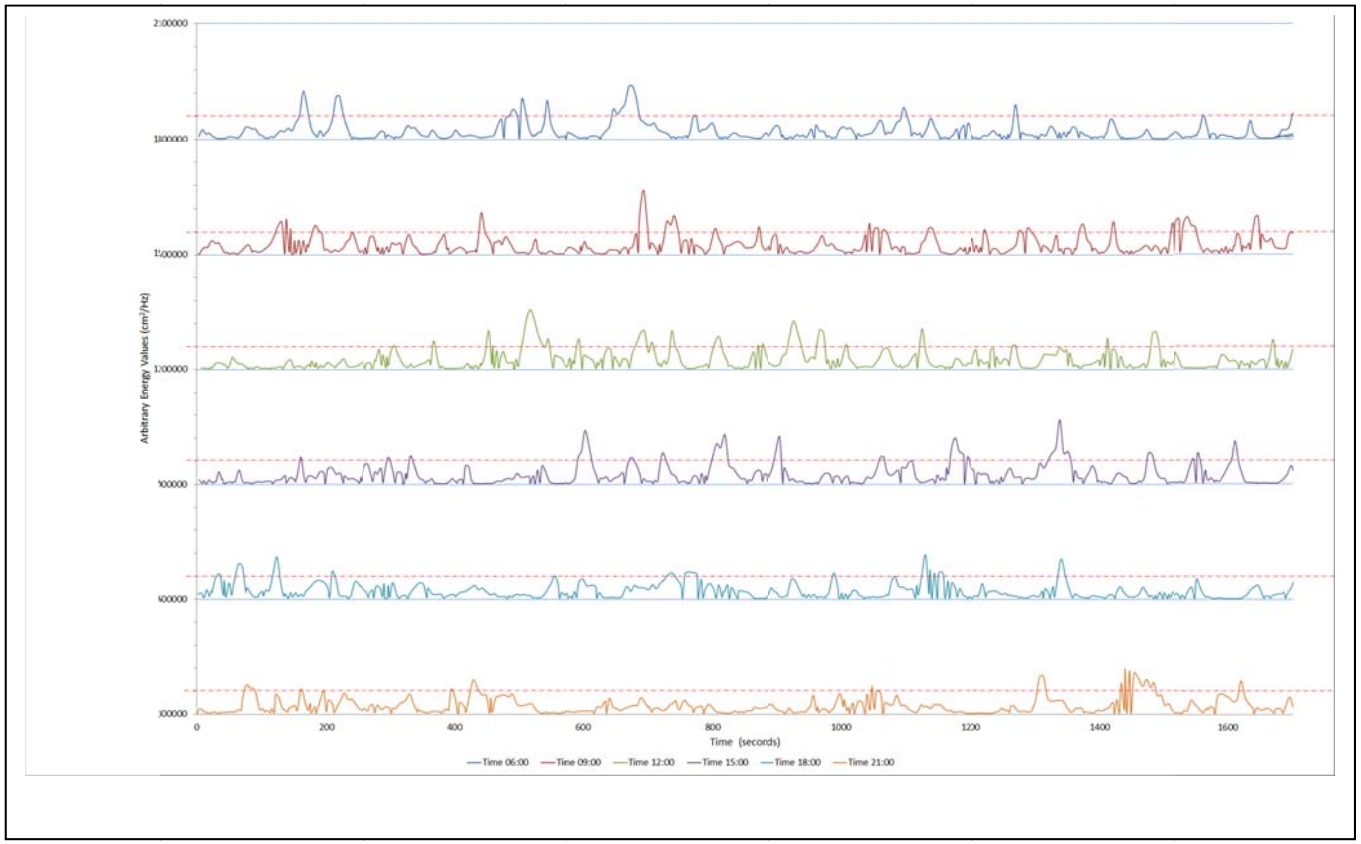

Figure 98: Period averaged singularity power Spectra (5 to15 seconds) for Saldanha Bay Harbour on 25 June 2013

Figure 99: Period averaged singularity power spectra (5 to 15 seconds) for Saldanha Bay Harbour on 13 August 2013

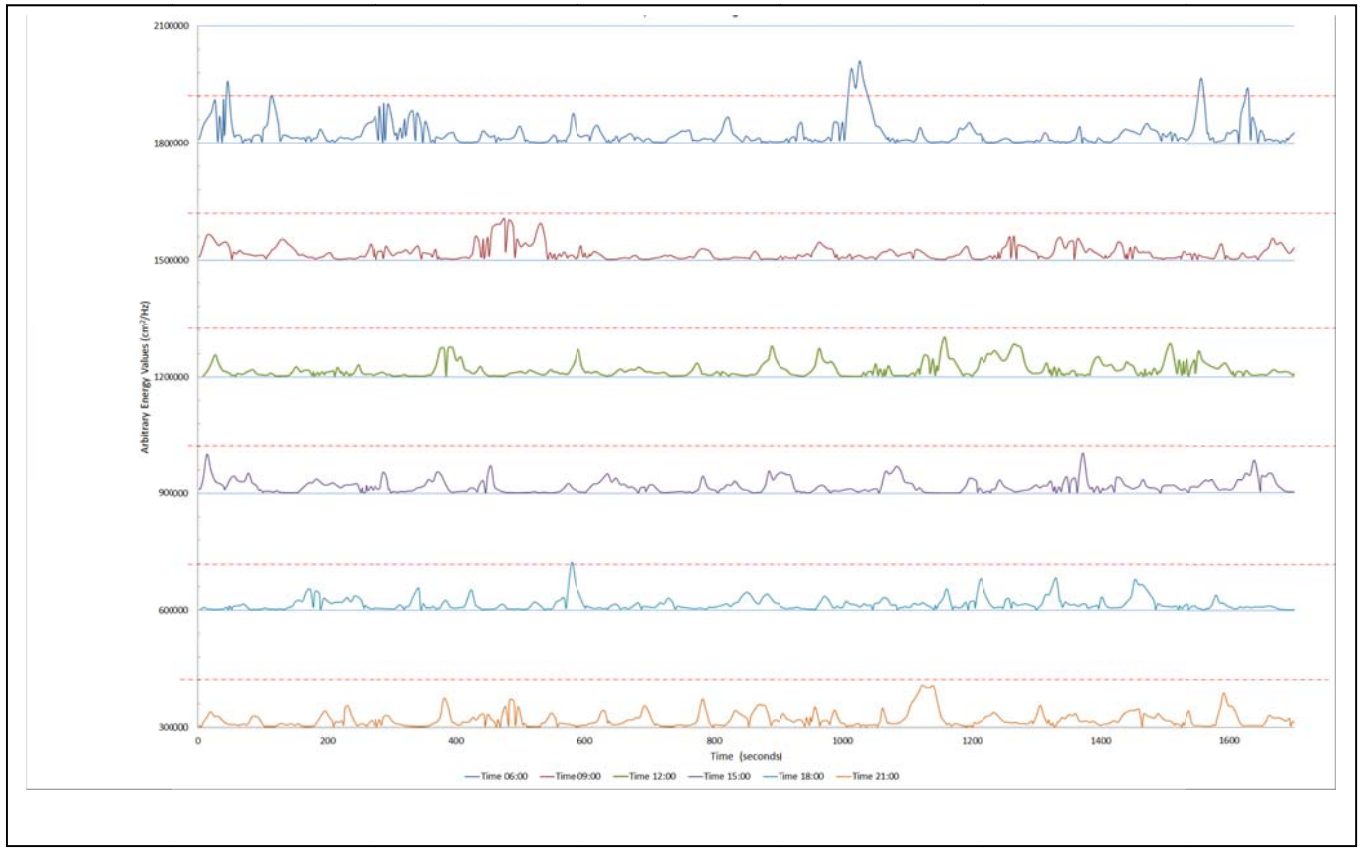

Figure 100: Period averaged singularity power spectra (5 to 15 seconds) for Saldanha Bay Harbour on 18 August 2013

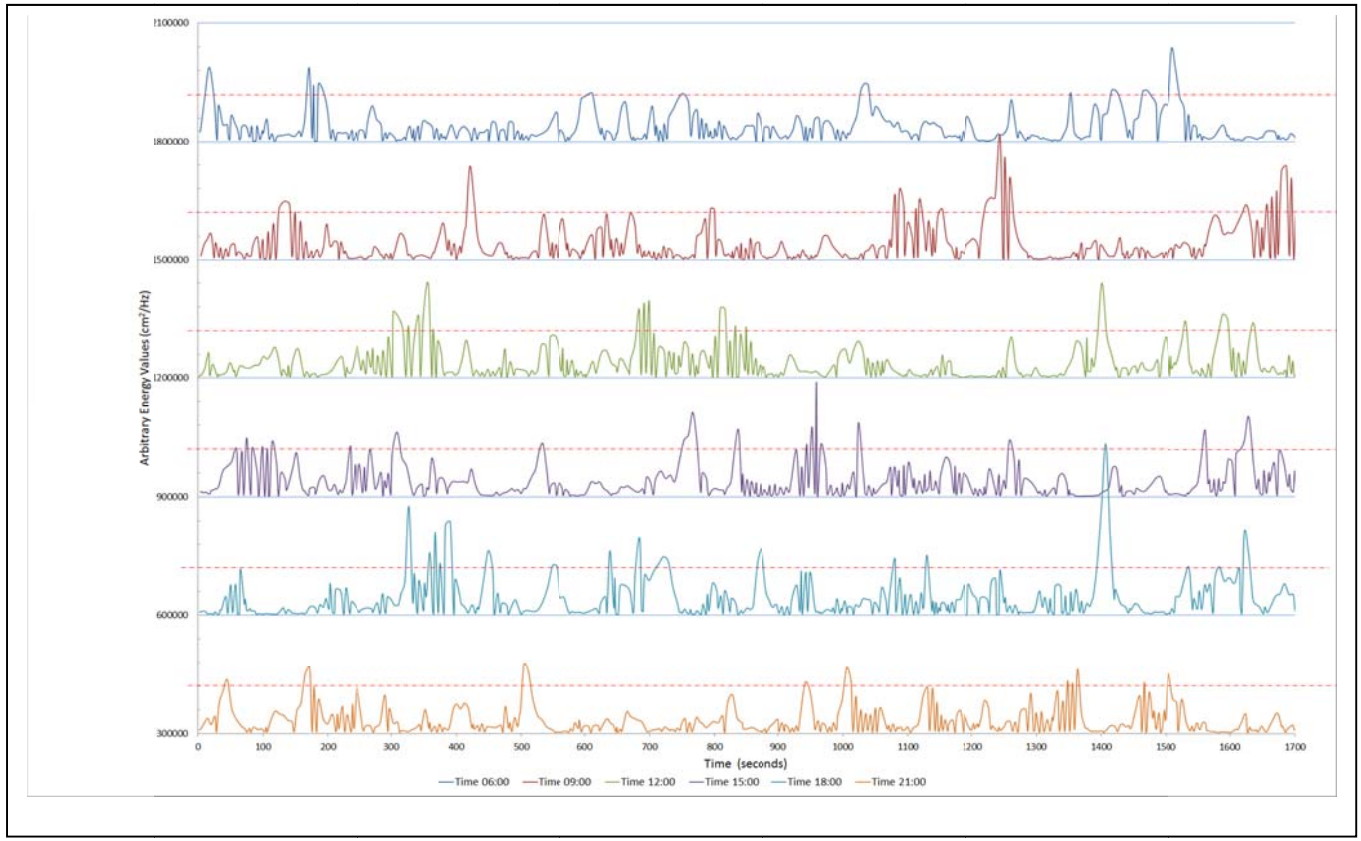

Figure 101: Period averaged singularity power Spectra (5 to 15 seconds) for Saldanha Bay Harbour on 28 September 2013

5.9 Summary of Chapter 5

Chapter 5 gives details of the software used for the analysis of the selected time series and then it leads on to give details of the analysis of the open lake water and harbour time series data.

The chapter covers the analysis of the above data in the time domain, by means of the Rescaled Range and Multifractal Detrended Fluctuation Analysis methods, and it the frequency domain by means of the Fourier and Wavelet transform methods.

The configurations and spectral density distributions of the singularities in the time series collected from the harbours are analysed and comparisons are made between the results of these analyses for both the hazardous and non-hazardous sea states at each of the harbours.

6. FINDINGS

6.1 Evaluation of fractal analysis methods

All of the fractal analysis methods that have been investigated in this research have been found to be effective in identifying multifractal sea states. However, both the Rescaled Range (R/S) and Spectral exponent methods cannot be used to differentiate between the fractal dimensions derived for the non-hazardous and hazardous bound infragravity wave sea states. Both of these methods describe a fractal system on the basis of the Hurst exponent, which by its nature is a single global value. Further, the limited sets of data that were used in this research do not allow one to determine a statistical level of confidence between the derived Hurst exponent values for the different sea states.

On the other hand, both the Multifractal Detrended Fluctuation Analysis (MDFA) and the Continuous Wavelet Transform (CWT) methods of analysis identified clear differences between the fractal indices and dimensions of the non-hazardous and hazardous bound infragravity wave sea states. In the former case the frequencies of occurrence of the local Holder exponents were shifted and redistributed significantly, and in the latter case the spectral and temporal distributions of the peak singularity strengths, as determined by the intensities of the local holder exponents, were significantly different.

The CWT technique was the only fractal method of analysis that could be used for the study of infragravity waves *per se.*

6.2 Proof of Hypothesis

The Hypothesis, which is the basis of this research, has been partially proven to be correct in that Bound Infragravity Wave (BIW) sea states are multifractal systems capable of being geometrically modelled and described in terms of the distribution of their singularities in such a way that:

- Different sea states can be characterised, quantified and described,
- Different sea states can be compared quantitatively with each other.

The hypothesis would need much more extensive testing than that undertaken in this research in order to develop a higher level of confidence in the results.

6.3 Conventional wave characteristics of Saldanha Bay and Ngqura Harbours

The conventional wave characteristics of H_{m0}, f_p and t_p, for Saldanha Bay and Ngqura harbours were calculated from the frequency domain analysis of single point time series data. The different values are summarized in Table 23.

Table 23: Comparative significant wave heights, peak frequencies and peak periods

Characteristic	Saldanha Bay Harbour		Ngqura Harbour	
	Before BIW Sea State 26 September 2013	During BIW Sea State 28 September 2013	Before BIW Sea State 6/7 August 2012	During BIW Sea State 8 August 2012
Average Significant Wave height (Hm0)	1.40 m	3.01 m	1.17m	3.46m
Average Peak Wave Frequency (fp)	.08 Hz	.07 Hz	.08 Hz	.10 Hz
Average Peak Period	11.9 sec	14.5 sec	13.0 sec	11.0 sec

The significant wave heights at Saldanha Bay and Ngqura harbours were found to be a very similar to each other both before and during hazardous BIW sea state. These wave heights were 1.4 m and 1.7m for the non-hazardous sea state and 3.01 m and 3.4 m respectively for the hazardous sea state. The average peak period values for both

the non-hazardous and hazardous seas states at Saldanha Bay and Ngqura shifted by 2.6 and 2.0 seconds respectively. In the case of Saldanha Bay the shift was from a lower (higher) to a higher (lower) period (frequency), while at Ngqura harbour the shift was from higher (lower) to a lower (higher) period (frequency). These conditions are indicative of an increased swell environment at Saldanha Bay, and increased wind sea environment at Ngqura, during hazardous bound infragravity wave sea states.

Notwithstanding the fact that these trends are confirmed by similar trends in the fractal dimensions (to be discussed later), they would need much more extensive testing than that undertaken in this research in order to develop a higher level of confidence in the results.

6.4 Fractal dimensions and indices for bound infragravity wave (BIW) sea states at Saldanha Bay and Ngqura Harbours

The significant fractal dimension and index that have been derived by the MDFA method for BIW Sea State at Saldanha Bay and Ngqura harbours, have been summarised in Table 24.

Table 24: Fractal dimension and indices for hazardous BIW sea states at Saldanha Harbour.

Dimension Type	Method of Analysis	Fractal Index	Reference
		Saldanha Bay	Ngqura
Fractal Dimension (D)	Derived from Hurst exponent	D = 1.56	D = 1.77
Peak Holder exponent h(p) and Global Hurst exponent (H)	Multifractal Detrended Fluctuation Analysis (MDFA): Derived from Singularity Spectrum	h(p) = .44	h(p) = .23

Stiassnie derived the Fractal Dimension, D, for the open sea surface and for unidirectional waves in 1988 and by Ajiwibowo in 2002. Stiassnie based his work on theory while Ajiwibowo based his work on the analysis of single point time series data. The values derived by Stiassnie and Ajiwibowo are in close agreement with those derived in this research, and they have been summarized in Table 25.

Table 25: Comparison of fractal dimensions and Hurst exponents for the ocean surface and for vertical sea surface displacements.

Researcher	Type of Data Used for analysis	Method of Analysis	Fractal Dimension		Hurst Exponent (* Derived from D)	
			Single point data	Spatial data	Single point data	Spatial data
Stiassnie (1991)	Spatial equations	Theoretical calculations based on Zakharov's and Hasselmann's Equations and Pierson's linear model	1.3	$2.3 < D < 3.0$	-	0.70* to 0.0*
Ajiwibowo (2002)	Single point time series in open sea water	Rescaled Range (R/S)	$1.5 < D < 1.8$	-	$.50^* > H > .20^*$	-
MacHutchon (2014)	Single point time series in open sea water	MDFA method.in domain	$1.5 < D < 1.9$	-	$.48 > H > .10$	-

6.5 Comparison of singularity spectra for hazardous BIW sea states in Saldanha Bay and Ngqura Harbours

The average Singularity Spectra for both Saldanha Bay and Ngqura harbours during non-hazardous and hazardous conditions have been shown in Figure 102.The overall trends that can be observed in these spectra indicate that:

- The two sea states at each of the harbours are different in terms of both their peak Holder exponent values and the frequencies of occurrence of their different local Holder exponent values.
- The hazardous BIW sea states (shown in red) at the different the harbours also have different fractal characteristics.

In this regard we note the following:

- The sea surface displacements during a hazardous BIW sea states in Saldanha bay harbour are generally smoother, or more regular, than they are for non-hazardous conditions. This finding is indicative of an increased swell as well as longer periods and it is confirmed by the spectral analysis of the time series data where the peak period can be seen shifts towards a lower value for the hazardous sea state.
- The sea surface displacements in Ngqura harbour are generally rougher and more irregular during hazardous conditions than they are for non-hazardous conditions, This finding is also confirmed by the spectral analysis of the time series where the peak period can be seen to shift towards a higher frequency for the hazardous sea state.
- The hazardous BIW sea states at Saldanha Bay harbour are generally smoother, or more regular, than they are for the same conditions at Ngqura.

The different fractal indices for both Saldanha Bay and Ngqura harbours are shown in table 26.

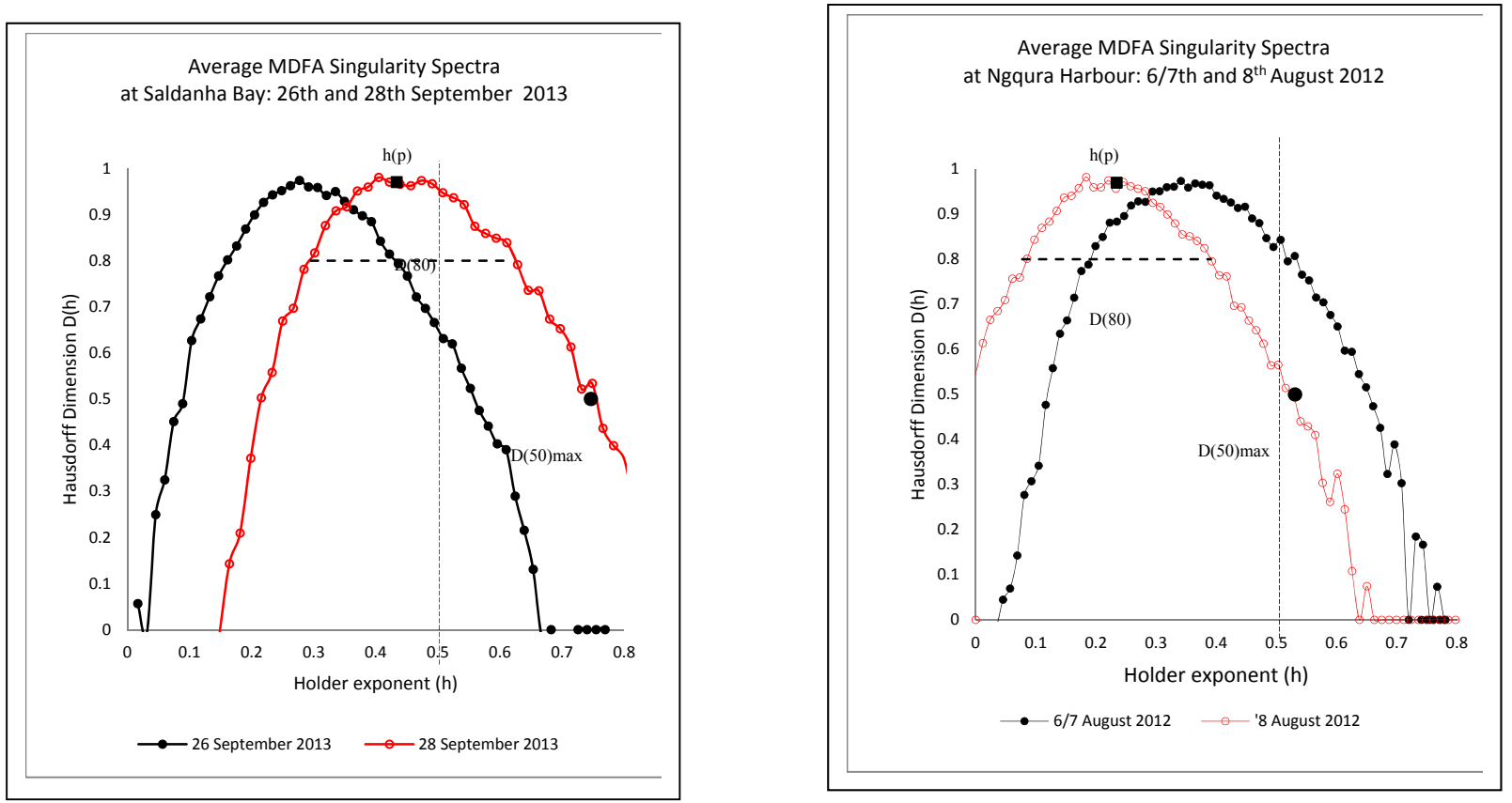

Figure 102: Singularity spectra for both Saldanha bay and Ngqura harbour

Table 26: Range of the following fractal indices for both Saldanha Bay and Ngqura harbours during hazardous sea states

Fractal Index		**Saldanha Bay harbour**		**Ngqura harbour**		**Comments**
	Description	Range	Average	Range	Average	
Peak Holder exponent: h(p)	The type of displacement (rough to smooth) that is generally most prevalent in the recorded sea surface displacements	.39 to .52 = .13 units	.46	.15 to .3 = .16 units	.23	Similar range of roughness Correlated surface displacements Uncorrelated randomness
Broadness of Singularity Spectrum D(80):	A measure of the spread of irregularity (rough to smooth) time series	.26 to .37 = .11 units	.32	.26 to .35 = .09 units	.31	Similar spread of surface roughness Uncorrelated randomness
Maximum Holder exponent with a 50% intensity: D(50)max.	A measure of the strength (or presence) of the smoothest sequences of displacements in the time series	.70 to .81 = .12 units	.76	.47 to .59 = .12 units	.53	The same distribution of roughness Smooth Correlated Correlated

The multifractal MDFA method of analysis provides a more complete description of the time series data than the monofractal techniques.

6.6 Probability of non-exceedance of local Holder exponent values

Saldanha Bay and Ngqura harbours both have correlated persistent sea surface displacement characteristics, with Holder exponent values in excess of 0.5, during non-hazardous and the hazardous sea state conditions.

The cumulative frequency of occurrence functions, which have been derived from the singularity spectra and which are the same as the probability of non-exceedance functions for the Holder exponent values at the two harbours, have been shown on Figures 103 and 104.

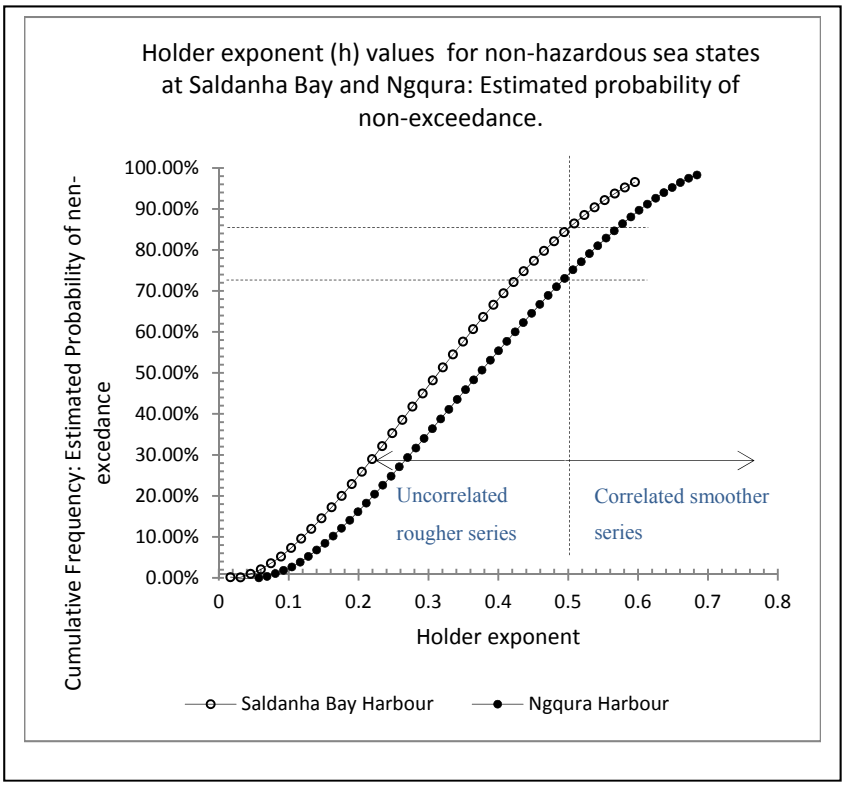

Figure 103: Holder exponent (h) values for non-hazardous sea states at Saldanha Bay and Ngqura Harbours.

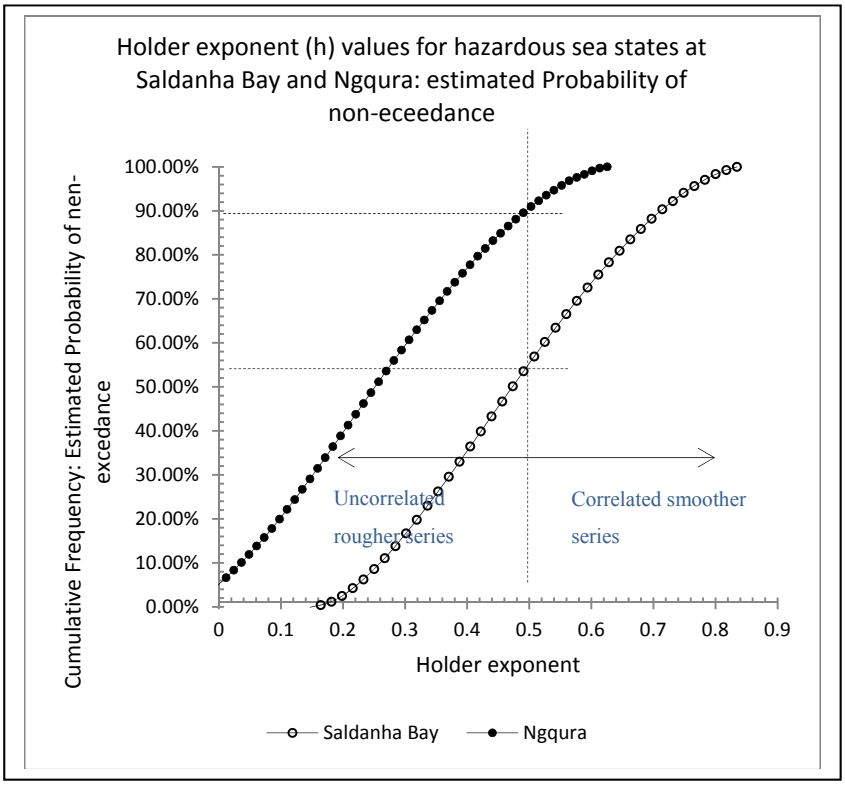

Figure 104: Holder exponent (h) values for hazardous sea states at Saldanha Bay and Ngqura Harbours.

The probabilities of non-exceedance and of exceedance have been summarized in Table 27.

Table 27: Probabilities of non-persistence and persistence at Saldanha Bay and Ngqura Harbours.

Sea State Condition	**Saldanha Bay harbour**		**Ngqura harbour**	
	Probability of non-correlated displacements (h < .5)	Probability of correlated displacements (h > .5)	Probability of non-correlated displacements (h < .5)	Probability of correlated displacements (h > .5)
Non-hazardous sea state	85%	15 %	72 %	28 %
Hazardous sea state	55%	45 %	90 %	10 %

It can be seen that there is a higher probability of correlated surface displacements at Ngqura harbour, than there is at Saldanha Bay harbour during non-hazardous conditions. However this situation is reversed during hazardous sea state when the probability of correlation at Saldanha Bay exceeds that at Ngqura.

The reason for the changes in surface displacement correlation at the two harbours is probably due to the fact that Saldanha Bay harbour is directly exposed to the open sea in a predominantly swell environment, while Ngqura harbour is situated inside a protective bay in a predominantly high wind environment.

These findings are not, in themselves, new but what is considered to be new is the fact that the fractal analysis of the sea surface displacements offers the coastal engineer a means of quantifying the degree of the difference between the sea states in terms of both surface roughness and probabilities of occurrence.

6.7 Comparison of singularity spectral power groups in non-hazardous and hazardous BIW sea states in Saldanha Bay and Ngqura Harbours

Continuous Wavelet Transforms of a typical time series from a non-hazardous and hazardous sea state at Saldanha Bay and Ngqura harbours have been shown in Figure 105. The locations of the peaks have been marked with vertical lines and it can clearly be seen that there is a significant difference between both the frequency and the temporal distributions of the singularity power groups.

The slow variations I spectral power would constitute a varying force on ship mooring systems and the periods of between 25 and 300 seconds for the two harbours would be resonate with ship mooring systems. It is quite possible that some of the larger peak power periods would act on the mooring systems in such a way that they would constitute separate events rather than a continuously linked resonating series. Conversely, if the periods are too short peaks could constitute a single force on a mooring system, rather than a series of forces in a single series.

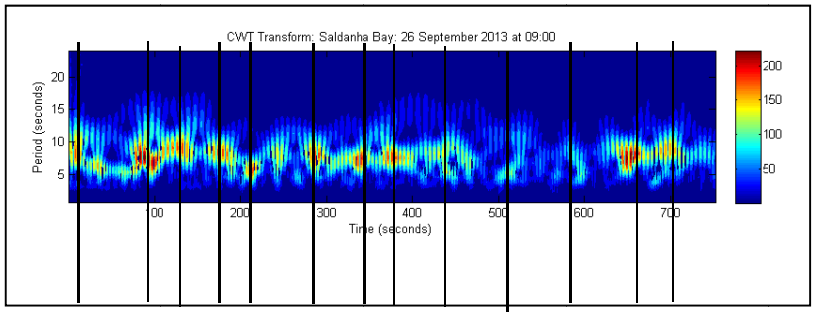

a. Saldanha Bay on the 26th September 2013 at 0900

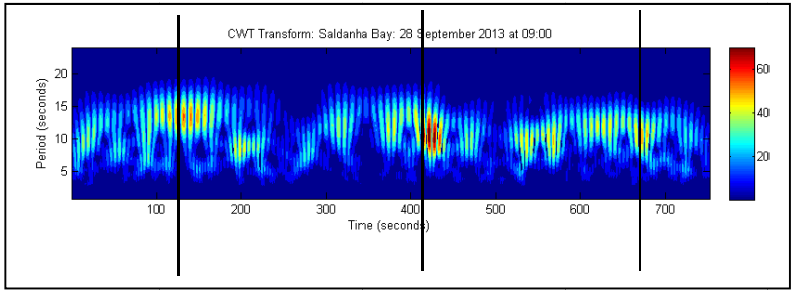

b. Saldanha Bay on the 28th September 2013 at 0900

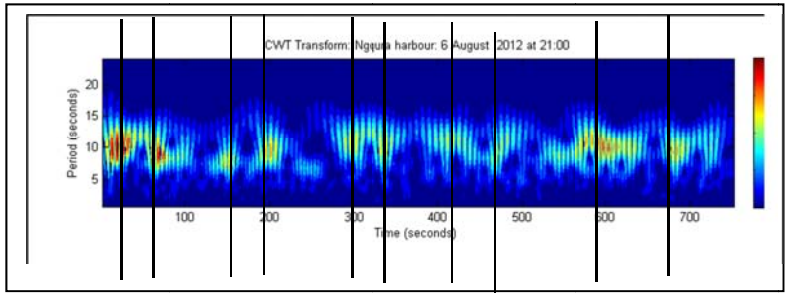

c. Ngqura on the 6th August 2012 at 2100

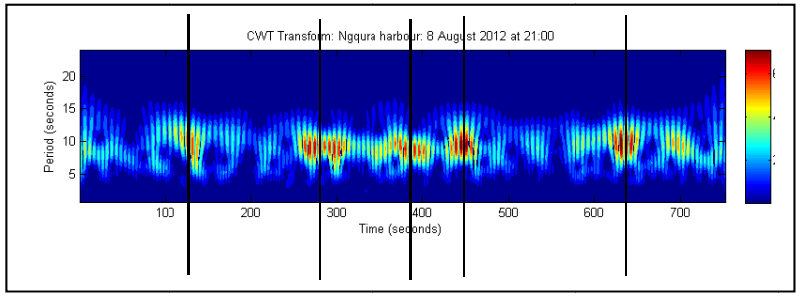

d. Ngqura on the 8th August 2012 at 2100

Figure 105: Singularity power distributions at Saldanha Bay and Ngqura Harbours.

The peak frequencies for the different intervals of the time series are similar to each other for each of the sea states. Further, they correlate very well with the power spectral density functions for the different series. On the other hand, the non-hazardous and hazardous sea states at each of the harbours have very different peak spectral power distributions in the time domain. These temporal power distributions vary with the wave periods (frequencies) at both harbours, as shown in Figure 85 for Saldanha Bay harbour.

6.8 Summary of Chapter 6

Chapter 6 records the main findings of the research. This includes a review of the different methods of fractal used in the research from the point of relevance insofar as the identification of a hazardous Bound Infragravity Wave (BIW) sea states at Saldanha Bay and Ngqura harbours.

The chapter goes on to include a consideration of whether or not the hypothesis that formed the basis of the research has been proven.

Comparisons are made between the singularity spectra and the probabilities on non-exceedance of local Holder exponents and findings are made with regard to their differences.

Finally, comparisons are made between the distributions of the singularity spectral power groups and their envelopes for hazardous (BIW) sea states at both Saldanha Bay and Ngqura harbours.

.

7. CONCLUSIONS

7.1 The ocean wave continuum and sea surface geometry

The fractal analysis of sea surface time series data provides the Coastal Engineer with a novel technique for measuring and comparing different sea states in different environments.

Conventional sea surface displacements are described in terms of the Euclidean descriptors of maximum wave height (Hmax), significant wave height (Hm0) and peak frequency (fp) relating to size, and fractal dimensions describe the displacements on the basis of the shape of time series data. This shape is determined by means of a power law function, which relates similar features of scaled cascades within the series.

There is no direct link between the Euclidean geometry of the sea surface and the fractal geometry of a sea state time series as they are both described in different dimensions. However, the different dimensions and geometries are considered to be equally important in obtaining a more complete understanding of sea surface dynamics and they enable the Coastal Engineer to obtain a better understanding of the structure of the sea surface in terms of its degree of roughness.

The Singularity Spectra derived from Multifractal Detrended Fluctuation Analysis (MDFA) method and the Singularity Tree Structure derived from the Wavelet Transform Modulus Maxima (WTMM) method of analysis are both particularly useful means of describing this structure.

This research has established that singularities in sea surface displacements can be used to identify sea states incorporating a hazardous bound infragravity wave system. Further, the temporal distribution of singularity power derived from the wavelet analysis of times series data provides more information on possible long term forcing mechanisms on ship mooring systems, than a Fourier analysis of the same series.

The focus of the research has been on the application of the theory of fractal physics and mathematics to the field of coastal engineering in a methodical way, rather than on the carrying out of research into the theory of fractal analysis.

There is only a limited amount of published research on the topic of the fractal analysis of sea surface displacements in the field of coastal engineering. Having completed this research it is concluded that the fractal dimensions of sea states should be determined, together with the conventional wave characteristics of Hmax, Hm0 and fp values, in order to more completely define the nature of a sea state.

Sea surface displacements generally have short, rather than long period correlations, due to the fact that their amplitudes are bound by gravity. On the other hand they do have long period singularity power spectral clusters in the temporal domain as identified in Wavelet Transforms.

7.2 Summary of findings

The principal findings of this research are summarized as follows:

- Sea surface displacements, as recorded by single point time series data, are multifractal systems,

- Fractal analysis techniques are best applied to the comparison of two or more sets of data, in order to quantify their characteristic roughness, or persistence, or correlation. In this research we were able to describe a sea state by comparing it to both its effect on moored bulk carriers, as well as its fractal set of dimensions.

- Multifractal analysis methods, comprising the MDFA and WTMM processes, are far more useful than monofractal techniques for deriving meaningful fractal indices and characteristics of different sea states

- The Continuous Wavelet Transform method of analysis of a time series can be used for:
    - The fractal analysis of sea surface displacements, and
    - The analysis of long period singularity power spectral clusters, which are related power concentrations, in a wave train.

- Fractal Analysis techniques enable one to:
  - Dimension sea states that do not cause a hazard to moored shipping,
  - Dimension sea states that cause a hazard to moored shipping,
  - Identify a set of fractal indices that characterise a hazardous sea state by comparing the above two sets of results.
  - Compare the dimensions and persistence of hazardous sea states in two different locations.

- There are significant differences between multifractal sets of dimensions for sea states at Saldanha Bay harbour on the west coast and Ngqura harbour on the South east coast of South Africa

- Persistent long wave sea states occur during non-hazardous and hazardous bound infragravity wave conditions at both Saldanha Bay and Ngqura harbours.

- There is a significantly greater probability of persistent long wave sea states occurring at Saldanha Bay during hazardous infragravity wave sea states, than there is at Ngqura harbour.

7.3 Summary of contributions

This research verified and applied analysis techniques that can be used by coastal engineers to describe the shape of a sea state in terms of a set of fractal indices based on the scaling properties of a time series. This geometric description reflects the varying degrees of roughness in a wave train.

Hazardous Bound Infragravity Wave sea states can be characterised by a set of fractal dimensions derived from the analysis of hazardous and non-hazardous sea states in the same general location. This general location could be very extensive, encompassing either a large length of coastline, or a complete atmospheric weather climate region.

The fractal dimensions of bound infragravity wave sea states have clearly been shown to depend on the primary mechanism forcing the sea state, being either swell or wind sea. The implication of this finding is that care must be taken when using a set of fractal dimensions derived for a sea state at one location to identify a similar sea state at another location, without first identifying that differences that may exist between the atmospheric weather and wave climate conditions at the two locations.

The ability to quantify the shape of sea surface geometry, which can be observed but not measured in terms of Euclidean dimensions, is considered to be a significant contribution towards obtaining a broader, if not complete, characterisation and understanding of coastal wave conditions.

7.4 Future research

Having completed this research, it is considered that it would be worthwhile to carry out the further research into fractal analysis applications in the field of coastal engineering:

- The fractal analysis of a large sample of long wave sea states that have caused hazardous conditions at both Saldanha Bay and Ngqura harbours, in order to confirm or modify the findings of this introductory research.

- The comparison of long wave sea state descriptions derived by physical measurements, mathematical modelling and fractal analysis techniques to identify correlations that could further develop the application of fractal analysis methods in the field of coastal engineering.

- The comparison of fractal dimensions derived from single point sea surface displacement data and remotely sensed spatial imagery to identify correlations that could optimise the design processes for coastal protection works.

- The determination of sea surface roughness criteria for the optimisation of local boundary conditions for the mathematical modelling of inshore coastal areas.

REFERENCES

Ajiwibowo, H (2002), *Fractal Solutions to the Long Wave Equations*, Doctor of Philosophy thesis: Oregon State University.

Babinec, P, Kucera, M, Babincova, M (2005), *Global Characterization of Time Series Using Fractal Dimension of Corresponding Recurrence Plots: From Dynamical Systems to heart Physiology*, HarFA e-journal-Harmonic and Fractal Image Analysis (2005)

Billiones, RG, Tackx, ML, Daro MH (1999), *The Geometric Features, Shape Factors, and Fractal Dimensions of Suspended Particulate Matter in the Scheldt Estuary (Belgium)*, Estuarine, Coastal and Shelf Science (Volume 48, Issue 3 march 1999)

Berizzi, F, Dalle Mese, E, Pinelli, G (1997), *A two-dimensional fractal model of the sea surface and sea spectrum evaluation*, Radar 97 (Conf. Publ. no. 449)

Boesten, J (2014), *Mooring with HMPE rope,* FPSO Forum Monaco March 25 2014.

Botes, WAM, Russell, KS, Huizinga, P (1982), *Resonance in South African Harbours,* Proceedings of 18th Conference on Coastal Engineering, Cape Town, South Africa,1982.

Buckley, M, and Lowe, R (2013) *Evaluation of nearshore wave models in steep reef environments,* Coastal Dynamics 2013

Cambou, AD, and Menon, N (2011), *Three-dimensional structure of a sheet crumpled into a ball*, PNAS

Delignieres, D, Ramdani, S, Lemoine, L, Torre, K, Fortes, M and Ninot, G (2006), *Fractal Analysis of "short" time series: A re-assessment of classical methods*, ScienceDirect, Elsevier.

Delignieres, D, Torre, K, Bernard, P-L (2011), *Transition from Persistent to Anti-Persistent Correlations in Postural Sway Indicates Velocity-Based Control, PLoS* Computational Biology.

D'Hondt, H (1999), *Port and terminal construction design rules and practical experience*, Proceedings 12th International Harbour Congress, Antwerp

Diniz, A, Wijnants, ML, Torre, K, Barreiros, J, Crato, N, Bosman, AMT, Hasselman, F, Cox, RFA, Van Orden, GC, Delignieres, D (2011), *Contemporary theories of 1/f noise in motor control,* Human Movement Science 30.

Eke, A, Herman, P, Sanganahalli, BG, Hyder, F, Mukli, P and Nagy, Z (2012), *Pitfalls in fractal time series analysis: fMRI BOLD as an exemplary case,* Frontiers in Physiology.

Elgar, S, and Mayer-Kress, G (1989), *Observations of the Fractal Dimension of Deep-and Shallow-Water Ocean Surface Gravity Waves,* Elsevier, North-Holland Physics Publishing.

Elgar, S and Guza, RT (1985) *Shoaling gravity waves: comparisons between field observations, linear theory, and a non-linear model.* J. Fluid Mech. (1985).

Farrar, R, and Wordon, K (2013), *Structural Health Monitoring: A machine perspective*, John Wiley and Sons Ltd.

Freeman, WJ (2007), *Hilbert transform for brain waves*, Scholarpedia.

Freilich, MH, and Guza, RT (1984), *Nonlinear Effects on Shoaling Surface Gravity Waves,* Phil. Trans. R. Soc. Lond. A.

Funke, EF and Mansard, EPG (1980), *On the Synthesis of Realistic Sea States*, Coastal Engineering.

Goda, Y (2010), *Random Seas and Design of Maritime Structures*, 3rd Edition, World Scientific Publishing Co Pte Ltd.

Grant, R, and Holboke, M (2004), *Shallow Water Effects On Low-Frequency Wave Excitation of Moored Ships*, Offshore Technology Conference.

Harkins, GS, and Briggs, MJ (1994) *Resonant Forcing of Harbors by Infragravity Waves*, Proceedings of 24th Conference on Coastal Engineering, Kobe, Japan, 1982.

Herbers, THC, Orzech, M, Elgar, S and Guza, RT (2003), *Shoaling transformation of wave frequency-directional spectra*, Journal of Geophysical Research.

Herbers, THC, Elgar, S, Guza, RT, and O'Reilly, WC (1995), *Infragravity-Frequency (0.005-0.05 Hz) Motions on the Shelf. Part ll: Free Waves,* Journal of Physical Oceanography.

Holthuijsen, L (2008) *Waves in Oceanic and Coastal Waters*, Cambridge Press

Hughes, SA (1993), *Physical Models and Laboratory Techniques in Coastal Engineering,* World scientific Publishing Co Pte Ltd.

Hughes, BD (1995), *Random Walks and Random Environments, Volume 1: Random Walks*, Oxford University Press, 1995.

Ihlen, EAF (2012), *Introduction to multifractal detrended fluctuation analysis in Matlab,* Frontiers in Physiology.

Jensen, OJ, Viggosson, G, Thomsen, J, Bjordal, S, Lundgren, J (1990), *Criteria for ship movements in harbours*, Proceedings of 22nd Conference on Coastal Engineering, Delft, The Netherlands, 1990.

Jones, CL, Lonergan, GT, and Mainwaring DE (1996), *Wavelet packet computation of the Hurst exponent,* J. Phys. A: Math Gen 29

Journee, JMJ and Pinkster, J (2002), *Introduction in Ship Hydrodynamics*, Lecture MT 519, Delft University of Technology

Kantelhardt, JW, Zschiegner, SA, Koscielny-Bunde, E, Havlin, S, Bunde, A, Stanley, HE (2002), *Multifractal detrended fluctuation analysis on nonstationary time series*, Physica A.

Kantelhardt, JW (2008), *Fractal and Multifractal Time Series.* Institute of Physics: Martin-Luther-University, Halle-Wittenberg, Halle, Germany.

Katsev, S, and L'Heureux, I (2003), *Are Hurst exponents estimated from short or irregular time series meaningful?* Computers and geosciences 29 (2003)

Khan MM, and Fadzil, A (2007), *Singularity Spectrum of Hydrocarbon Fluids in Synthetic Seismograms,* International Conference on Intelligent and advanced systems, IEEE

Kofoed-Hansen, H, and & Rasmussen, JH (1998), *Stochastic Modelling of Nonlinear Waves in Shallow Water,* Coastal Engineering- 1998

Kristoufek, L (2010), *Rescaled Range Analysis and Detrended Fluctuation Analysis: Finite Sample Properties and Confidence Intervals*, AUCO Czech Economic Review 4 (2010)

Lakshina, V and Silaev, A (2012), *The Application of Fractals in Financial Time Series Modelling,* International Research Journal of Finance and Economics.

Liu, PC (1988) *What is the slope of equilibrium range in the frequency spectrum of wind waves?,* Proceedings of 21st Conference on Coastal Engineering, Torremolinos, Spain, 1988

Longuet-Higgins, MS and Stewart, RW (1962), *Radiation Stress and mass transport in gravity waves, with application to 'surf-beats',* Journal of Fluid Mechanics.

Longuet-Higgins, MS, and Stewart, RW (1960), *Changes in the form of short gravity waves on long waves and tidal currents*, Journal of Fluid Mechanics.

Longuet-Higgins, MS (1994), A Fractal Approach to Breaking Waves, Journal of Physical Oceanography.

Lopes, R and Betrouni, N (2009), *Fractal and multifractal analysis: A review.* Medical Image Analysis (2009).

Lovejoy, S, and Mandelbrot, BB (1985) *Fractal properties of rain, and a fractal model*, Tellus (1985)

MacHutchon K, Wessels J, Wu, C & Liu, P (2009), *The Use of Streamed Digital Video Data and Binocular Stereoscopic Image System (BISIS) Processing Methods to Analyse Ocean Wave Field Kinematics*, Proceedings of OMAE 2009 Conference.

Makowiec, D, Galaska, R, Rynkiewicz, A (2009), *Multifractal estimators of short-time automatic control of the heart rate*, Proceedings of the International Multiconference on Computer Science and Information Technology.

Mandelbrot, BB (1977), *The Fractal Geometry of Nature*, WH Freeman and Company, New York.

Mandelbrot, BB (1989), *Fractal Geometry*: *what is it, and what does it do?* Proc. R. Soc. Lond. A. 423 3-16

Mansard, EPD, and Pratte, BD (1982), *Moored Ship Response in Irregular Waves*: Proceedings of 18th Conference on Coastal Engineering, Cape Town, South Africa,1982.

Mansard, EPD and Sand, SE (1994), *A Comparative Evaluation of Wave Grouping Measures*, Proceedings of 24th Conference on Coastal Engineering, Kobe, Japan, 1994.

Marmelat, V, Torre, K and Delignieres, D (2012), *Relative roughness: an index for testing the suitability of the monofractal model*, Frontiers in Physiology.

McSharry, PE (2007), *Nonlinear Dynamics and Chaos,* Lecture Notes: Mathematical Institute, University of Oxford.

Moes, J and Terblanche, L (undated), *Motion criteria for the efficient, (un)loading of container vessels,* Technical Paper, CSIR Stellenbosch, South Africa.

Norheim, CA, and Herbers, THC (1998) *Nonlinear Evolution of Surface Wave Spectra on a Beach,* Journal of Physical Oceanography

Okihiro, M, Guza, RT & Seymour, RJ (1992), *Bound Infragravity Waves,* Journal of Geophysical Research.

Oltman-Shay, J and Hathaway, KK (1989), *Infragravity Energy and its Implications in Nearshore Sediment Transport and Sandbar Dynamics,* US Army Corps of Engineers, Technical Report CERC-89-8.

Otteson Hansen, NE, Sand, SE, Lundgren, H, Sorensen, T, Gravesen, H (1980), *Correct Reproduction of Group-induced Long Waves*, Proceedings of 17th Conference on Coastal Engineering, Sydney, Australia, 1980.

Ozger, M (2011), *Investigating the Multifractal Properties of Significant Wave Height Time Series Using a Wavelet-Based Approach*, Journal of Waterway, Port, Coastal and Ocean Engineering.

Paszto, V, Marek, L, Tucek, P, Janoska, Z (2011) *Perspectives of Fractal Geometry in GIS Analysis,* GIS Ostrava, 2011

PIANC Report No. 115-2012 (2012) *Criteria for the (Un)Loading of Container Vessels*, Maritime Navigation Commission

Rabinovich, AB (2008), *Seiches and Harbour Oscillations,* Text for publication in Handbook of Coastal and Ocean Engineering World Scientific.

Rangarajan, G, and Ding, M (2001), *An Integrated Approach to the Assessment of Long Range Correlation in Time Series Data*, Indian Institute of Science, Bangalore, India

Riley, M, Bonnette, S, Kuznetsov, N, Wallot, S, and Gao, J (2012), *A tutorial introduction to adaptive fractal analysis*. Frontiers in Physiology, vol. 3, Article 371.

Roelvink, D, Reniers, A, van Dongeren, A, van Thiel de Vries, J, McCall, R and Lescinski, J (2009), *Modelling storm impacts on beaches, dunes and barrier islands*, Coastal Engineering 56 (2009)

Roelvink, JA and Reniers, AJHM (2012), *A Guide to modelling Coastal Morphology*, World Scientific Publishing Co. Pte.

Roelvink, JA, Petit, HAH, and Kostense, JK (1992), *Verification of a One-dimensional Surfbeat Model against Laboratory Data,* Proceedings of 23rd Conference of Coastal Engineering, Venice, Italy, 1992.

Rossouw, M, Terblanche, L, and Moes, J (2013), *General Characteristics of Long Waves around the South African Coast,* Coasts and Ports 2013 Conference, Australia.

Sand, SE (1982), *Long Waves in Directional Seas,* Coastal Engineering, 6 – 1982.

Sarkar T, Salazar-Palma M, Wicks M (2002) *Wavelet Applications in Electromagnetics*, Artech House, Inc.

Schlurmann, T (2002), *Spectral analysis of nonlinear water waves based on the Hilbert-Huang Transformation*, Journal of Offshore Mechanics and Arctic Engineering.

Schoeman, S, Branch Manager, Rennies Ships Agency (Pty) Ltd (2013), Interview.

Shimizu, Y, Barth, M, Windischberger, C, Moser, E, and Thurner, S (2004), *Wavelet-based multifractal analysis of fMRI time series*, NeuroImage.

Soler, C (2006) *Swell and Wave-Groups in Saldanha Bay,* Master Thesis, Delft University of Technology

Stanley, HE, Amaral, LAN, Goldberger, AL, Havlin, S, Ivanov, PCh and Peng, C-K (1999), *Statistical physics and physiology: Monofractal and multifractal approaches,* Physica A.

Stiassnie M (1988), *The fractal dimension of the ocean surface,* in Nonlinear Topics in Ocean Physics, Proceedings of the International School of Physics Enrico Fermi, AR Osborne, Ed, pp 633-647.

Stiassnie M (1991), *The multifractal structure of the ocean surface*, Proceedings of the Nonlinear Water Wave Workshop, Bristol, England. DH Peregrine, Ed, pp 140-147.

Stowe, P (Capt., Retired), (2014), Interview.

Struzik, ZR, and Siebes, A (1999), *Measuring Time Series' through Large Similarity Features Revealed with Wavelet Transformation*, DEXA '99 Proceedings of the 10th International Workshop on Database & Expert Systems Applications.

Struzik, ZR (1999), *Direct Multifractal Spectrum Calculation from the Wavelet Transform*, Stichting Mathematisch Centrum, Amsterdam. Report INS-R9914.

Stuart, DCA (2013), *Characterizing Long Wave Agitation in the Port of Ngqura using a Boussinesq Wave Model*, Master of Science Thesis, Stellenbosch University.

Symonds, G, Huntley, DA and Bowen, AJ (1982), *Two-Dimensional Surf Beat: Long Wave Generation by a Time-Varying Breakpoint,* Journal of Geophysical Research.

Terrence C, and Compo, G (1998), *A Practical Guide to Wavelet Analysis,* Programme in Atmospheric and Ocean Sciences, University of Colorado, Boulder, Colorado

Theiler, J (1990), *Estimating fractal dimension*, Optical Society of America.

Theiller, J (1990), *Estimating the Fractal Dimension of Chaotic Time Series*. The Lincoln Laboratory Journal. vol. 3, no. 1.

Thomson, J, Elgar, S, Herbers, TCH, Raubenheimer, B and Guza, RT (2007), *Refraction and reflection of infragravity waves near submarine canyons,* Journal of Geophysical Research.

Transnet website, (2009), *Saldanha Bay: Port Information and Operating Guidelines*, Transnet National Ports Authority.

Van Giffen, IK, Battjes, JA Van Dongeren, AR and Moes J (2003) *Simulation of Long Waves in Saldanha Bay*, Long Waves Symposium 2003

van der Molen, W, and Moes, J (2009), *General Characteristics of South African Ports and the Safe Mooring of Ships*, Southern African Transport Conference.

van Oorschot, JH (1976) *Subharmonic Components of Hawser and Fender Forces*. Proceedings of 15th Conference of Coastal Engineering, Honolulu, Hawai, 1976.

Voss, J (2013), *Rescaled Range Analysis: A method for detecting Persistence, Randomness or Mean Reversion in Financial Markets*, Enterprising Investor, CFA Institute.

Wilson, BW (1953), *The Mechanism of Seiches in Table Bay Harbour, Cape Town,* Proceedings of Fourth Conference on Coastal Engineering, Chicago, Illinois..

Xiao-Guang, MA, and Fei, HU (2004) *Refined Structure of Energy Spectrum and Energy Cascade in Atmospheric Turbulence*, Chinese Journal of Geophysics

Xiong, G, Zhang, S, Yang, X (2012) *The fractal energy measurement and the singularity energy spectrum analysis*, Physica A 391 (2012)

Yuen, AF, Burke MG and Leung TC (1986), *Ship Motion Study for the 2010 and 2020 Plan in the San Pedro Bay, California*, Coastal Engineering.

Zaourar, N, Hamoudi, M, Mandea, M, Balasis, G and Holschneider, M (2013) *Wavelet-based multiscale analysis of geomagnetic disturbance*, Earth Planets Space 65